AFFDL-TR-78-182
PART II

FUEL TANK SURVIVABILITY FOR HYDRODYNAMIC
RAM INDUCED BY HIGH VELOCITY FRAGMENTS
PART II: NUMERICAL ANALYSES

CALIFORNIA RESEARCH & TECHNOLOGY, INC.
FOR
UNIVERSITY OF DAYTON RESEARCH INSTITUTE
300 COLLEGE PARK
DAYTON, OHIO 45469

FEBRUARY 1979

APPROVED FOR PUBLIC RELEASE - DISTRIBUTION UNLIMITED

AIR FORCE FLIGHT DYNAMICS LABORATORY
AIR FORCE WRIGHT AERONAUTICAL LABORATORIES
AIR FORCE SYSTEMS COMMAND
WRIGHT-PATTERSON AIR FORCE BASE, OHIO 45433

REPORT DOCUMENTATION PAGE	READ INSTRUCTIONS BEFORE COMPLETING FORM

1. REPORT NUMBER	2. GOVT ACCESSION NO.	3. RECIPIENT'S CATALOG NUMBER
AFFDL-TR-78-182		

4. TITLE (and Subtitle)	5. TYPE OF REPORT & PERIOD COVERED
FUEL TANK SURVIVABILITY FOR HYDRODYNAMIC RAM INDUCED BY HIGH VELOCITY FRAGMENTS. PART II. NUMERICAL ANALYSIS.	Final Report. October 1977–October 1978
	6. PERFORMING ORG. REPORT NUMBER
	CRT-3200-02

7. AUTHOR(s)	8. CONTRACT OR GRANT NUMBER(s)
H. Schuster S. Macales	F33615-77-C-2082

9. PERFORMING ORGANIZATION NAME AND ADDRESS	10. PROGRAM ELEMENT, PROJECT, TASK AREA & WORK UNIT NUMBERS
California Research & Technology, Inc. 6269 Variel Avenue, Suite 200 Woodland Hills, California 91367	Project No. 2402 Task No. 02 Work Unit No. 24020218

11. CONTROLLING OFFICE NAME AND ADDRESS	12. REPORT DATE
Air Force Flight Dynamics Laboratory Wright-Patterson Air Force Base, Ohio 45433	February 1979
	13. NUMBER OF PAGES
	92

14. MONITORING AGENCY NAME & ADDRESS(if different from Controlling Office)	15. SECURITY CLASS. (of this report)
	Unclassified
	15a. DECLASSIFICATION/DOWNGRADING SCHEDULE

16. DISTRIBUTION STATEMENT (of this Report)

Approved for Public Release - Distribution Unlimited

17. DISTRIBUTION STATEMENT (of the abstract entered in Block 20, if different from Report)

18. SUPPLEMENTARY NOTES

Work performed under UDRI Subcontract No. 82770.

19. KEY WORDS (Continue on reverse side if necessary and identify by block number)

Hydrodynamic Ram	Numerical Simulation
Fuel Tank	Analytic Forcing Functions
Entrance Panels	CRALE 2D Finite Difference Code
	NONSAP 2D Finite Element Code

20. ABSTRACT (Continue on reverse side if necessary and identify by block number)

Numerical finite difference (CRALE) and finite element (NONSAP) calculations of the behavior of fuel tank front panels, penetrated by steel fragments impacting at velocities of 1.0-2.0 km/sec were used to explain the phenomena observed in an accompanying experimental program (Part I of this report). Analytic expressions for the variation of peak pressure and impulse along the panel as functions of fragment size, velocity, and panel areal density were derived from the finite difference runs and used as boundary conditions in the finite element calculations of panel failure and displacements.

DD FORM 1473 EDITION OF 1 NOV 65 IS OBSOLETE
1 JAN 73

UNCLASSIFIED

The increase in survivability achieved by inserting a 1.0 cm layer of foam behind the front panel was explained by the resultant changes in the timing of the loading along the panel.

PREFACE

The program described in this report was carried out by California Research & Technology for the Air Force Flight Dynamics Laboratory, under a subcontract with the University of Dayton Research Institute. Most of the work was done under Contract F33615-77-C-2082. Mr. William. E. Hackenberger was the monitor for that contract. The UDRI subcontract No. 82770 was monitored by Dr. Stephen Bless.

Sheldon Schuster of CRT served as Principal Investigator. The calculations were executed under the supervision of Jack Macales. Dr. Marvin Ito and Ken Kreyenhagen assisted in the finite difference analysis and in the review of the numerical results.

Accession For

NTIS GRA&I

DDC TAB

Unannounced

Justification

By

Distribution/

Availability Codes

Dist | Avail and/or special

A

iii

TABLE OF CONTENTS

PAGE

v

TABLE OF CONTENTS (CONT.)

LIST OF ILLUSTRATIONS

LIST OF ILLUSTRATIONS FOR APPENDIX A

INTRODUCTION AND SUMMARY

1.1 Prior Studies

The ability of numerical codes to model the impact and penetration of bullets and spherical fragments into aircraft fuel tanks has been demonstrated in previous studies at CRT[1,2]. In the more recent of these programs, the behavior of 1/16-in. (.158-cm) 2024-T3 aluminum entrance panels impacted by spheres at 1.55 km/sec was examined. The calculated results generally agree with stress and velocity measurements obtained from companion experiments. Peak displacments of the entrance panels were substantially underpredicted by the analyses. Some of this discrepancy may be due to the truncation of that portion of the numerical analysis which determines the late-time loading on the internal surface of the panel. For *bare* panels (i.e. where the fluid is in direct contact with the entrance panel), the *peak stresses* which initiate catastrophic failure are experienced close to the impact hole at relatively early times; these stresses decline before the late-time, maximum displacements of the panel occur.

1.2 Objectives of Current Program

Continuing the study of fragment impacts on entrance panels, the objectives of the current program at CRT have been:

o to formulate analytical loading functions to describe the time- and space-resolved force applied by the fluid to the internal surface of the entrance panel, as a function of impacting mass, velocity, and panel thickness, (Section 3),

o to develop a methodology, based on numerical solutions and calibration experiments, for predicting the minimum velocity needed to produce catastrophic failure of an entrance panel as a function of impacting mass, panel thickness, and panel strength properties, (Section 4).

1

Time histories of entrance panel displacements were also calculated for selected cases for comparison with UDRI test observations (Section 5). Finally, the changes in front panel loading produced by the inclusion of a foam layer behind the panel were examined (Section 6) and compared with the corresponding bare panel results.

1.3 Nature of Panel Penetration and Response

1.3.1 Primary Penetration

Impact of a steel projectile on an aluminum entrance panel at velocities of 1.4-2.0 km/sec produces initial pressures in the 100 - 500 kb regime. Such pressure propagates as a shock wave system in all directions from the impact point, both laterally into the aluminum, and across the interface into the fluid behind the panel. Within the aluminum, interaction of the extreme pressures with the outer and inner surfaces of the panel results in large plastic distortions and failure. The exact character of the hole which forms will depend on the impact velocity, the projectile shape, and the thickness of the panel relative to the projectile dimensions. Shear and/or tensile failure will occur, and there is generally some outward (radial) plastic distortion and consequent thickening of the aluminum around the hole. The hole size is usually larger than the projectile, being weakly dependent on impact velocity and plate thickness.

1.3.2 Panel Response to Early Shock Loading by Fluid

The shock pressure system propagates into the fluid ahead of the projectile and also radially from the projectile. This radial wavefront results in an enlarging high pressure region immediately behind the entrance panel. Application of pressure to the inner surface of the panel causes an outward acceleration with consequent rapid drop in the pressure. This phase of the loading is therefore intense and of short duration. It is also relatively concentrated, since the shock pressure decays with

2

distance from the impact site. Early shock loading is the critical phase for panels which are in direct contact with the fluid. The outward displacement of the panel near the impact site during the first 100μsec leads to large tensile hoop stresses near the hole; if these are sufficiently intense, radial cracks will start to propagate out from the hole. Experimental observations confirm that such cracks start in the initial 100 μsec.

1.3.3 Panel Response to Late-Time Pressure Loading

As the projectile penetrates, it transfers energy into the fluid due to drag. Part of this energy goes into thermal energy, but much of it goes into kinetic energy of the fluid. The fluid behaves essentially incompressibly at the pressures involved, so fluid is set into motion not only close to the projectile, but also at substantial ranges from the projectile, including along the front panel.

If the panel is to survive, it must eventually decelerate or deflect the fluid moving towards it. In so doing, the panel responds as a diaphragm which is loaded by internal pressure. This long-duration load can cause appreciable deflection which is less localized than the response to early-time loading. In the case of a panel in which radial cracks have already been initiated during the early shock loading, the long-duration internal pressure due to projectile drag is the mechanism which drives the cracks to catastrophic failure. This is also confirmed by experimental observation, which show the radial cracks propagating at 200 - 300 m/sec. Such cracking thus persists for several hundred μsec after the initial shock loading has dissipated.

SECTION II.

NUMERICAL APPROACH

The two-phase finite difference (FD)/finite element (FE)
technique used in the previous study[2] was expanded and improved
in the current effort. For example, the .635cm and .158 cm
thick 7075(T6) Aluminum entrance panels investigated in this
program were explicitly modeled in the FD calculations;
avoiding the necessity for the point mass inertial approximation
used to represent the .158 cm panels considered in the earlier
work. The basic codes used for the FD/FE analyses were the
CRALE-2 finite difference method and the CRT NONSAP finite
element method. CRALE-2 uses as arbitrary coordinate motion
technique adapted from the AFTON code, i.e., the grid points are
neither Lagrangian or Eulerian but move to maintain an appropriate
grid spacing.

The boundary between the aluminum and fluid in the FD analyses
was treated as a sliding interface. The materials were only con-
strained to have the same normal velocities; their respective
tangential velocities were independently determined from their
internal forces. No shear stresses could be transmitted across
the interface. The appropriate algorithms for this interface
treatment are standard in CRALE-2.

The steel cubes used in the tests were modeled as equivalent-
mass spheres in the 2-D axisymmetric calculations. This approx-
mation appeared justified by early test data on .635 cm panels
which show nearly circular holes formed in the entrance panels
by impacts of cubes. However, several shots (e.g. FD31 and FD33)
with .158 cm Aluminum front panels, which were fired late in the
test program, clearly show failure cracks originating from the
corners of the cube. Thus, the use of spherical penetrators
probably underestimates the damage in the thinner panels.
Another potential error resulting from the use of spheres to
represent the penetrators occurs during the drag phase of the
calculation. The lower drag coefficient of a sphere compared to
that of either a cube or the fragments of cube and front panel

4

which actually enter the tank increases the time interval over which the total impact energy and momentum are delivered to the water. However, initiation of fracture of the front panel occurs during the early shock phase. Therefore, the difference in drag forces due to the penetrator shape probably cannot effect the minimum velocity required to induce failure significantly. Similarly, peak displacements occur long after most, if not all, of the impact energy has been delivered to the tank. Again, the details of the drag phase are of secondary concern. No attempt, therefore, was made by modifying the shape or size of the impacting sphere to mockup different drag coefficients.

As illustrated in velocity field and grid plots of Figure 1, the Lagrangian nature of the outer surface of the Aluminum panel and the Aluminum-fluid interface are maintained in the calculation, while interior grid points are adjusted or rezoned so that grid distortions are minimized. In both the experiments and analyses, the fluid behind the panel was water, which has shock and compression properties nominally similar to fuels.

The finite difference (CRALE) calculations of the pressure-time behavior of the water adjacent to the entrance panel under a variety of impact conditions were used to derive a set of loading functions. These functions define the time and space-resolved force applied to the panel, $f(R,t)$, as its dependence on impact velocity, sphere diameter, and Aluminum panel thickness. These relationships were then applied as boundary conditions in NONSAP calculations of the response of a 37.5 cm radius Aluminum panel. The outer boundary of the panel was assumed to be rigidly attached to a frame and was not allowed to move. This is an adequate representation of the important characteristics of the panel, inasmuch as both test observations and analyses show that the motions leading to failure occur within 100μsec of impact.

5
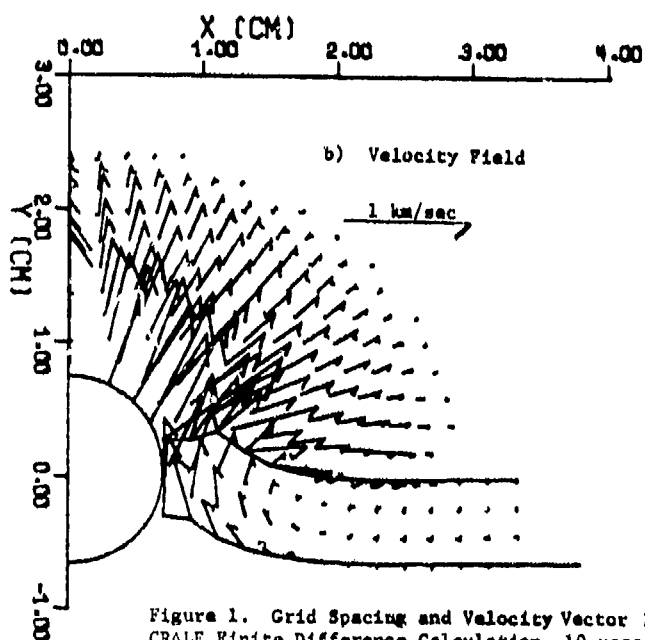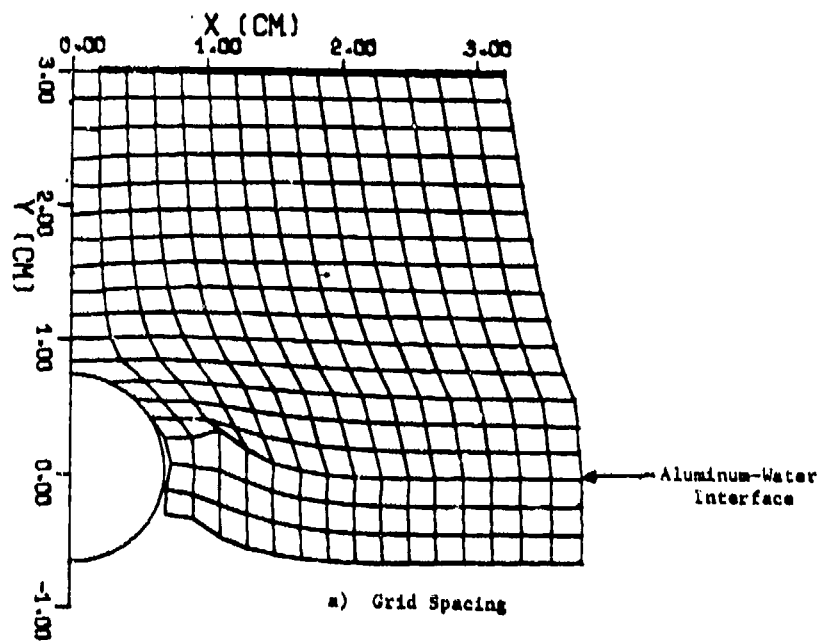
Figure 1. Grid Spacing and Velocity Vector Field in the CRALE Finite Difference Calculation, 10 μsec After Impact of a 11.66 gm Steel Sphere, V=1.63 km/sec onto a Fuel Tank with ¼" Aluminum Front Panel.

6

Only signals running radially outward along the disc can reach
the boundary in this time, and these signals are quickly damped.
For the NONSAP analysis, a 2-cm dia. entrance hole in the panel
was assumed, consistent with test results.

7

CRALE FINITE DIFFERENCE ANALYSIS OF EARLY-TIME PANEL LOADING

3.1 Functional Fits to the Calculations

Initially, the peak pressures and total impulses in the fluid adjacent to the inner surface of the Aluminum panels were obtained from results of four CRALE calculations, two from the current study and two from the earlier study:

Table I. Finite difference cases used to derive the initial set of loading functions.

Case*	Sphere DIA (cm)	Impact Velocity (km/sec)	Panel Thickness (in.)	Panel** Material
7L1.63	1.41	1.63	1/4-in.	7075-T6
7L1.80	1.41	1.80	1/4-in.	7075-T6
2S1.55	1.11	1.55	1/16-in.	2024-T3
2L1.55	1.43	1.55	1/16-in.	2024-T3

Fits of the calculated peak pressure and impulse were then used to derive the following generalized functions defining loading on the inner surface of the panel:

$$P_m \text{ (kbars)} = 3.0D^2\omega^{.25}VR^{-(2+4\omega)} \qquad (1)$$

$$I_{total} \text{ (bar-sec)} = .0165D^{.8}\omega^{.45}V^2e^{-.365R} \qquad (2)$$

where
D = sphere dia (cm)

V = impact velocity (km/sec)

R = radius from impact point (cm)

ω = panel thickness (cm)

---

* Throughout this report, the notation used by UDRI will be used to identify impact and panel conditions. 7 or 2 designates the panel Aluminum alloy (7075-T6 or 2024-T3). Underlining this digit (e.g., 7) designates a thick (1/4-in.) panel; otherwise it is this (1/16-in.). L or S designates the large (11.66 gm) or small (5.83 gm) projectile. A calculation of an extra large 22.4 gm, 1.75 cm diameter penetrator is designated X).

** Early-time internal loading of the panel is affected by its areal density (i.e., material density and thickness), but is insensitive to mechanical properties.

These fits (equation 1 and 2) are compared with the data
from the four calculations in Figures 2 and 3. The exponents
in the fits were derived by comparing pairs of calculations:
the effect of fragment size (D) from 2S1.55 vs 2L1.55, the
effect of velocity (v) from 7L1.63 vs 7L1.80, and the effect
of panel thickness (ω) from the difference between the two
pairs. Equations 1 and 2 were used to define the loading forces
in the NONSAP analysis of the front panel failure and displace-
ment discussed in Section 4 and 5.

After these initial calculations were completed, the results
of the test program conducted by UDRI were made available for com-
parison. In general, the derived functions appeared to under-
estimate both peak pressure and impulse. A series of calculations,
run only to 75μsec to permit the use of finer zoning, was under-
taken in order to better define the functional dependence of the
pressure and impulse with velocity, fragment size and plate
dimensions.

The cases studied included:

Table II   Finite Difference Cases used to Derive the Final
           Loading Functions (Fig. 4)

Case	Sphere Diam (cm)	Impact Velocity (km/sec)	Panel Thickness (cm)
RL1.63	1.41	1.63	rigid
7L1.80	1.41	1.80	.635
7L1.63	1.41	1.63	.635
7X1.63	1.75	1.63	.635
7S1.63	1.11	1.63	.635
7L1.63	1.41	1.63	.158
7L1.35	1.41	1.35	.635
7S1.35	1.11	1.35	.158

These cases were chosen so that each of the parameters;
sphere radius (R_p), initial velocity (V), and plate thickness
(ω), assumed at least three different values. The resultant
functional form of peak pressure (equation 3) and impulse
(equation 4) are presented in Figure 4. These final functions
differ from equations 1 and 2 in several major respects. First,
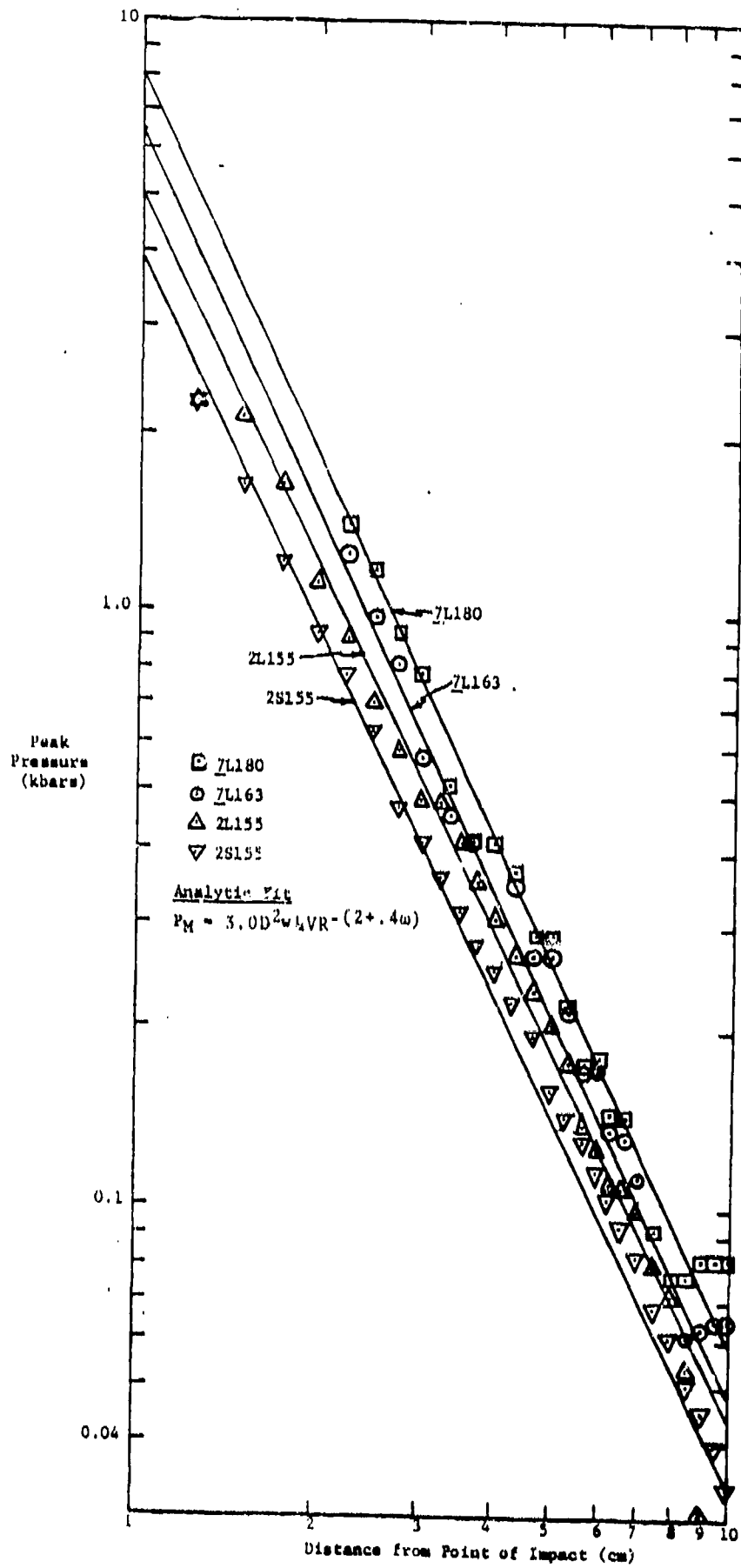
Figure 2. Calculated and Analytic Peak Pressure along Panel as Function of Distance from Point of Impact.

10

7L180
7L163
2L155
2S155

Analytic Fit

$I = .0165D^{.8} \omega^{.45} V^2 e^{-.365R}$

.01

I
(bar-sec)

.001

2   4   6   8   10   12

Distance from Point of Impact (cm)
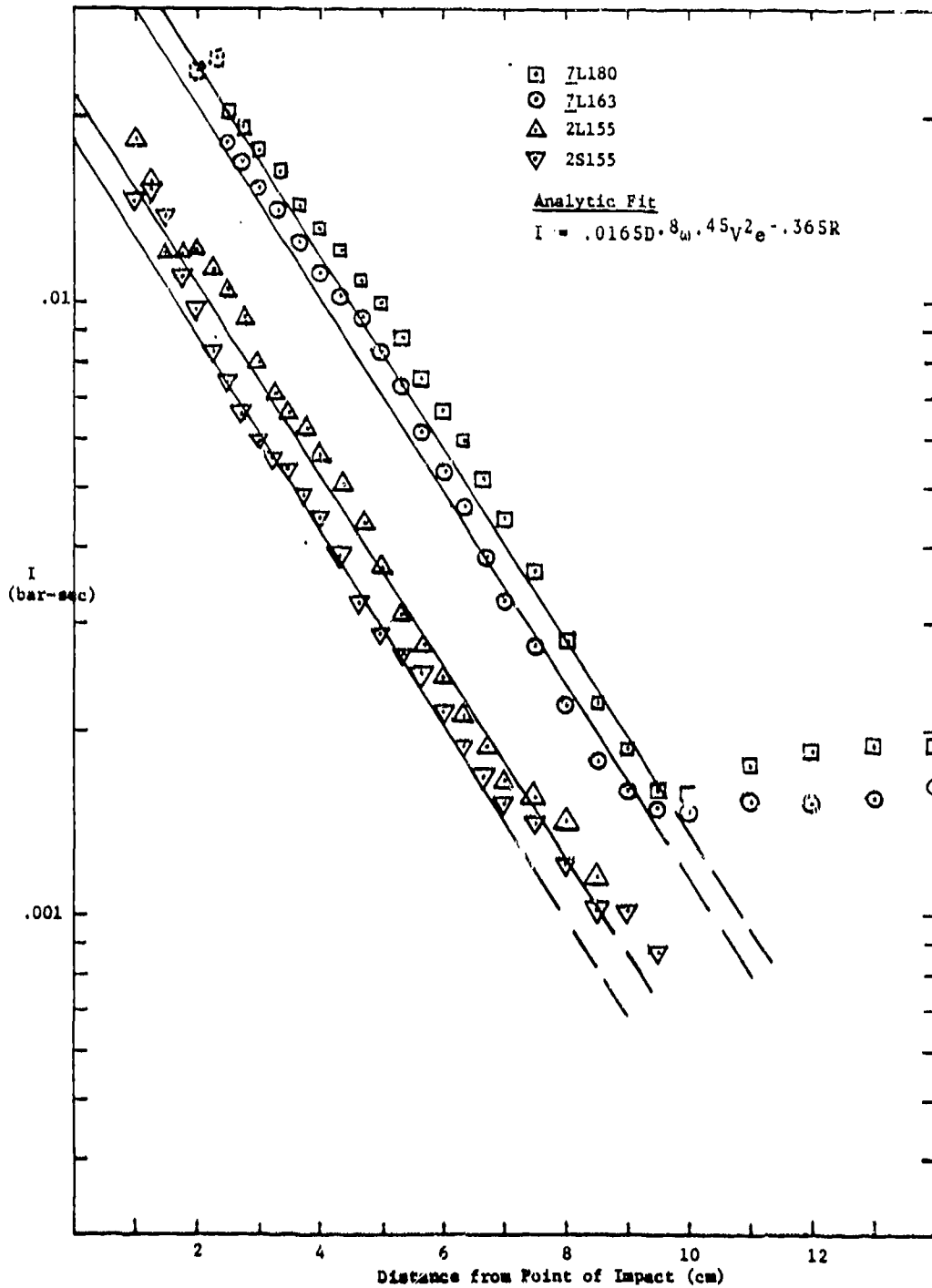
Figure 3. Total Impulse, Calculated and Analytic Fits as Function of Distance from Point of Impact.

11
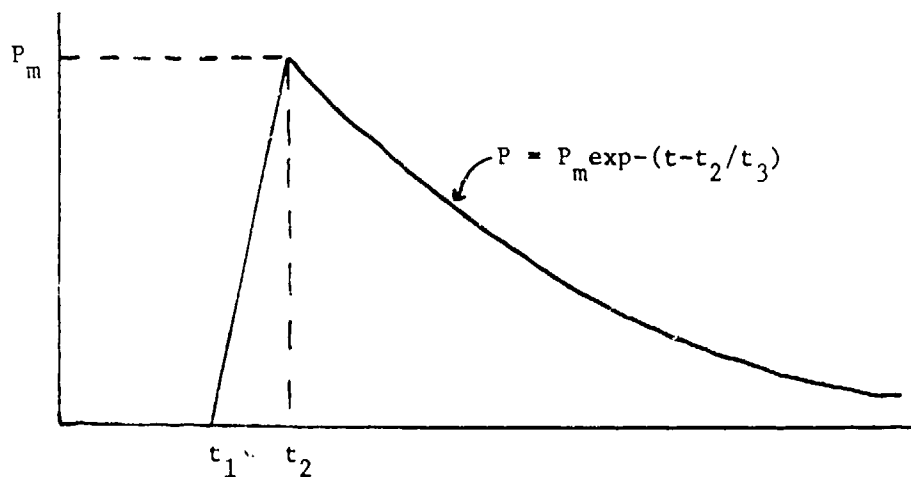
Let:

R_p = Average radius of impacting fragment (cm)

V_p = Initial fragment velocity (km/sec)

$\rho\omega$ = Front plate areal density (gm/cm^2)

t_1, t_2, t_3 = Time (μsec)

R = Distance along front panel from point of impact (cm)

I = Total impulse (Mb-μsec $\equiv$ bar-sec)

P_m = Peak pressure (kbars)

Then:

$$P_m(R) = 3.68\delta V(R'/R_p)^{-\alpha} \tag{3}$$

$$\alpha = 1.15 + .6e^{-.72\,\rho\omega} \tag{4}$$

$$I(R) = .03\delta V e^{-(\beta R'/R_p)} \tag{5}$$

$$\beta = .185 + .35e^{-.63\,\rho\omega} \tag{6}$$

$$R' = \min \begin{cases} R \\ 10 \end{cases} \tag{7}$$

$$\delta = \sqrt{R'/R} \tag{8}$$

$$t_2 = \omega/V_p + (R-R_p).16 \tag{9}$$

$$t_1 = t_2 - (2\omega/.63+1) \tag{10}$$

$$t_3 = \min \begin{cases} I/P_m - .5(t_2-t_1) \\ 10. \end{cases} \tag{11}$$

Figure 4. Generalized Front Panel Loading Functions

12

the dependence on fragment size is accounted for by normalizing the distance from the impact point by the average radius of the fragment (R/Rp). This relation was suggested in the original pressure function (equation 1) in which the pressure depended on the product of D^2 and $R^{-(2 + .4\omega)}$. Figures 5 and 6 illustrate how well a single line fits the three cases in which the fragment radius was varied ($\underline{7}$S1.63, $\underline{7}$L1.63 and $\underline{7}$X1.63).

The second parameter, V_p, is best represented by a linear dependence for both pressure and impulse (Figures 7 and 8). Thus it would appear that the initial shock pressure ($\rho_0 C_s V$) is the source of the pulse along the panel rather than the drag pressure effect ($\tfrac{1}{2}\rho_0 V^2$). Having both pressure and impulse depend on the same power of velocity is also an improvement over equation 2, since impulse is an integral of pressure over time.

Finally, the very weak dependence on front panel thickness, ω, in equations 1 and 2($\omega^{.25}$ for pressure and $\omega^{-.45}$ for impulse) has been replaced by the appearance of the areal density, $\rho\omega$, in the exponents of (equations 4 and 6). Thus, the pressure for a rigid (i.e. $\rho\omega = \infty$) front panel, decays as $R^{-1.15}$, slightly faster than R^{-1} dependence one expects for the decay from a point source. As the panel thickness decreases, the decay is more rapid, approaching $R^{-1.75}$ at zero thickness. This is due to the increased relief from the surface. The rather complex exponential decay of the impulse was unexpected and no physical explanation has been found for this dependency, however, the comparisons of the analytic fits to pressure and impulse, Figures 9 and 10, are quite good. The use of areal density, $\rho\omega$, cannot be justified by the calculations, all of which had Aluminum front panels. However, the inertia of the panel, rather than its compressibility or shear strength appears to be the most important feature at early times. Furthermore, the comparison of the fits with data from a test with a graphite-epoxy panel in Section 3.3 support the generalization to $\rho\omega$.

13
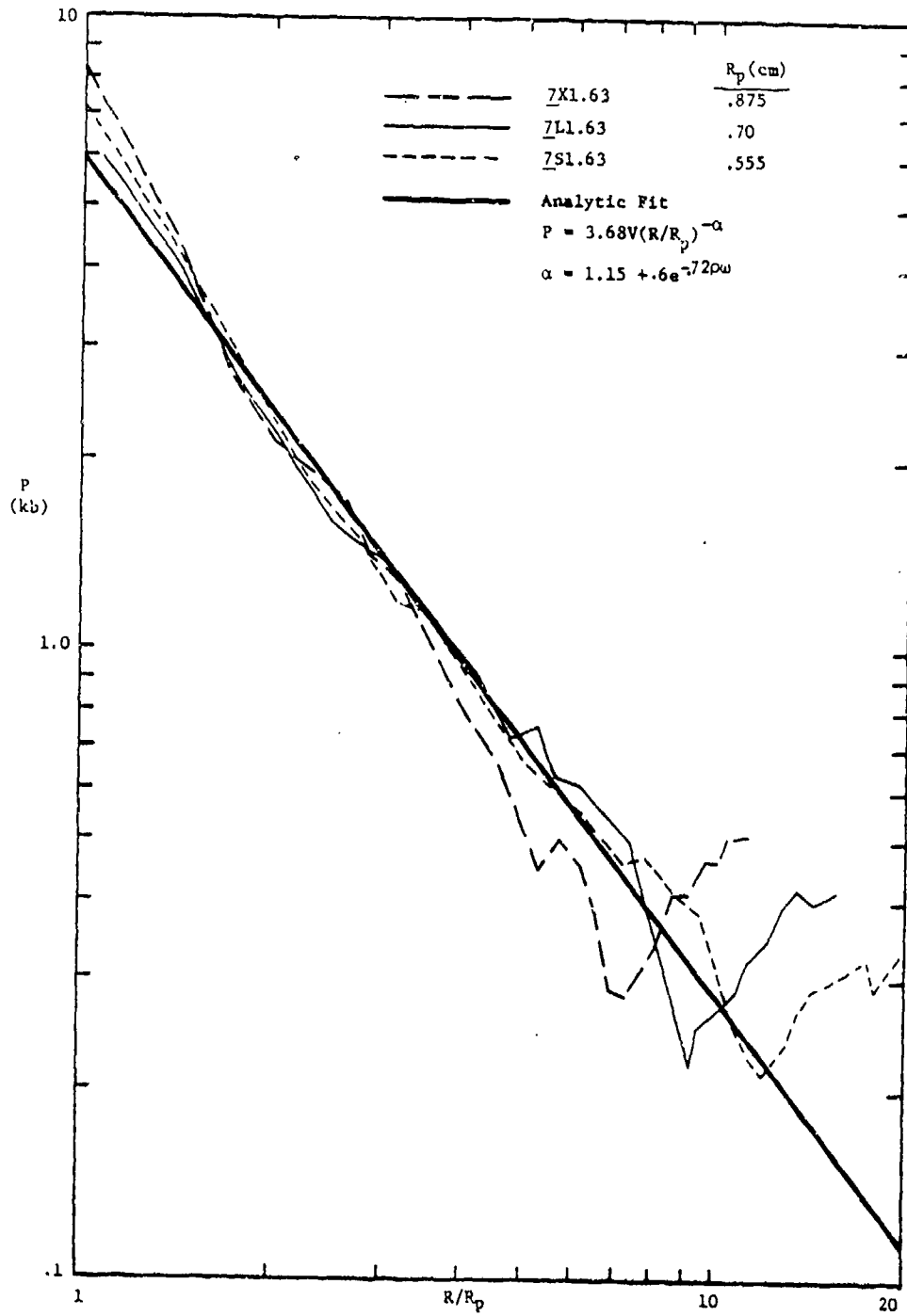
Figure 5. Comparison of Analytic Fits with calculated peak pressures along the entrance panel to illustrate the effect of scaling by penetrator radius, R_p.

14
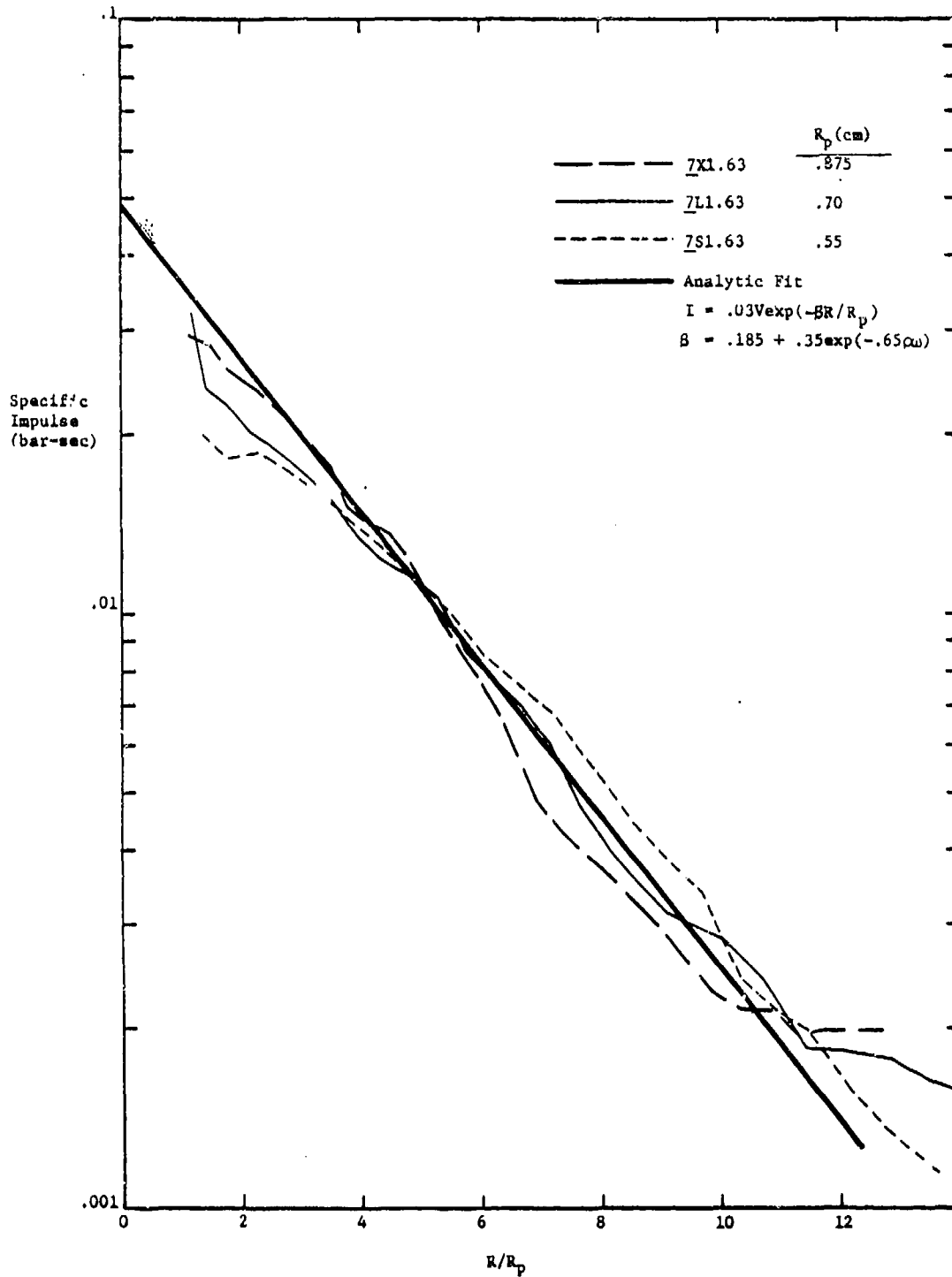
Figure 6. Comparison of the Analytic Fits with calculated Specific Impulse to 75 μsec to illustrate the effect of scaling by the penetrator Radius, R_p.

15
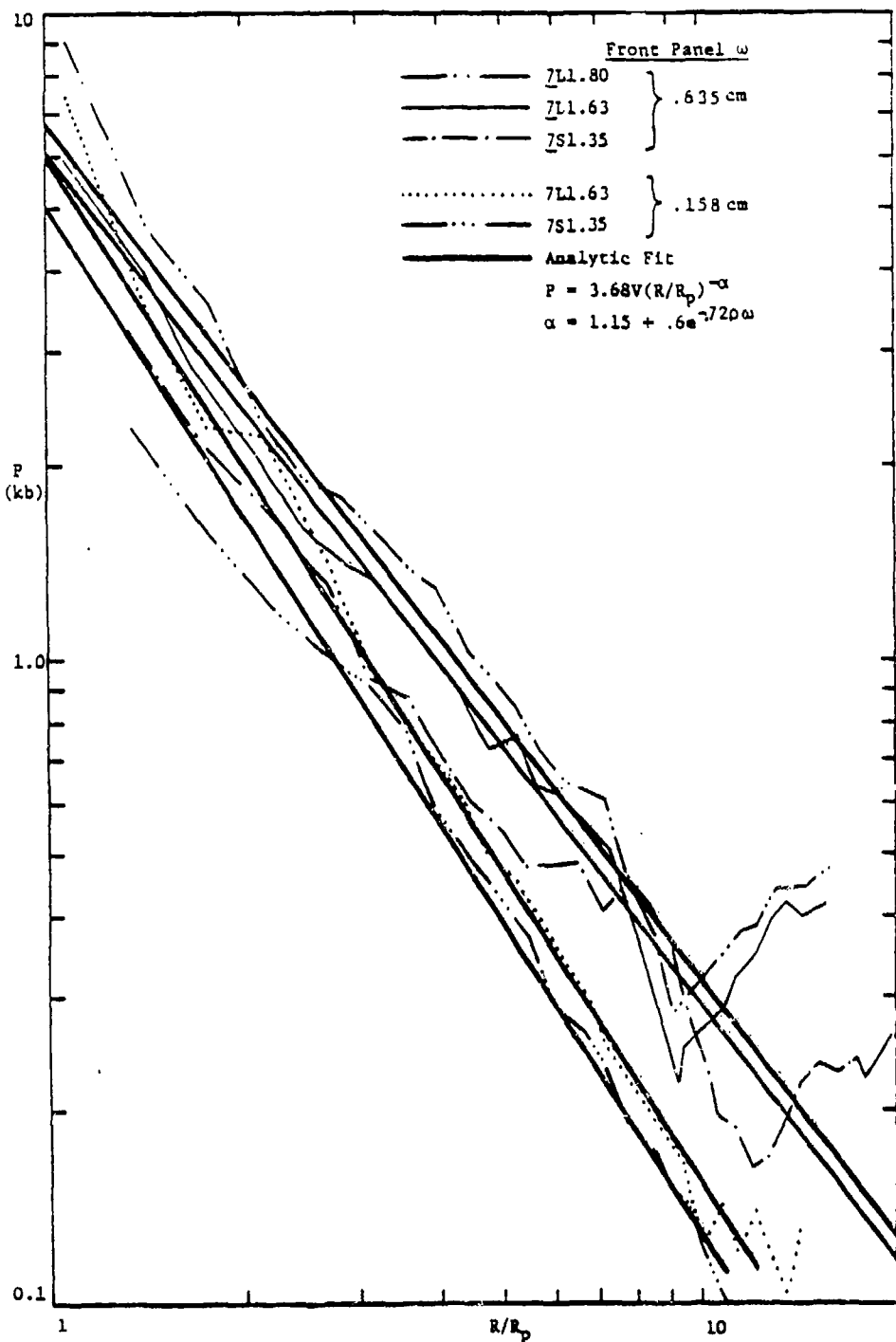
Figure 7. Comparison of Analytic Fits with calculated peak
pressure along the front panel to illustrate the
effect of initial penetrator velocity, V.

16
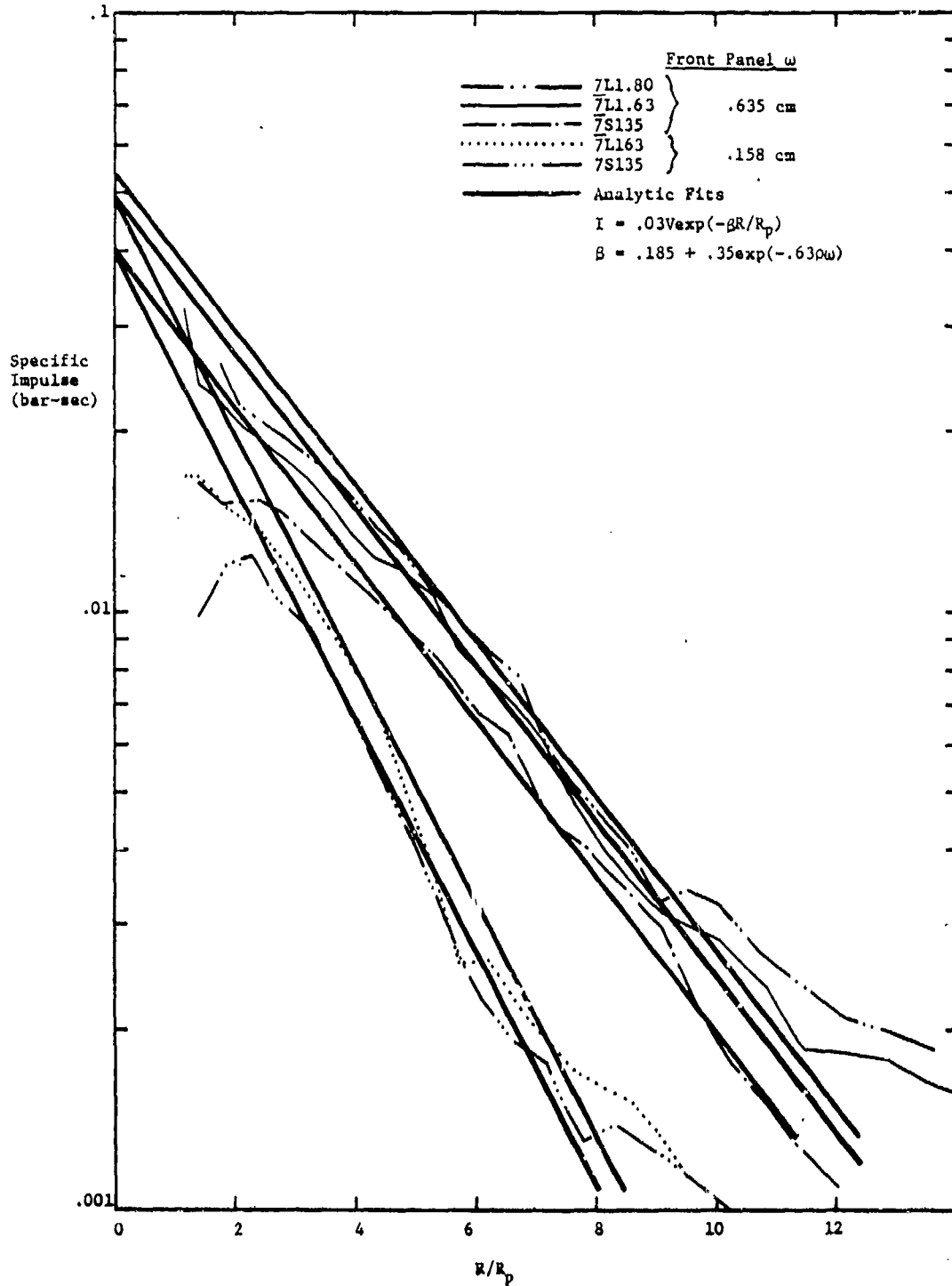
Figure 8. Comparison of the Analytic Fits with calculated specific impulse to 75 μsec along front panel to illustrate the effect of the initial penetrator velocity, V.

17
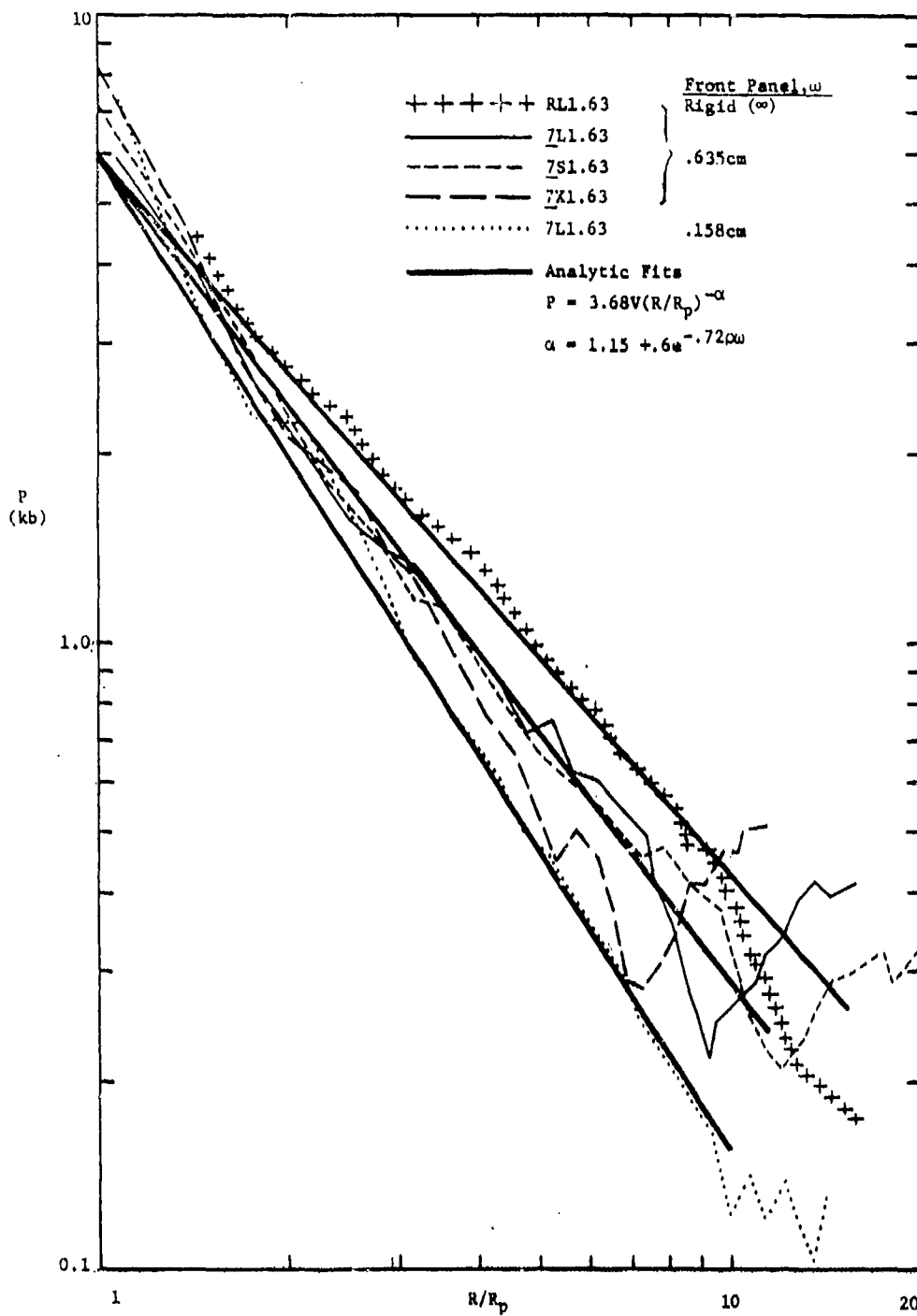
Figure 9. Comparison of Analytic Fits with calculated peak pressures along the entrance panel to illustrate the effect of the front panel areal density, $\rho\omega$.

18
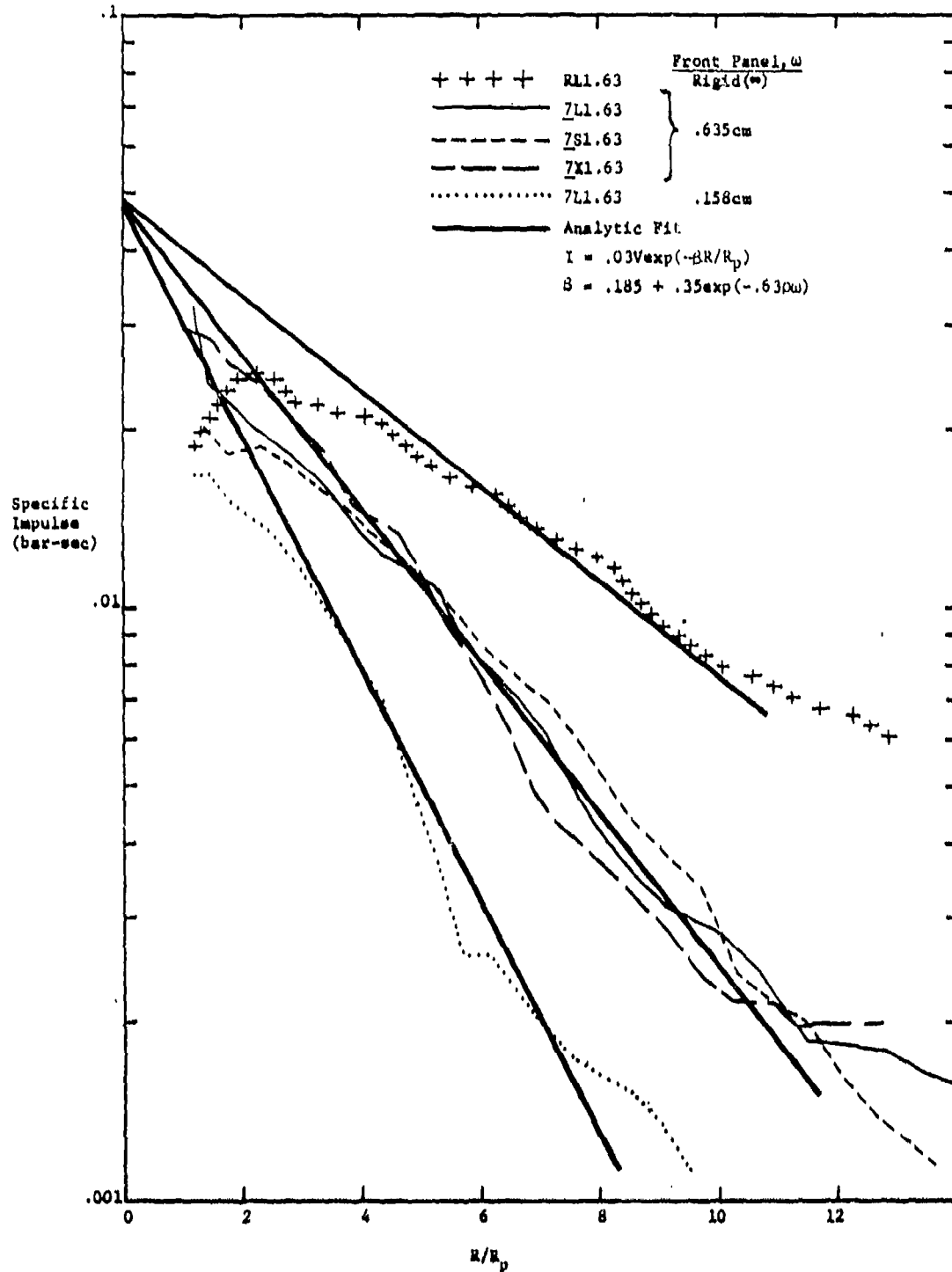
Figure 10. Comparison of the Analytic Fits with calculated specific impulse to 75 μsec along front panel to illustrate the effect of entrance panel areal density, $\rho\omega$.

19

In addition to peak pressure and specific impulse, a complete analytic description of the loading function at any distance from the point of impact requires a representation of the pressure as a function of time. After examining many waveforms from the various FD calculations, the generalized pulse shown in Figure 4 was selected. It consists of a linear rise to P_m followed by an exponentially decaying tail. The time at which the peak pressure occurs, t_2, is just the sum of the time needed for the fragment to pass through the front panel (ω/V_p) and the travel time of a shock wave (V = 1.6 km/sec) out to the range of interest. The time of first arrival, t_1, is set several μsec before t_2, for convenience, in subsequent calculations. A true shock wave would have a discontinuous jump to P_{max} (i.e., $t_2-t_1=0$). The time constant of the exponential, t_3, was originally set to conserve impulse but as the calculations only run to 75μsec, not all the impulse has been delivered at large distances from the axis. This problem was resolved quite satisfactorily (as shown in the many comparison plots of Section 3.3 and Appendix A) by not allowing t_3 to assume a value less than 10μsec. By setting $t_3 = 10$, the pressure wave form is completely defined and the equation for impulse is not needed to generate the loading forces, a useful simplification for some finite element codes.

3.2 Adjustments to the Basic Analytic Models

The analytic fits of Figure 4 are in general agreement with the data, however, there are a number of inconsistencies which can be accounted for by minor adjustments in the model. For example, the arrival times of the peak signal, t_2 are consistent with a wave traveling at the shock speed of water (~1.6 km/sec) for all cases, including the foam backed (see Section 6) and the rigid wall calculations (the bounding cases). However in *all* of the calculations for .635 cm thick panels, an early signal, becomes noticeable about 5 cm from the impact point and grows in magnitude with distance so that it dominates the wave form beyond about 6 cm ranges, Figure 11. This wave appears to be moving about 2.3 km/sec, initially, but slows to about 1.1 km/sec after

20
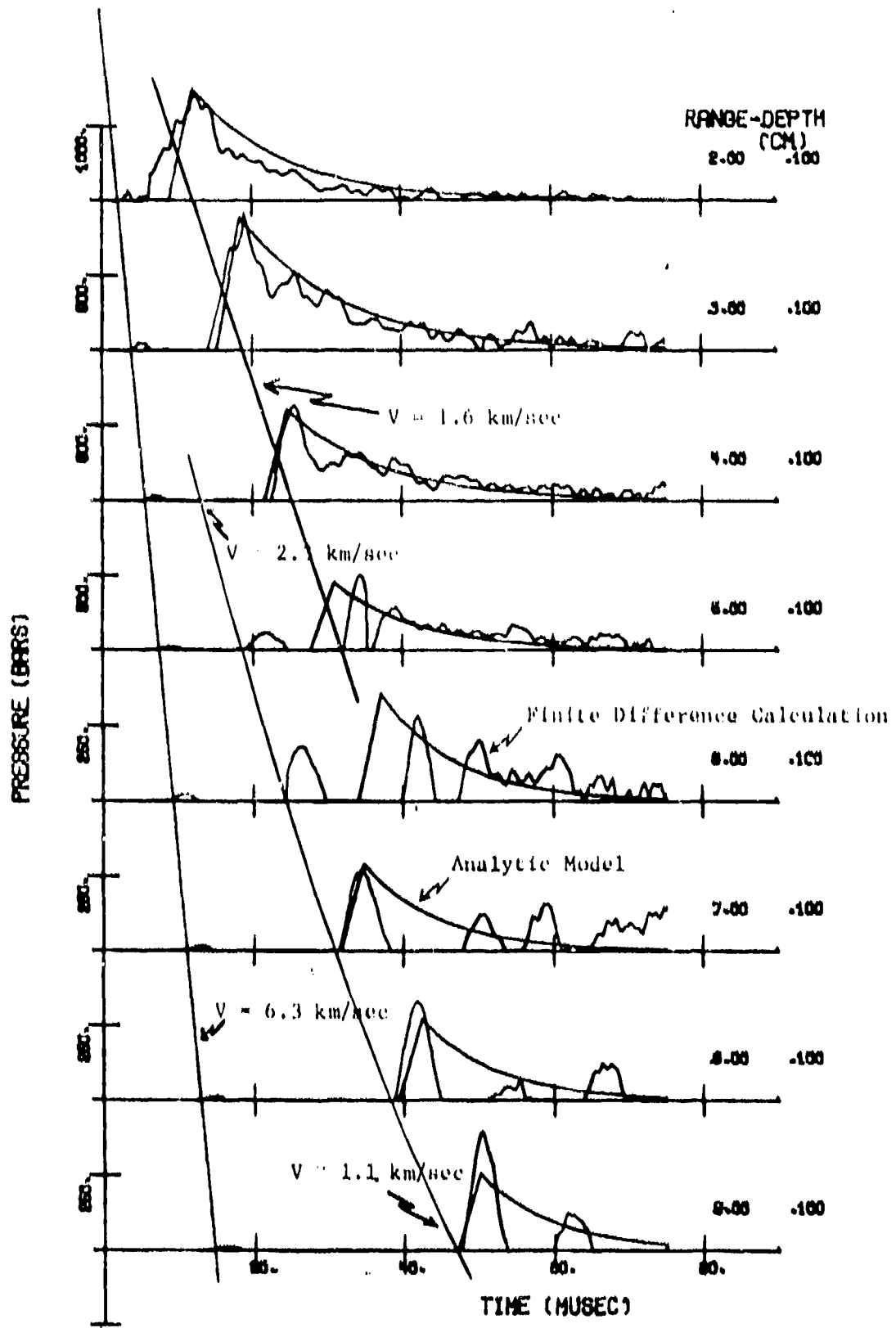
Figure 11. Comparison of the Analytic Fits with the
pressure time histories to 75μsec for points
.1 cm behind the front panel for 7L1.63, between
2 and 9 cm from the point of impact.

21

reaching its peak. The arrival of a significant pressure pulse
at about 35 μsec on the gauges located about 7.5 cm from the
point of impact in FD3 and FD8, two .635 cm thick panel shots,
is consistent with this calculated signal. The only plausible
source for this signal, which is not present in any calculations
or experiments with other panel thicknesses, must be complex
interactions of the front panel with the compressive and relief
waves in the water.

The strong shock in the water produces a wave in the thick
Aluminum panels which runs ahead and generates this leading
signal. This is best illustrated by comparing the pressure
contours (isobars) in four cases with a 1.4 cm diameter sphere
impacting at 1.63 km/sec. In the first, Figure 12, the front
surface was rigid (i.e., an infinitely thick plate) while in
the second, Figure 13, it was free (a zero-thickness plate).
The pressure contours in the rigid case are almost hemispherical
disturbed only by the motion of the fragment and the relief waves
originating in the cavity behind the fragment. By contrast,
although the front remains hemispherical, the contours in
Figure 13 clearly show the lower pressures along the front
surface due to the free surface boundary condition. Two calcu-
lations with finite thickness plates produced strikingly differ-
ent isobars. These are shown for the .158 cm plate in Figures
14 and 16 and for the .635 cm plate in Figures 15 and 17. The
interactions along the plate 13 μsec after impact, Figures 14
and 15, have produced a very low amplitude signal out to a
range twice as far as the main wave. This signal is quickly
damped in the .158 cm panel calculation, so that by 25 μsec,
Figure 16, the isobars again resemble those of the free surface
run, Figure 13. The thicker, .635 cm panel, however, appears to
reinforce this signal so that by 30 μsec (Figure 17), a signifi-
cant spreading of the pressures is evident along the front surface.
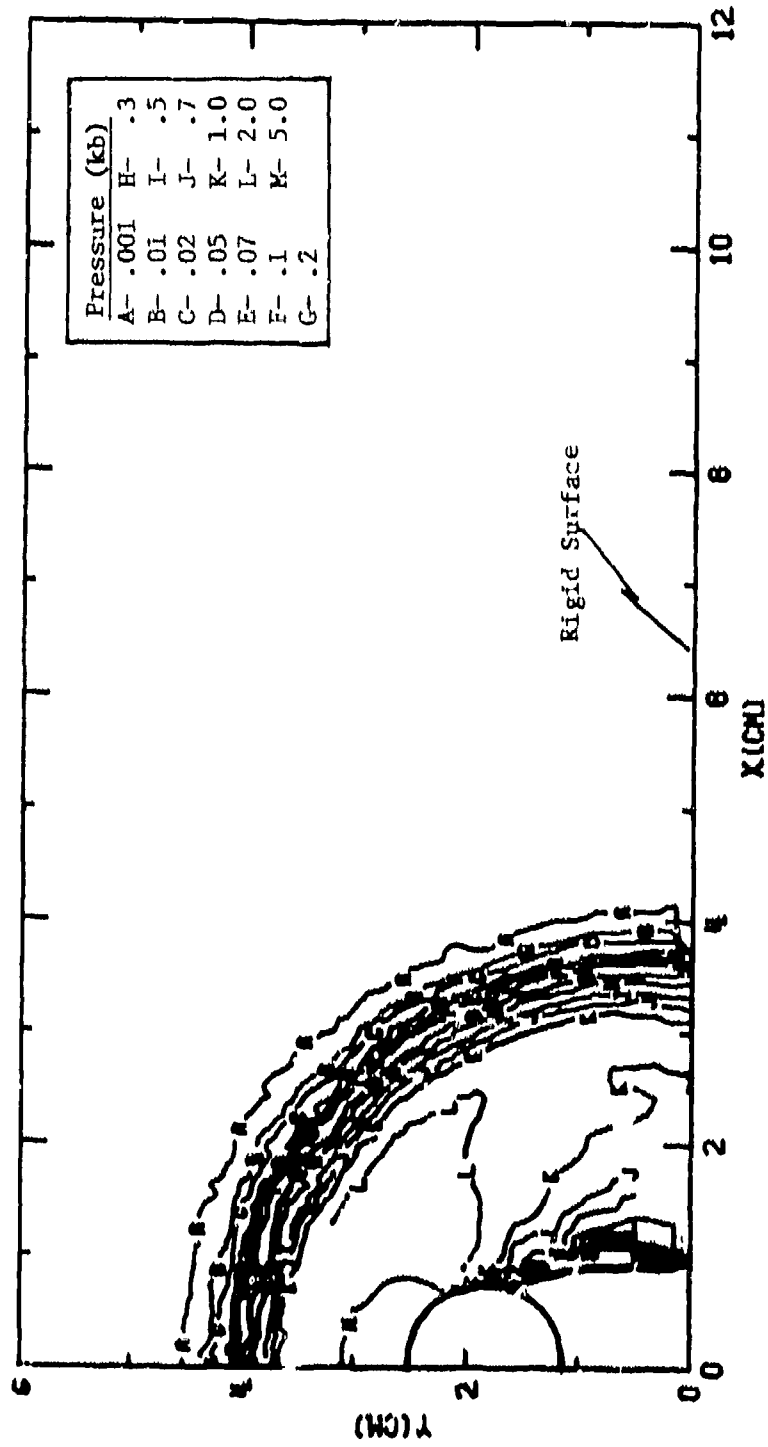
Figure 12. Isobars at 17μsec for KL1.63, the case with a 1.40 cm diameter sphere impacting at 1.63 km/sec into a tank with a rigid front surface.

23
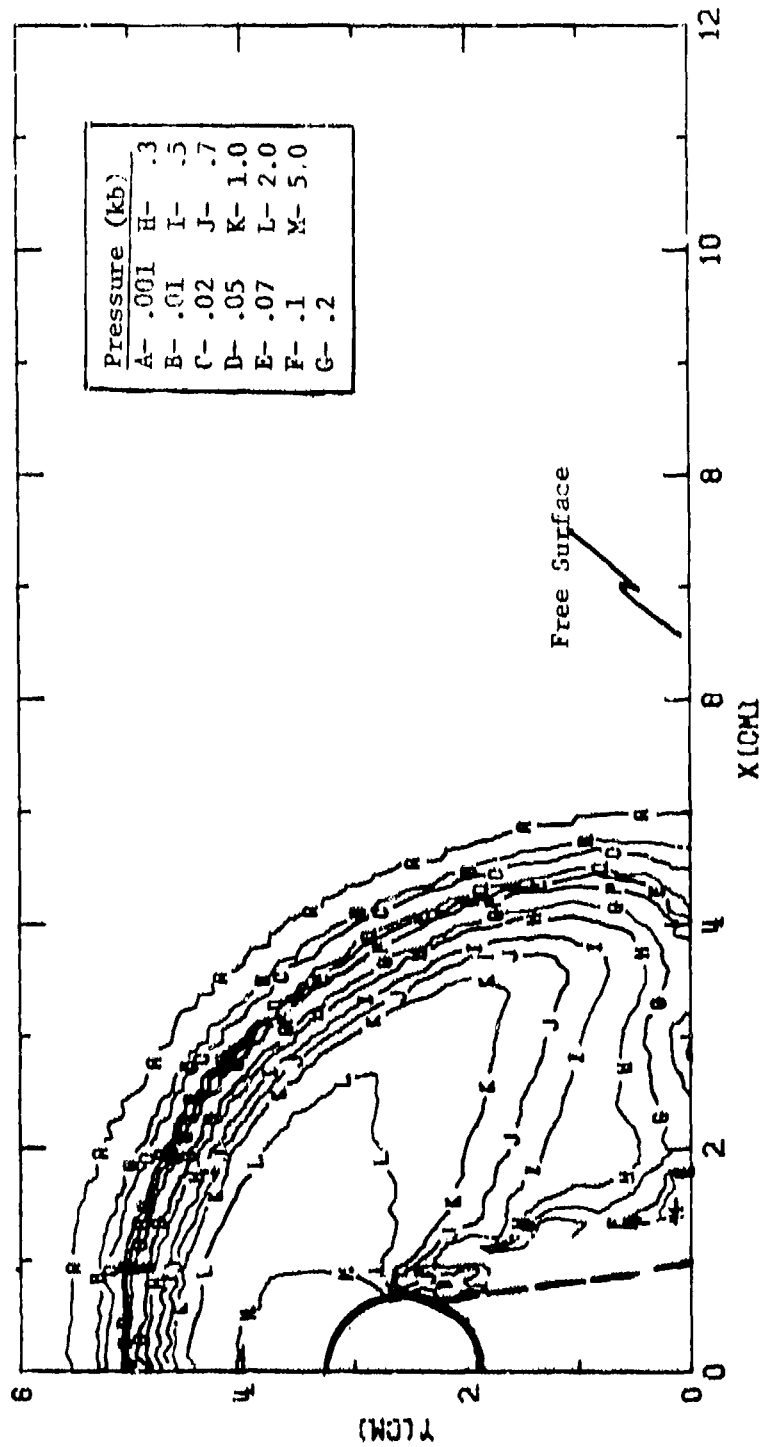
Figure 13. Isobars at 21μsec for 7LF1.63, the case with a 1.40 cm diameter sphere impacting at 1.63 km/sec into a tank with a free surface boundary condition at Y = 0.
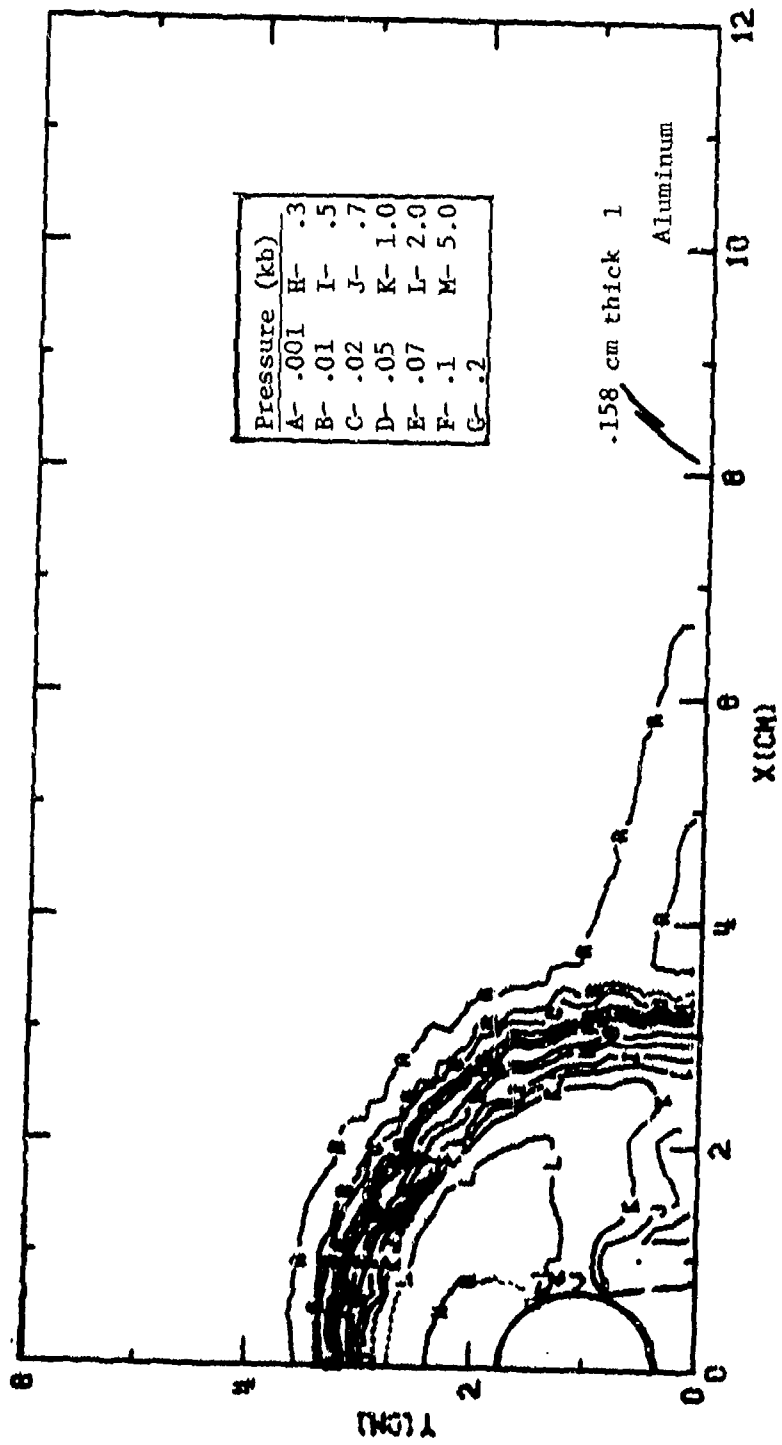
Figure 14. Isobars to 13μsec for 7L1.63, the case with a 1.40 cm diameter sphere impacting at 1.63 km/sec, into a tank with a .158 cm thick Aluminum front panel.

25
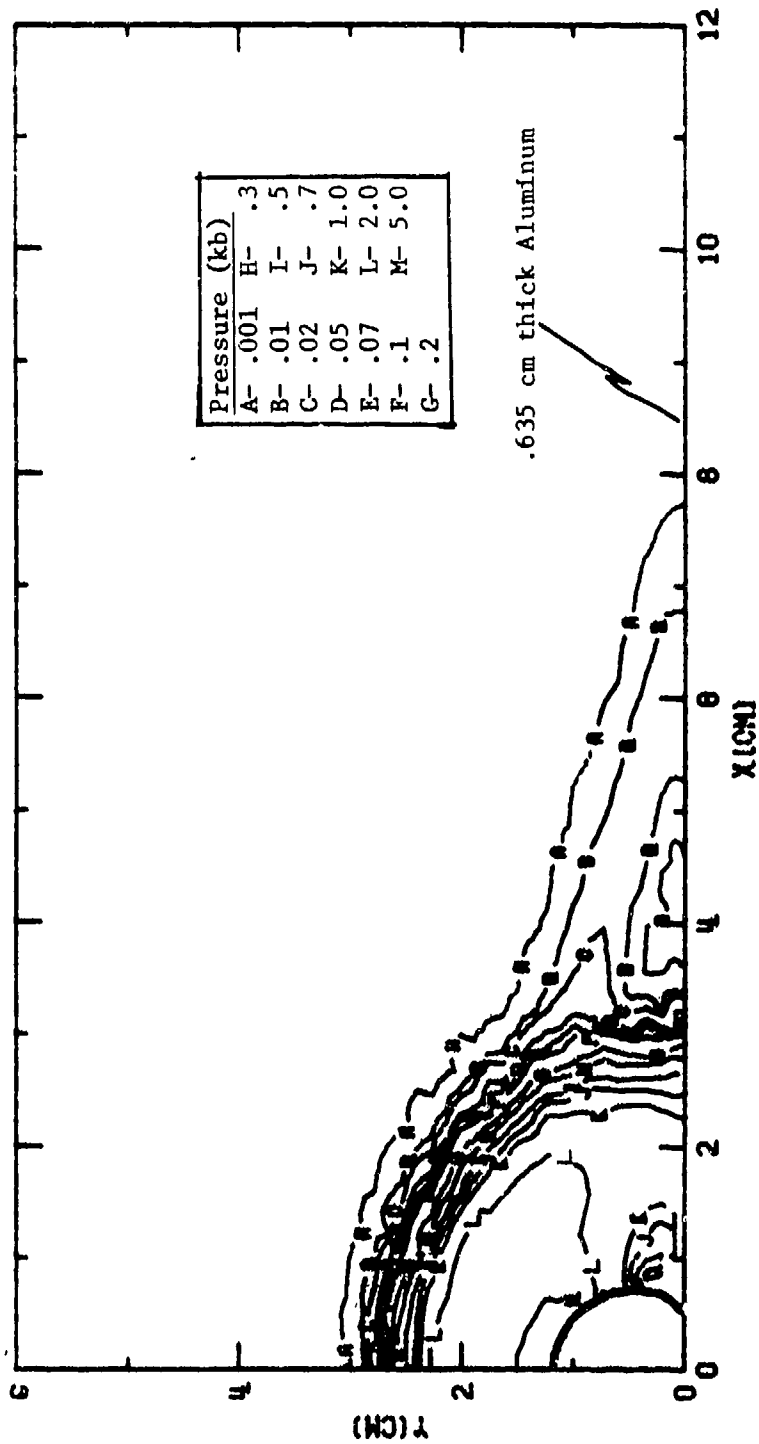
Figure 15. Isobars at 13μsec for 7L1.63, the case with a 1.40 cm diameter sphere impacting at 1.63 km/sec into a tank with a .635 cm thick Aluminum front panel.

26
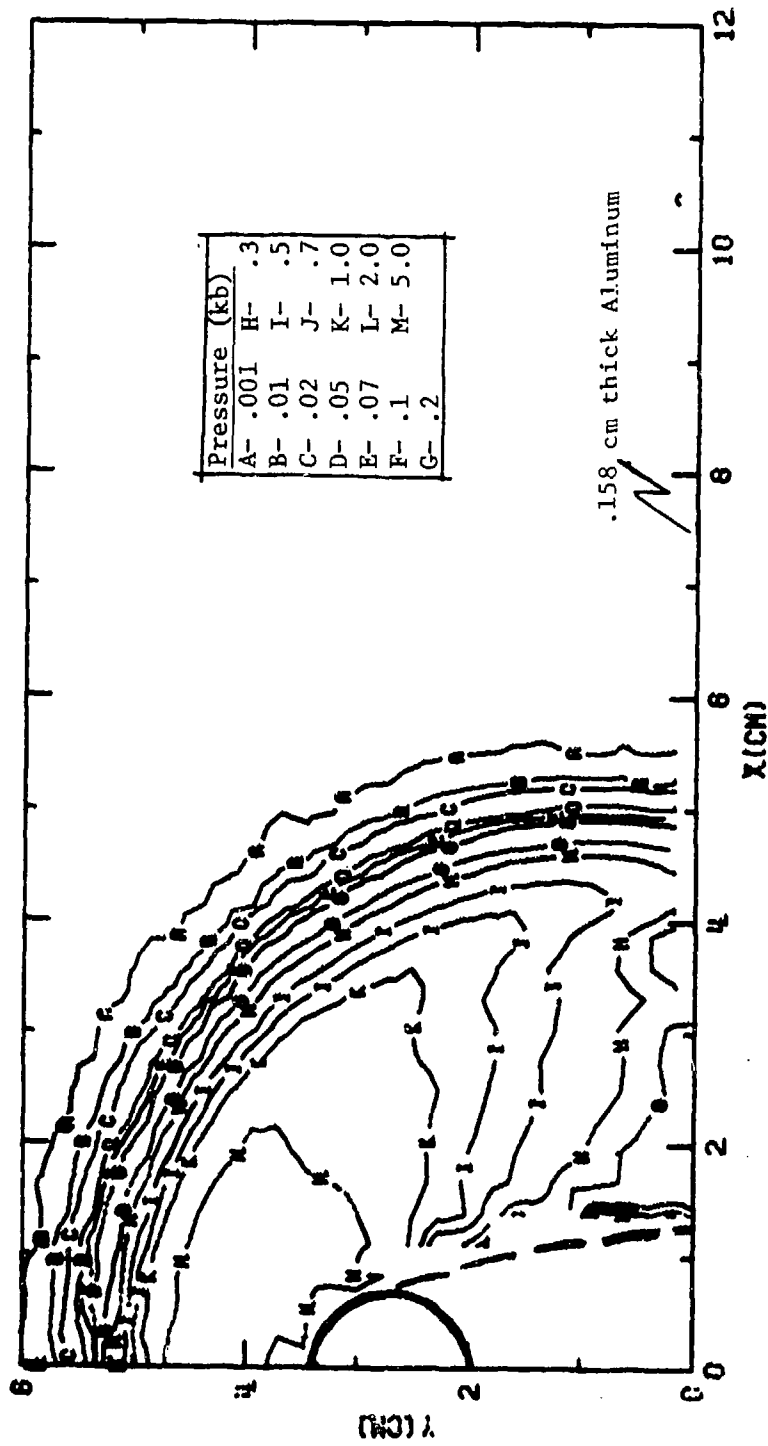
Figure 16. Isobars at 25μsec for 7L1.63, the case with a 1.40 cm diameter sphere impacting at 1.63 km/sec into a tank with a .158 cm thick Aluminum front panel.

27
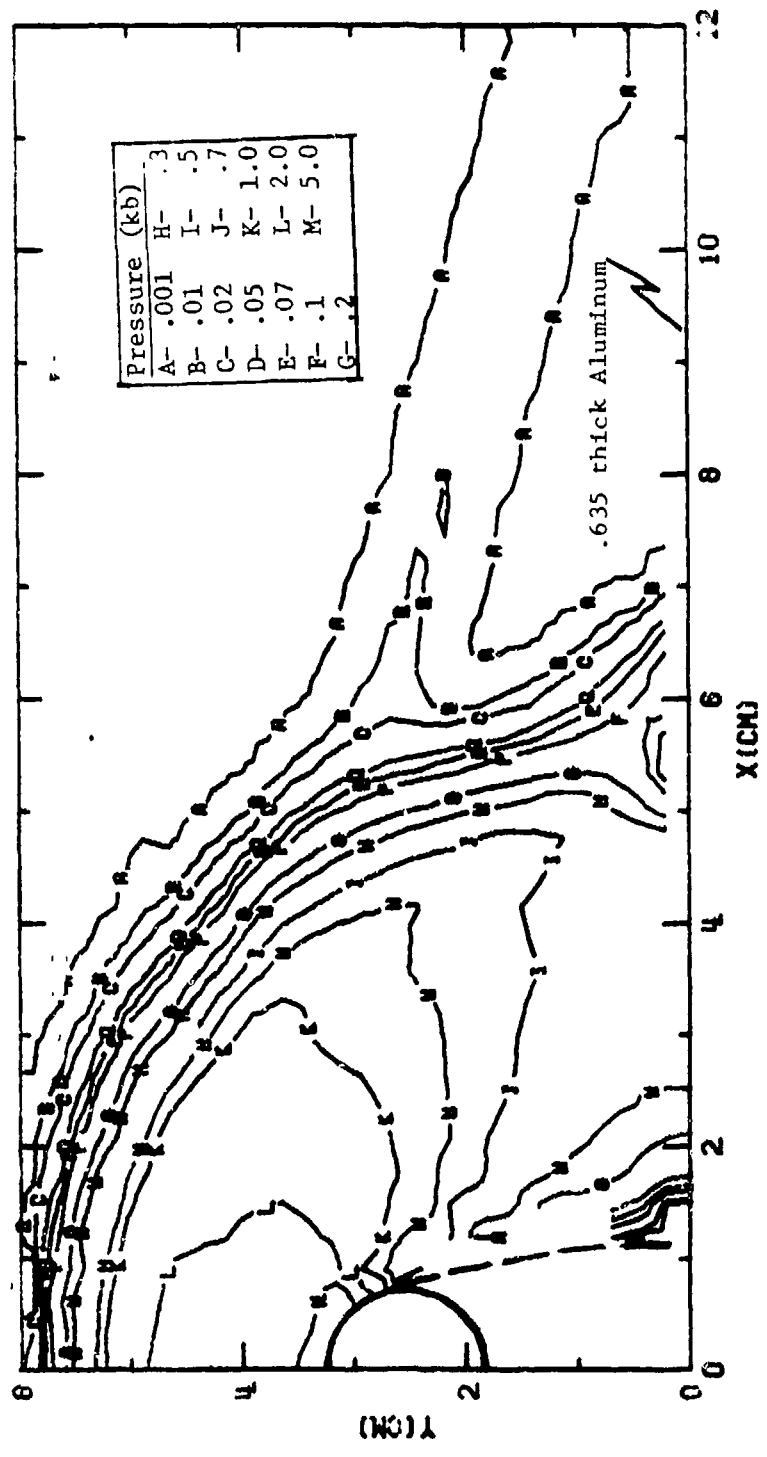
Figure 17. Isobars at 30μsec for 7L1.63, the case with a 1.40 cm diameter sphere impacting at 1.63 km/sec into a tank with a .635 cm thick Aluminum front panel.

28

The plate interaction is also demonstrated in Figure 18, in which the original motion (and accompanying pressure spike) at a range of 7.5 cm in the 7L1.63 calculation is directed into the tank and produces the leading pulse at 40μsec. No corresponding inward motion is present in 7S1.35 where the first peak occurs at about 48 μsec. Thus, the pressure histories for 7L1.63 .1 cm behind the front panel (Figure 11), show a peak arriving at 5.0 and 7.0 cm simultaneously. (Note an initial pulse due to the shock wave traveling through the Aluminum can be seen as a very early, low magnitude blip on each of the records). To account for the early arrival in the .635 cm panel, the analytic functions were shifted by recomputing t_2, thusly:

$$t_2 = (R-2.5)/.13 \text{ for } \begin{cases} R \le 6 \text{ cm} \\ \omega = .635 \end{cases} \qquad (12)$$

A second difficulty with the analytic fits appears in the deviation of the calculated data from the fits at R/R_p greater than ~10. Since the calculations were terminated at 75 μsec, the data at large ranges are not complete. However, a definite change in the slopes of the data is apparent. A possible explanation of this shift would be a change in the driving mechanism from the initial shock wave to the drag pressure. The decay of the peak pressure with ~1/R in Equation 3 is consistent with a point source for the energy. If the drag dominates beyond $R/R_p = 10$, a falloff as $\sim\sqrt{R}$ (as would be expected from a line source) might be more appropriate. Such a change was incorporated in comparing with the experimental data (Section 3.3 and in Figure 18 and Appendix A). With these revisions, the analytic model of pressure may be restated as follows:

$$P = 3.68 \, V\delta(R'/R_p)^{-a}$$

where $R' = \text{minimum of } (R, 10) \text{ and } \delta = \sqrt{R'/R} \qquad (13)$

29
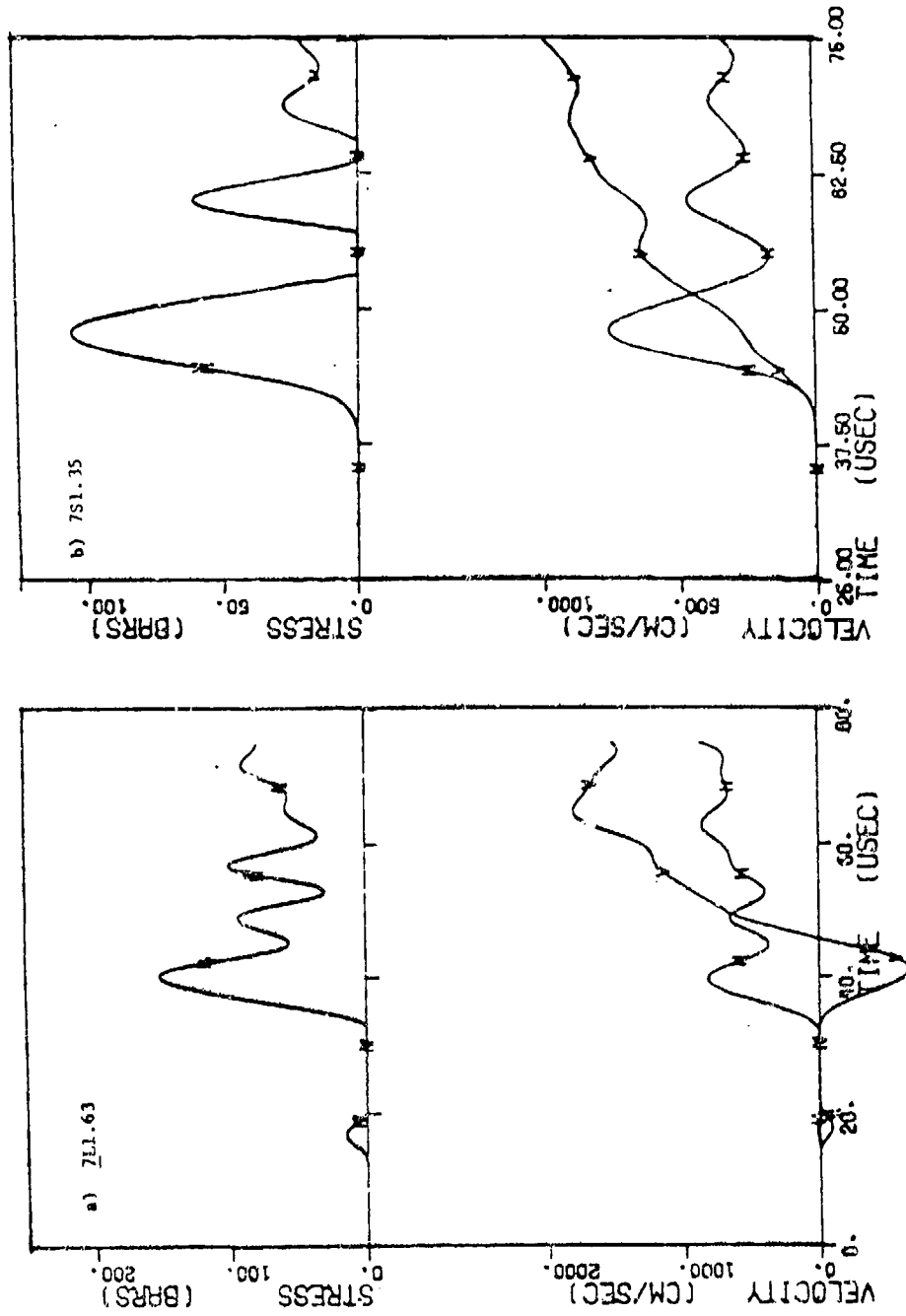
Figure 18. Velocity and Pressure versus time at a point 7.5 cm from the impact and, b) and into the tank for the two cases with .635 cm (7L1.63) and .158 cm (7S1.35) front panel. A positive velocity represents motion away from the impact (H) and out of the tank (V).

30

3.3 Comparisons with Experimental Data

Experimental pressure time histories were obtained from UDRI[3]
for five tests. Two, FD3 (7L.135) and FD8 (7L1.63), are directly
comparable with calculated pulses. The calculated and measured
pressure profiles at 7.5 cm range, .6 cm depth for 7L1.63 are
compared in Figure 19. Comparing arrival times, the calculation
misses the initial 200 bar pulse completely but matches the next
three quite well. The calculated peak pressure, 151 bars, is
about 30% lower than the measured value (210 bars). The differ-
ences in peaks may be attributed to several sources, both calcu-
lational and experimental. First, the rounded nature of the cal-
culated wave forms suggests that the calculational grid (~.25 x .30 cm
near this station) was still too crude to resolve the very steep
rise and fall of the actual pulses. Second, although the pressure
gradient with range, as illustrated by the wave forms at 7, 7.5
and 8 cm, Figure 20, is negligible and actually increases with
range, the changes with depth into the tank at the 7.5 cm range,
Figure 21, is quite large. The calculated peak pressure at .1 and
2.0 cm depths are 282 and 306 bars, respectively; both considerably
higher than the 151 bars calculated at the .6 cm depth. Thus,
a shift in the position of the experimental gauge of as little as
.2 cm could have resulted in a change in peak equivalent to the
difference between the experiment and calculation shown in Figure
19 model. The analytic model, since it was derived for loading
the front panel, gives a value of 282 bars, consistent with the
.1 cm value but much higher than the experimental data at .6 cm.
The large pressure gradients close to the front panel and the
apparent increase of pressure with increasing range are distress-
ing since the limited data which can be obtained in the experi-
mented tests are only representative of a few unique points. Data
from similar locations in different shots may produce widely
varying results related more to the exact locations of the guages
than differences in the input parameters.
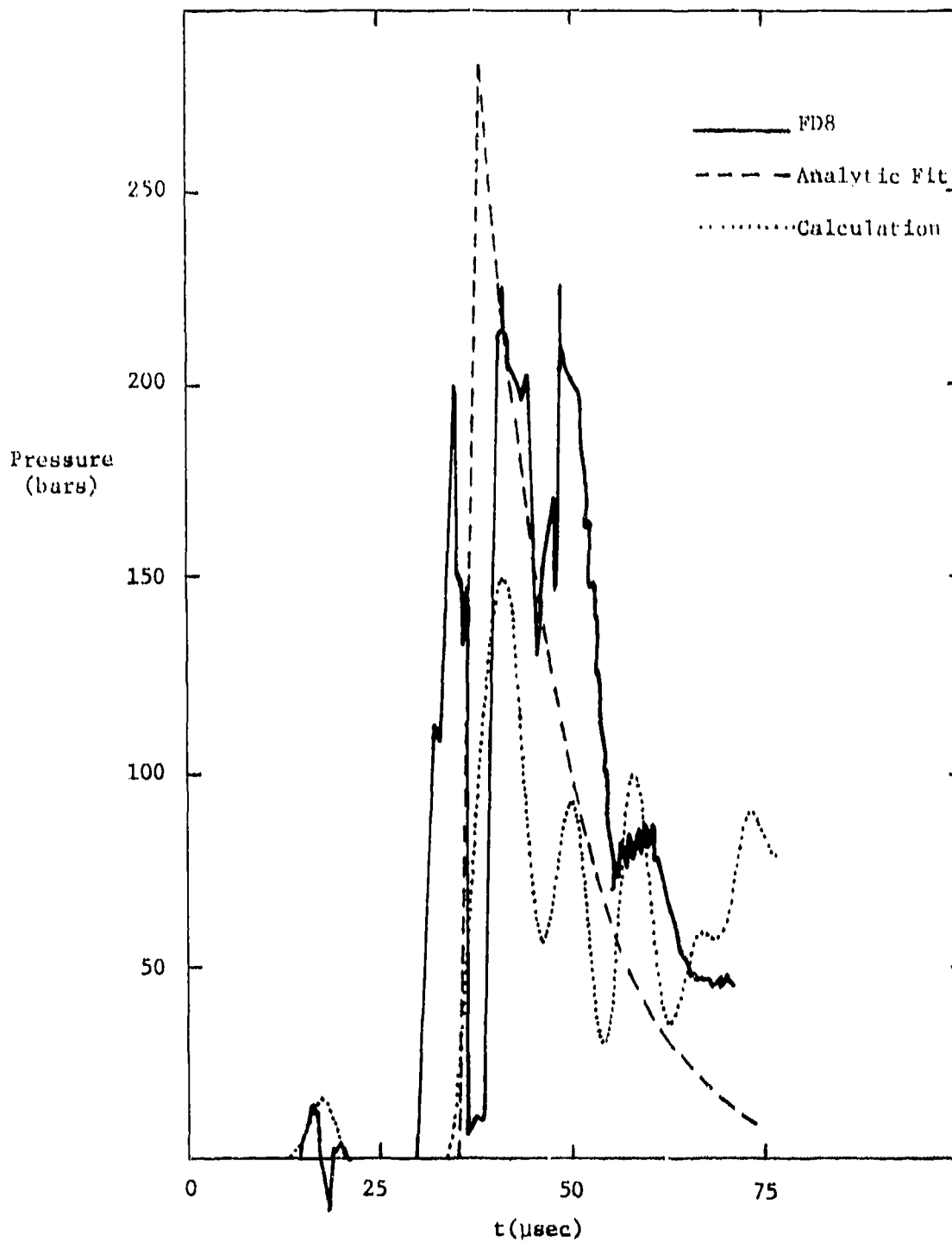
Figure 19. Early pressure time history for 7L1.63, 7.5cm
from the point of impact and .6cm behind the
front panel as measured (FD8), calculated and
fit by the equations of Fig. 4.

32
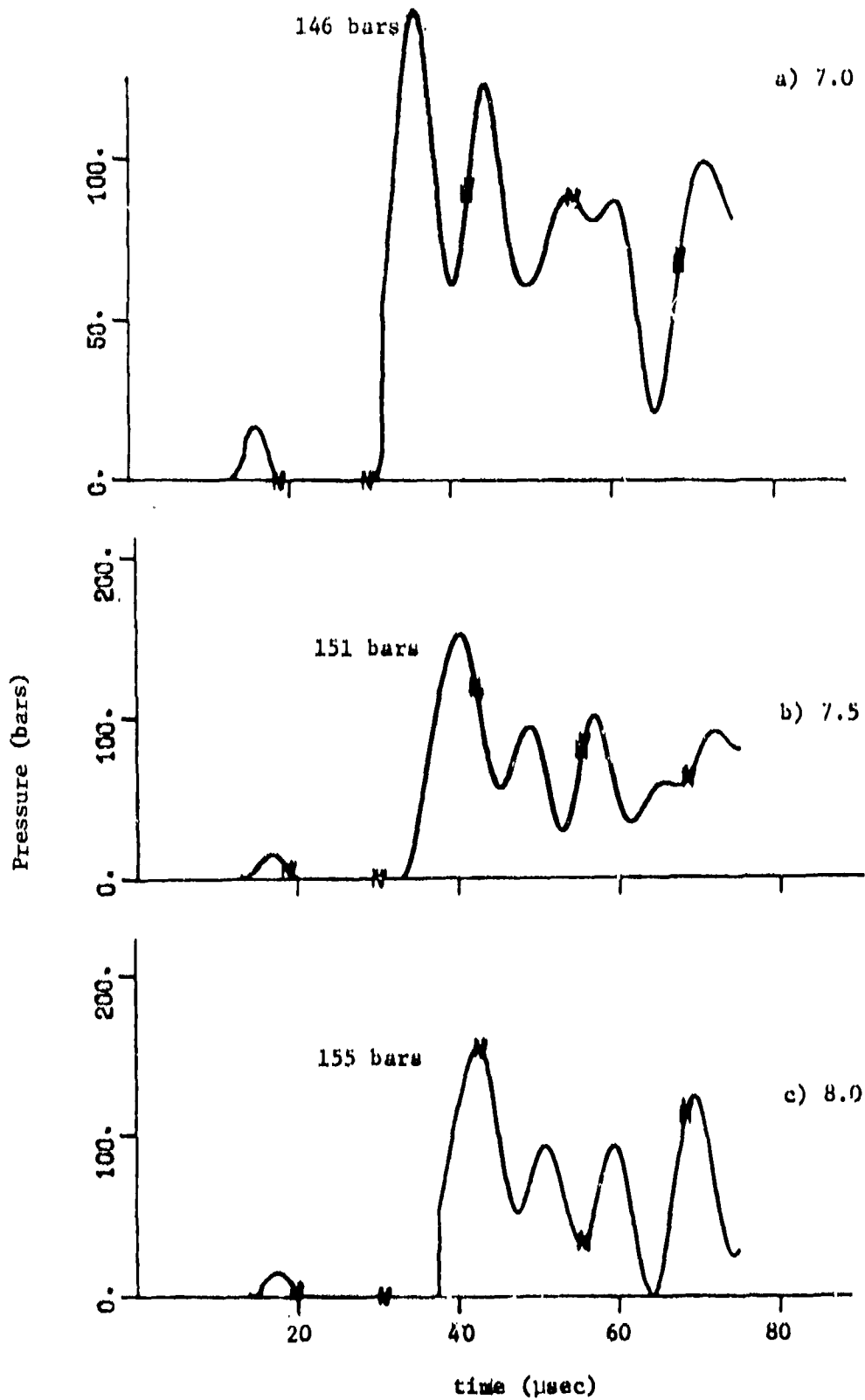
Figure 20. Pressure time histories calculated for 7L1.63 at ranges of 7.0, 7.5 and 8.0 cm from the point of impact, .6 cm behind the panel.

33
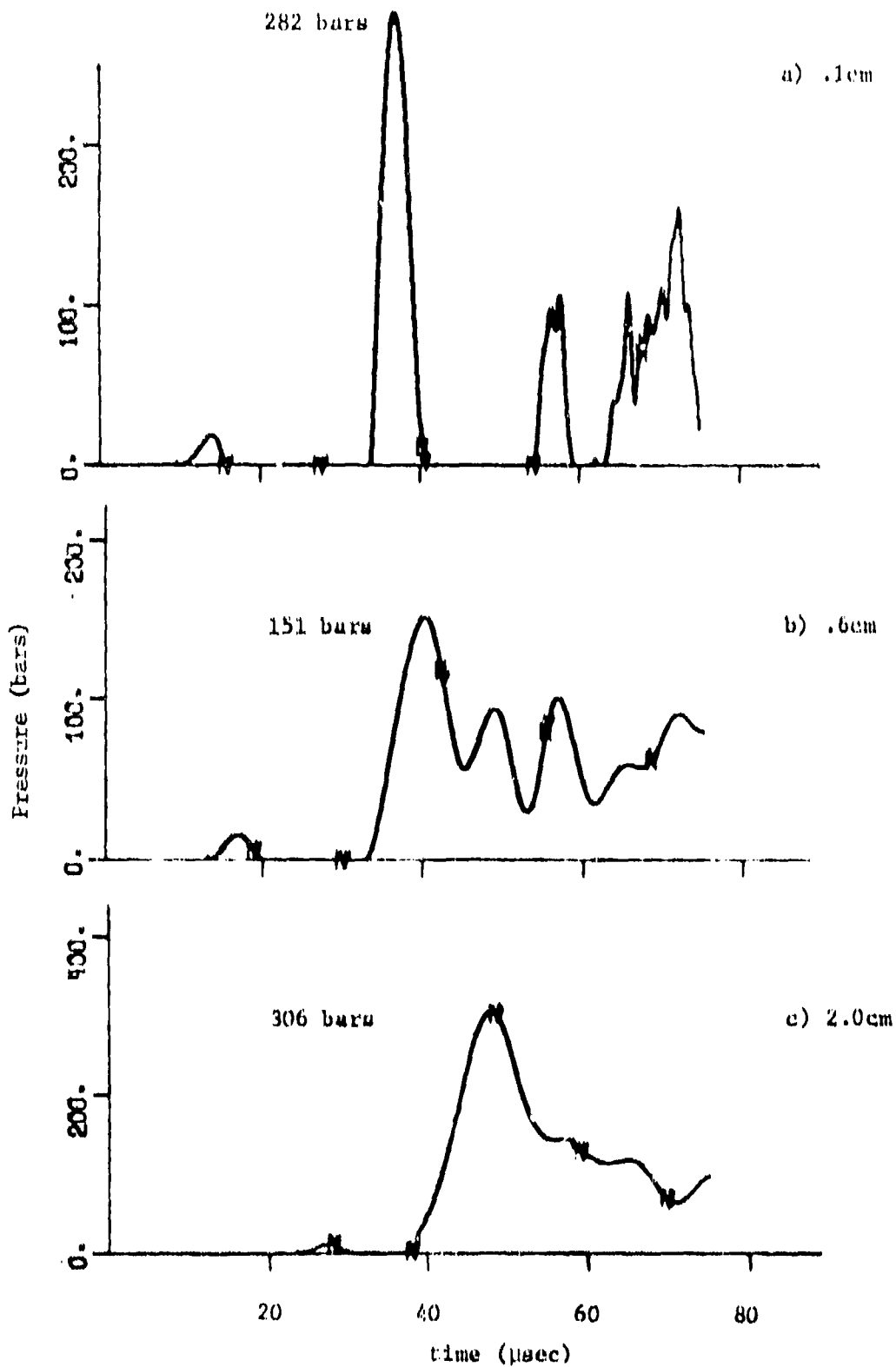
Figure 21. Pressure time histories calculated for 7L1.63, 7.5 cm from the point of impact, .1, .6 and 2.0 cm behind the front panel.

Experimental pressure wave forms at 7.5 and 10 cm ranges from FD23 (7S1.35) are compared with the analytic function and the calculated output at the .1 and .6 cm depths in Figure 22. Again the calculated peaks are lower than the measured values. The difference between the calculated peaks at .1 and .6 cm is much less than for 7L1.63, since the .158 cm front panel in 7S1.35 does not reflect the signal as well as the four times thicker panel (.635 cm) in 7L1.63.

The measured pressure profiles at 7.5 and 10 cm are compared with the analytic models for three shots without corresponding calculations, FD3 (7L1.47), FD15 (7S1.98) and FD25 (GS1.46 - shot with a .476 cm thick graphite-epoxy front panel) in Figures 23, 24 and 25, respectively. For 7L1.47, the analytic peak is 40% too high and arrives between the double peaks of the experiment. The calculated impulse to 80μsec, however, is only about 30% higher than that measured. The analytic pressure for 7S1.98 at 7.5 misses the initial peak by a factor of two and arrives almost 5 μsec late thereby greatly underestimating the impulse. The profile at 10 cm, however, although still several μsec late, is much closer to the data and the impulse delivered is about right.

The GS1.47 comparisons, Figure 25, are, perhaps, the most interesting, since the front panel is of a very different material, i.e., graphite-epoxy. The waves at 10 cm appear to differ mainly by a 5 μsec time shift, while the rapid drop in the measured profile after the initial peak at 7.5 cm leads to too large an analytic impulse at that range.

It appears that each of the comparisons of the fit with specific measurements show discrepancies. However, there are not consistent differences which would indicate a specific oversight. Rather, the changes in wave shapes as a function of depth shown in Fig. 21, suggest the major source of the differences may be the uncertainties in the position of the gauge relative to the front panel.

35

a) 7.5 cm from impact

Distance Behind
Front Panel (cm)

FD23   .6
Calc   .6
Calc   .1
Fit   .1

P
(bars)

b) 10 cm from impact

P
(bars)
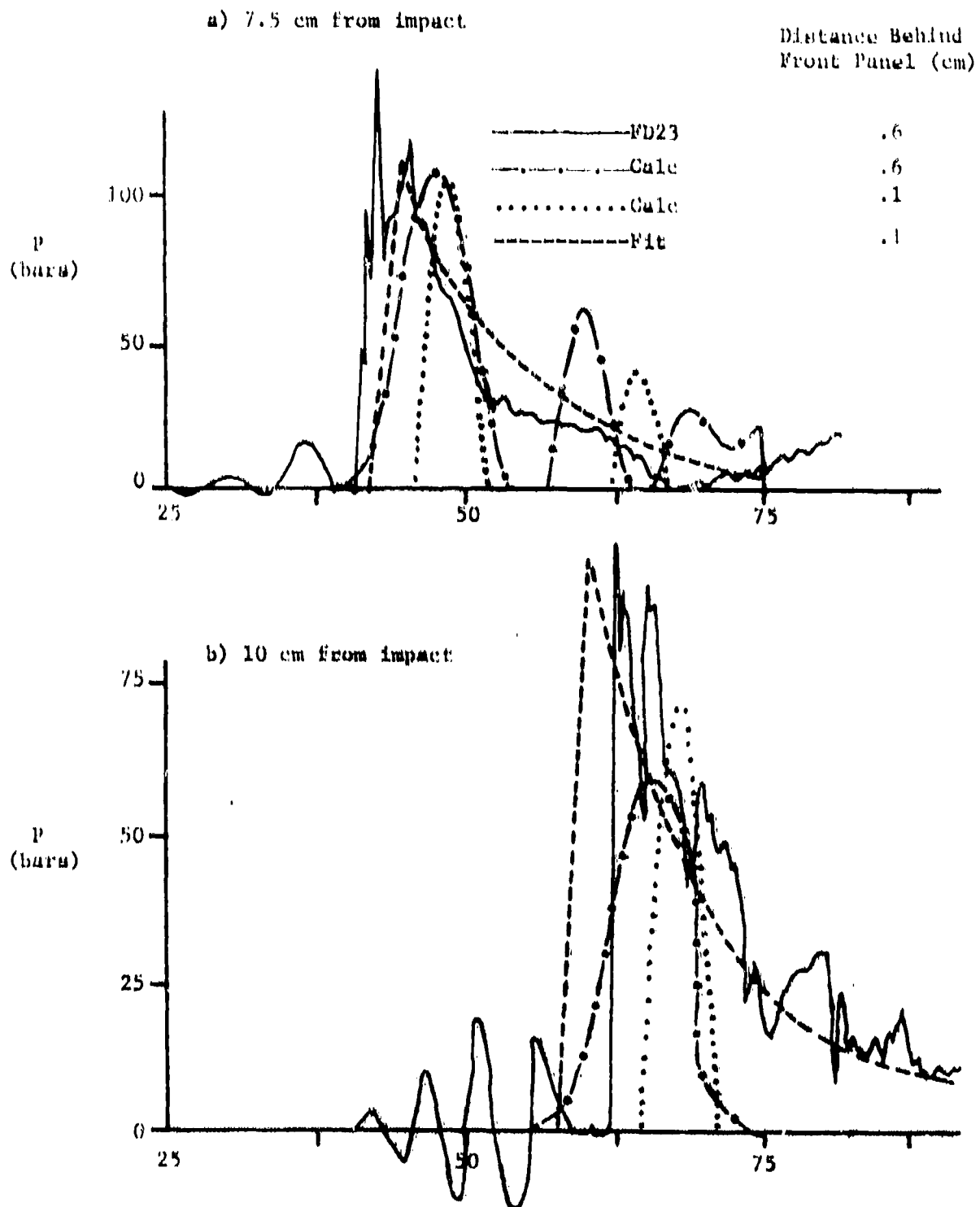
Figure 22. Comparison of the pressure time histories for
7S1.35 at 7.5 and 10 cm from the point of impact
(R_p = .55, w = .158, V = 1.35).
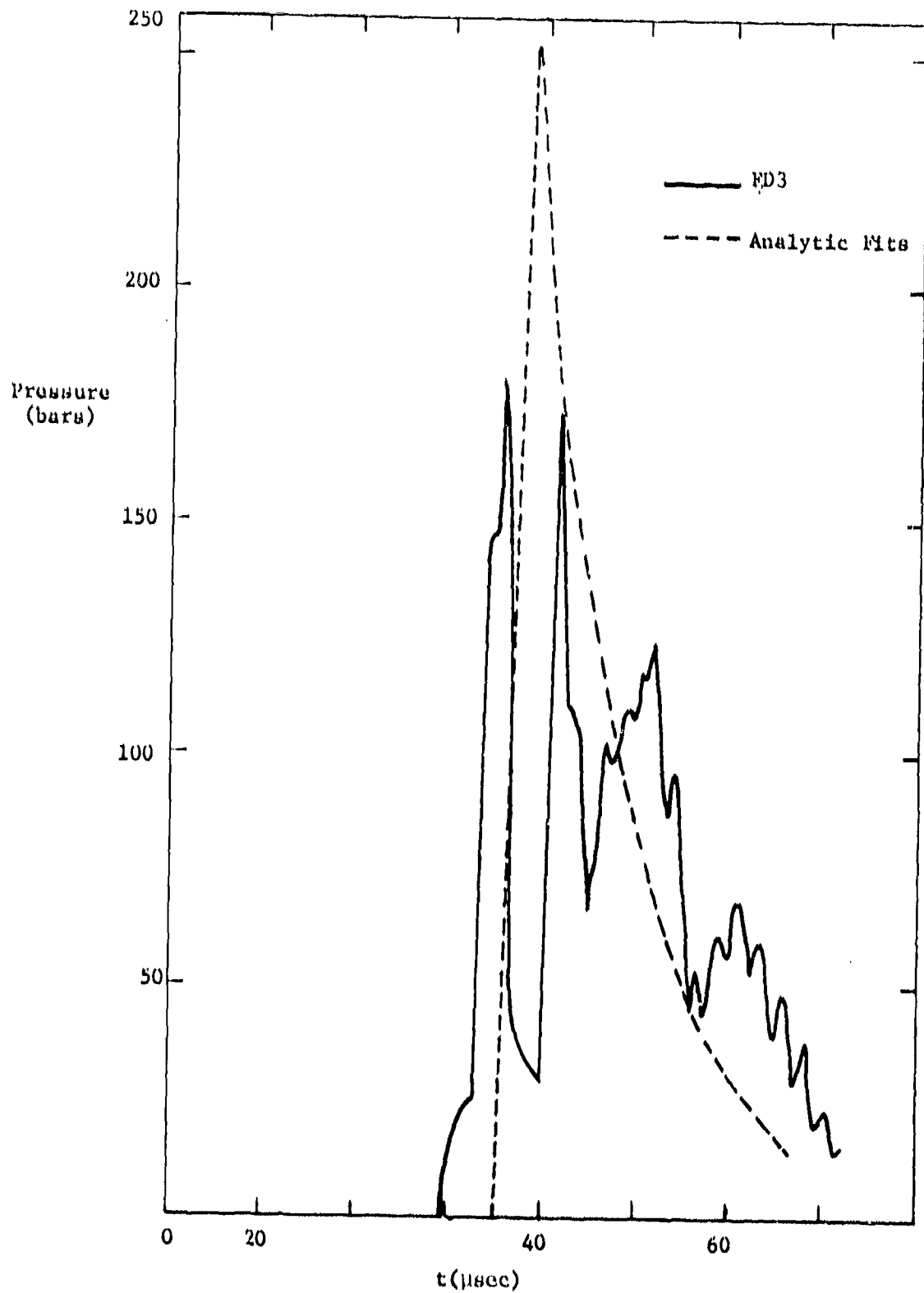
Figure 23. Comparison of the experimental (FD3) and analytical
pressure time histories for $\underline{7}$L1.46, 7.5cm from the
impact point, .6cm behind the front panel. (R_p = .70,
w = .635, V = 1.46).

37
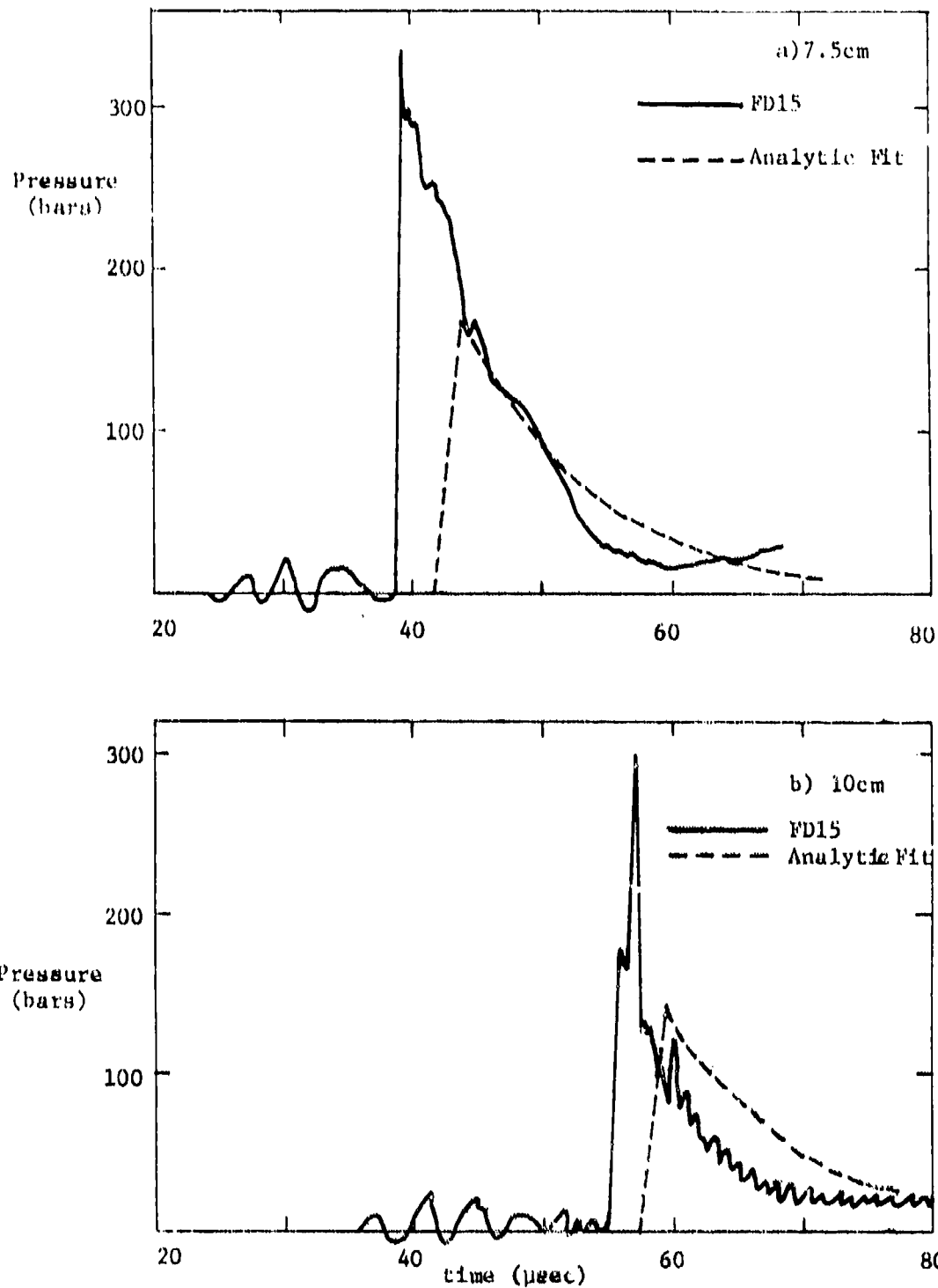
Figure 24. Comparison of the Experimental (FD15) and analytical pressure time histories for 731.98, 7.5 and 10 cm from the impact point, .6 cm behind the front panel. (R_p = .55, w = .158, V = 1.98).
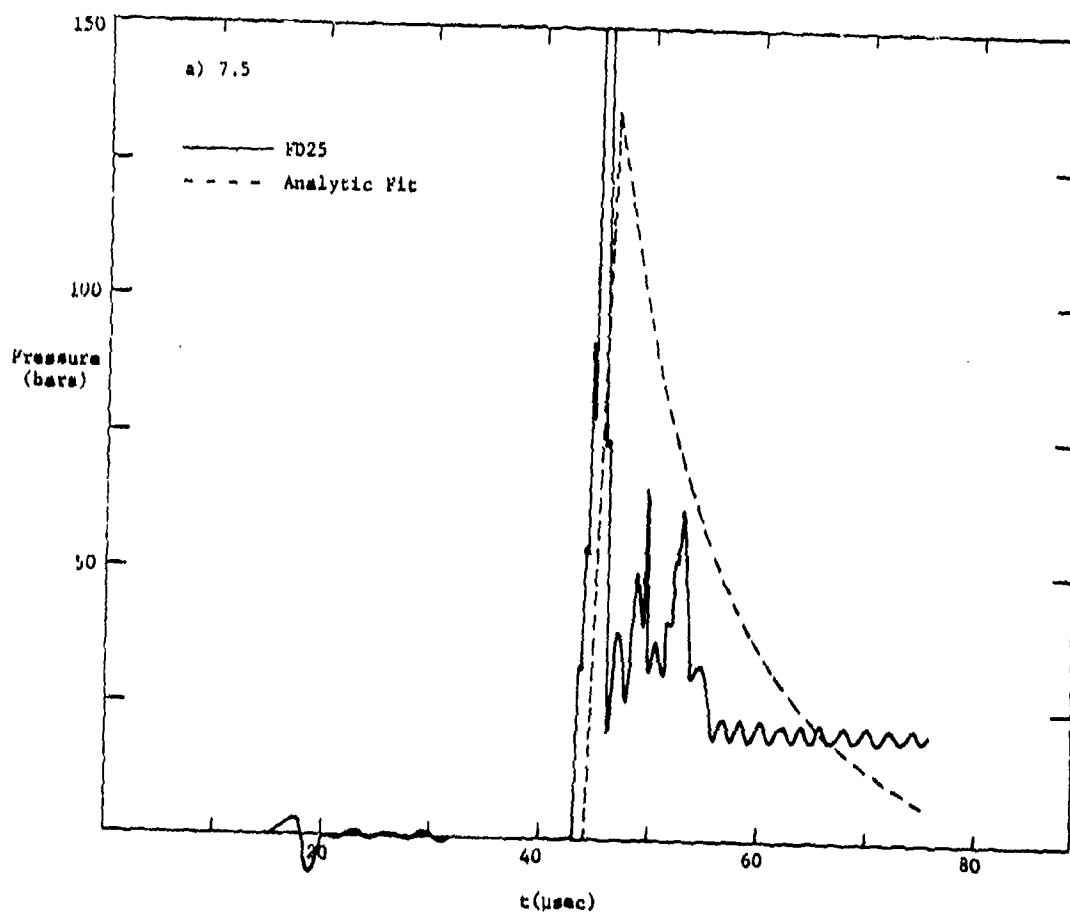
Figure 25a. Comparison of the experimental (FD25) and Analytic pressure time histories for GS1.46, 7.5 cm from the impact point, .6cm behind the front panel ($R_p = .55$, w = .476, V= 1.46, ρ = 1.28)

39
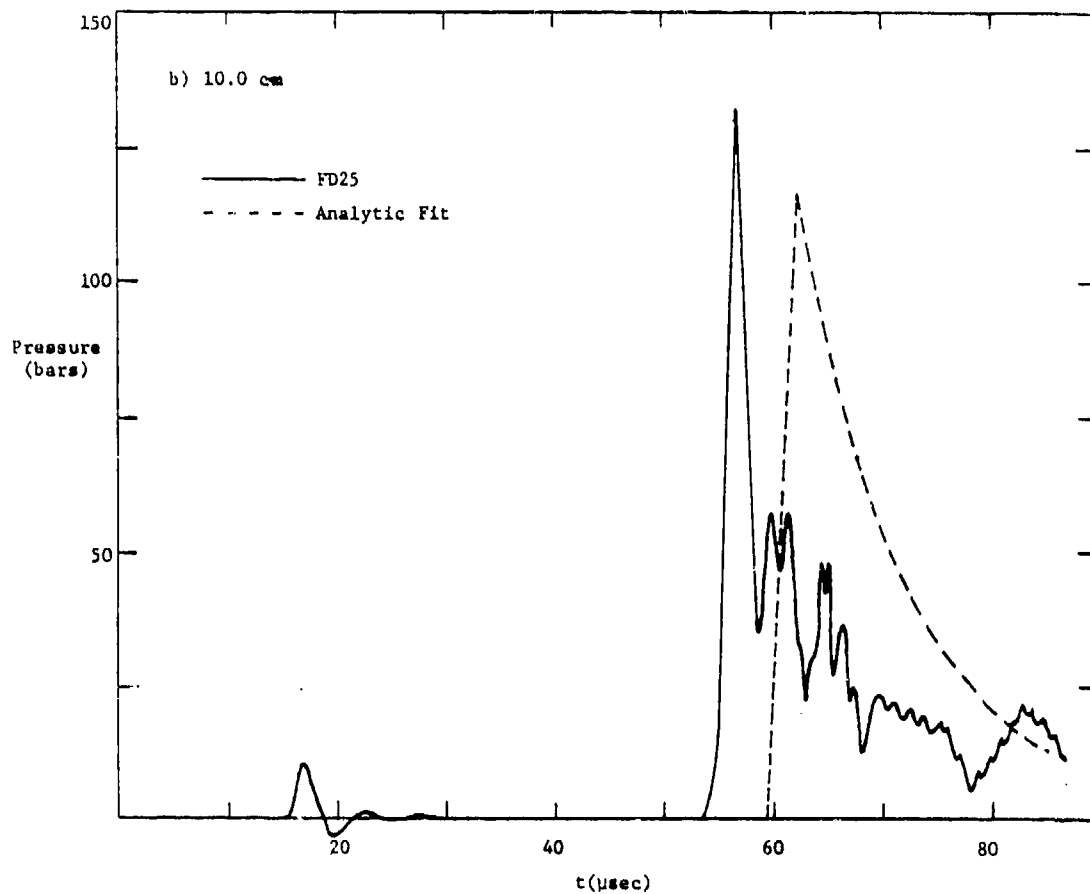
Figure 25b. Comparison of the experimental (FD25) and Analytic pressure time histories for GS1.46, 10 cm from the impact point, .6cm behind the front panel. $(R_p = .55, \quad w = .476, \quad V = 1.46, \quad \rho = 1.28)$

40

3.4 Relative Importance of the Parameters

Differentiating the natural log of P and I as given in equations 3 and 5 results in

$$\frac{dP}{P} = \frac{dV}{V} + \alpha \, \frac{dR_p}{R_p} - \frac{dR}{R} + .43\ln(R/R_p)\exp(-.72\rho\omega) \, d(\rho\omega) \quad (14)$$

$$\frac{dI}{I} = \frac{dV}{V} + \beta R/R_p \, \frac{dR_p}{R_p} - \frac{dR}{R} + .22^{R/R_p}\exp(-.63\rho\omega) \, d(\rho\omega) \quad (15)$$

Thus a change in V results in the same percentage change in both P and I, while the effect of changing the fragment size produces a larger percentage change in P since α is always greater than 1, but a smaller change in I, β being less than .55. In addition, the relative changes in P and I with fragment size are largest for the thin panels as both α and β have their maxima at $\omega=0$. The dependence of P and I on the panel areal density is more complex and cannot be characterized by equivalent percentage changes. However, for a fixed incremental change in $\rho\omega$, the relative changes in P and I will be greatest for the thinner panels. The coefficient of the $d(\rho\omega)$ term in equations 12 and 13 decreases from .43 to zero for P and .22 to zero for I at each R/R_p as the plate areal density increases from 0 to ∞. Thus thickening the front panel to increase its ability to withstand fractures also increases the forces it must withstand. However, an increase in plate thickness also reduces the values of α and β thus reducing the sensitivity of P and I to the size of the impacting.

41

SECTION IV.

NONSAP ANALYSIS OF ENTRANCE PANEL RESPONSE

4.1 Hoop Stress Profiles

The analytic functions (Equations 1 and 2) were used to provide the inner surface loading conditions for NONSAP finite element analyses of the entrance panel response. Figure 26 defines the geometry, boundary conditions, and material properties for these analyses. Bi-linear relationships were used to describe the elastic-plastic properties of the two aluminum alloys.

Figures 27a and 27b contain typical hoop stress vs radius ($\theta_{\theta\theta}$-R) profiles at a sequence of times. The highest stresses are seen to occur near the entrance hole at times between 30 and 120 μsec. By 200 μsec, the hoop stresses near the hole have dropped significantly, and the peak stress (which occurs at r~3cm) is well below the nominal material strength of 83 ksi. This indicates that if failure is to occur, it will initiate by formation of radial cracks near the hole at early times. This does not imply that failure is completed at early times or that stresses due to late time bulging are insignificant or unimportant. However, for panels in direct contact with the fluid, failure will start near the hole at early times because stresses in that region are the highest which will be experienced. The resulting cracks will propagate a few centimeters due to the early time loading. There will be large stress concentrations around the crack tips, so the lower intensity, late-time loading can usually propagate these cracks to ultimate failure of the panel.

(If the panel is not in direct contact with the fluid, as in the case of a foam-backed panel (Section 6), the early-time shock loading will be much less severe or even non-existent. In this situation, failure will occur only if the stresses induced by late-time loading and displacement are sufficient to initiate crack propagation).

ENTRANCE PANEL GEOMETRY:

Aluminum Plate

37.5 cm

r_o

Entry hole

END VIEW

rigid support
at 37.5 cm radius

τ

20 mm

F(r,t) determined
by CRALE analysis
of pressures in water
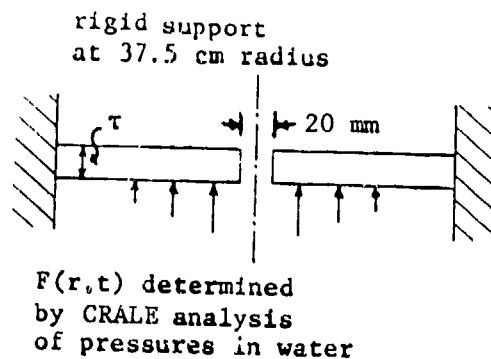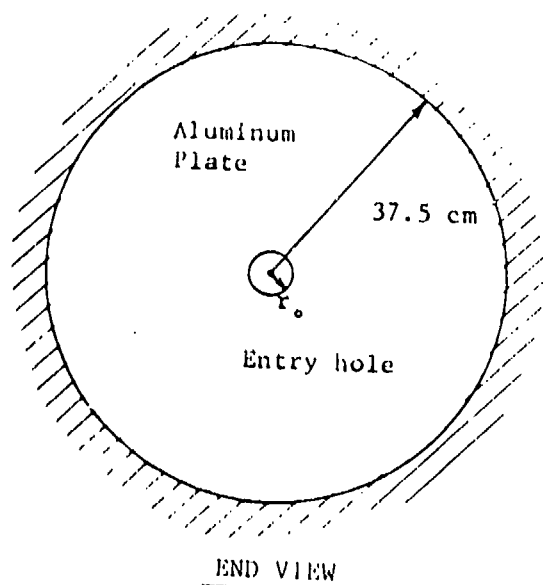
CROSS-SECTIONAL VIEW

ALUMINUM MATERIAL MODEL:

73

200
1

7075-T6

50

333
1

2024-T3

10.5 x 10³
1

11 x 10³
1

σ, kpsi

$\nu = 0.326$

ϵ, in/in
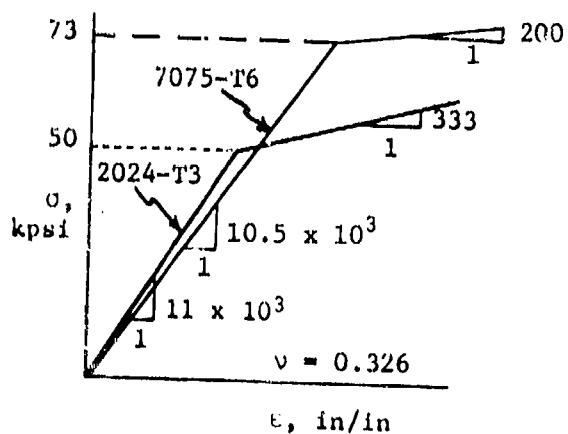
GRID SIZE:

τ	No. Elements	No. Nodes
1.6 mm	55	278
6.35 mm	36	183

TIME STEP:

$\Delta t = 2$ μsec

Figure 26. NONSAP Finite Element Axisymmetric Model of the Entrance Panel of the Fuel Tank

43
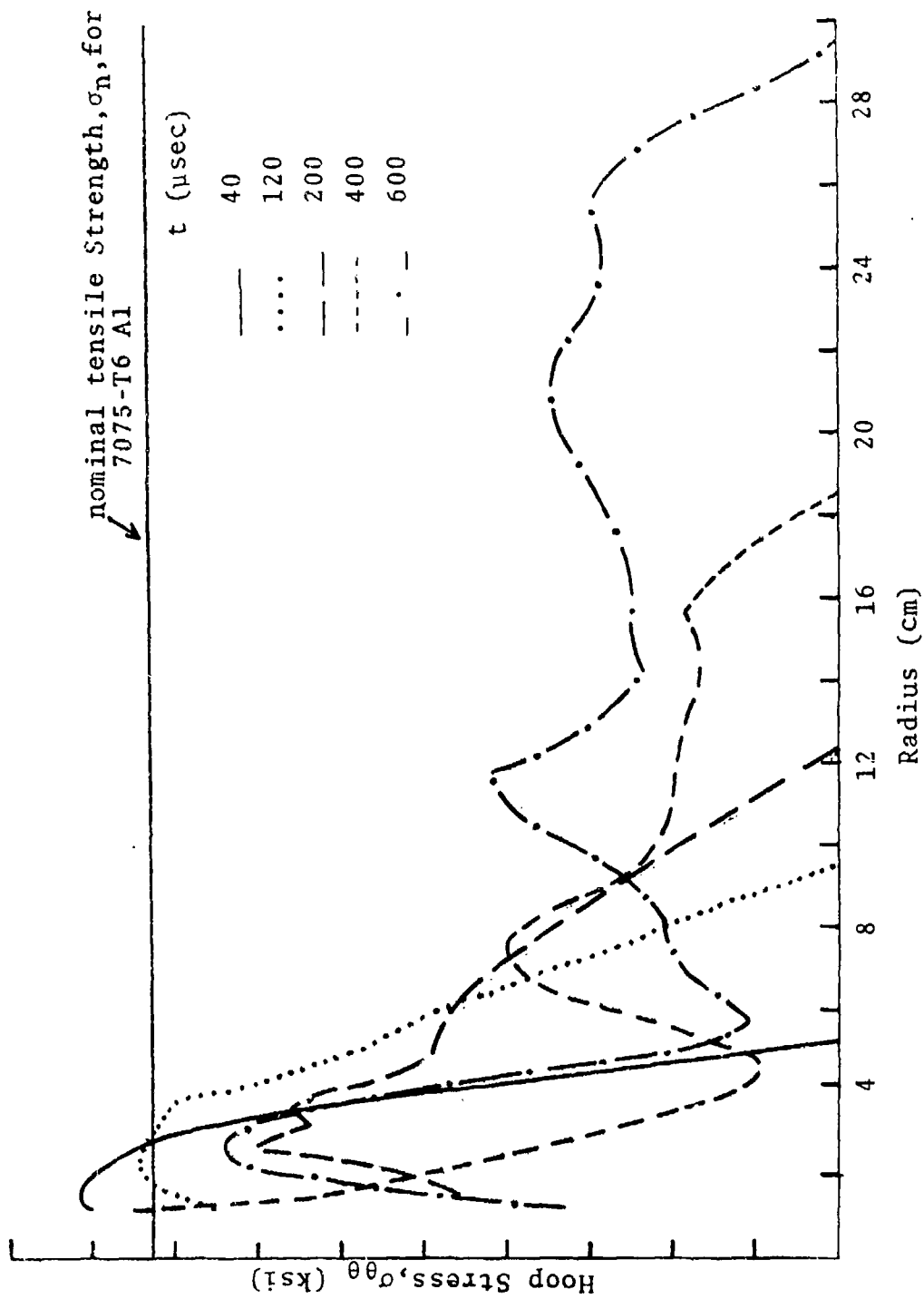
Figure 27a. Hoop stress, $\sigma_{\theta\theta}$, in entrance panel, case 7L1.60, 11.66gm steel sphere impacting at 1.6 km/sec into 1/4-in 7075-T6 Al panel.

44
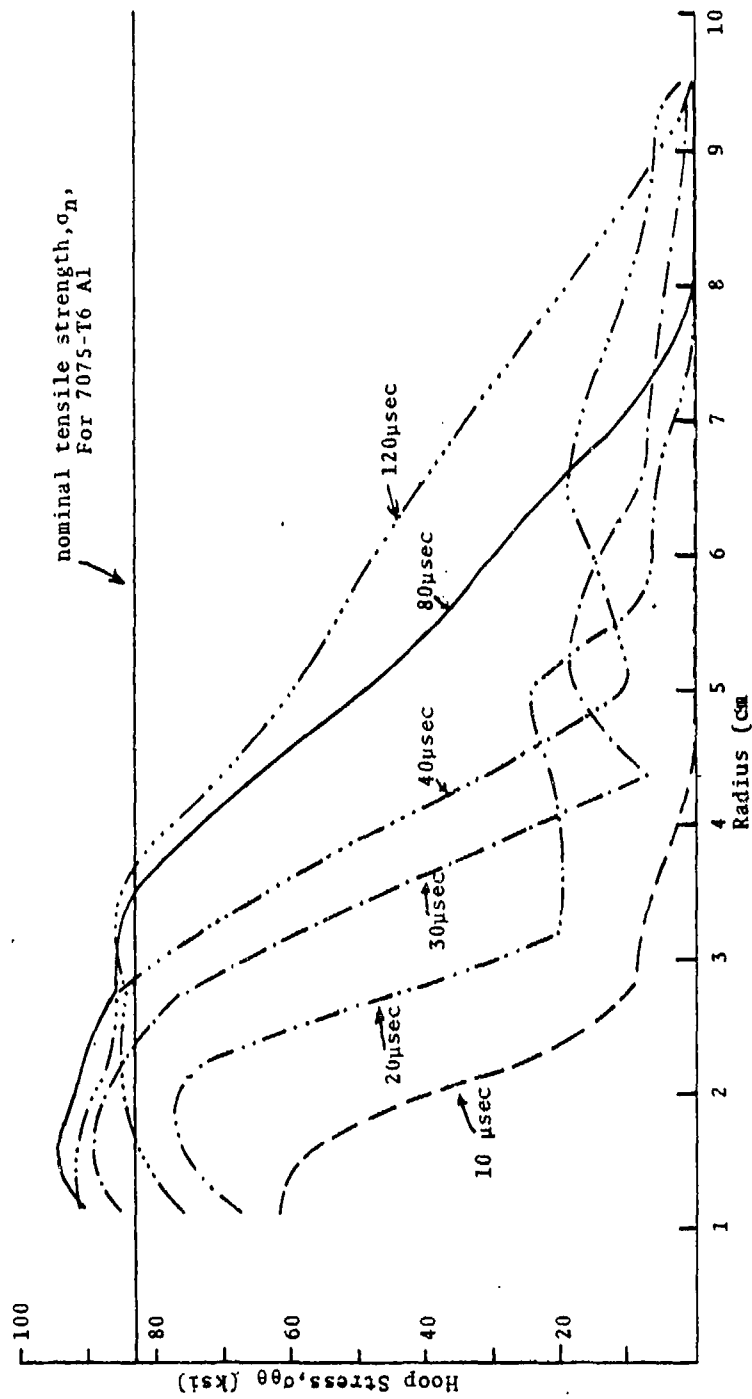
Figure 27b. Hoop Stress, $\sigma_{\theta\theta}$, in entrance panel, case 711.60, 11.66gm steel sphere impacting at 1.6 km/sec into ¼-in 7075-T6 Al panel

45

4.2 Method for Failure Prediction

Material failure (i.e. an abrupt drop in stress with in-
creasing strain) is not modeled in NONSAP, so it is necessary
to apply some criterion to the numerical results to determine if
failure is initiated. The simplest criterion would be the
"handbook" ultimate tensile strength. However, note that the
early-time stresses at r<4cm in Figure 27 substantially exceed
the nominal strength for 7075-T6; nonetheless, the impact
conditions for 7L1.60 did not produce failure in UDRI tests.
This suggests that the strength of 7075-T6 under the complex,
dynamic loading conditions experienced near the entrance hole
in these tank impact problems is greater than the nominal
handbook values, which are based on data from quasi-static,
uniaxial stress laboratory tests.* We know of no way of directly
measuring these effective strengths for the actual loading con-
ditions being experienced, but calibration with parallel exper-
iments can provide semi-quantitative information.

Our approach for such calibration has been as follows:
From UDRI test data, we know large sphere (11.66 gm) impacts
onto 1/4-in. 7075-T6 produce failures for velocities of 1.69
km/sec and above, while no failures have occured for velocities
of 1.63 km/sec and below. NONSAP was used to analyze these
bounding cases (7L1.63 and 7L1.69), and the peak $\sigma_{\theta\theta}$ vs R pro-
files in Figure 28 were obtained. In order to predict whether
or not failure occurs in 7075-T6 for other thicknesses or impact
velocities, the calculated peak $\sigma_{\theta\theta}$ vs R profiles for those
conditions were compared with these calibration cases.

---

* See section 4.6 for additional comments regarding handbook
  strength values.

46

Overstress Area = $\int (\sigma_{\theta\theta} - \sigma_p) dR$
(hatched regions beneath $\sigma_{\theta\theta}$ profiles)
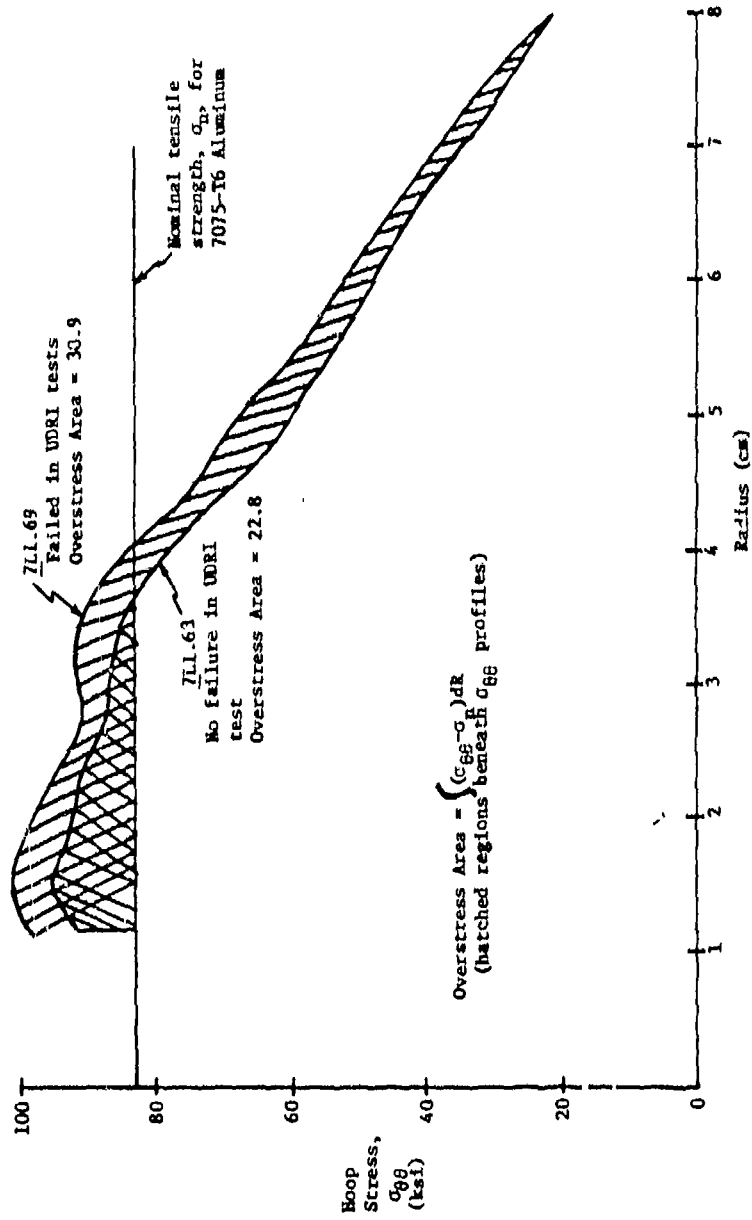
Figure 28. Calibration of "Overstress Area" Criterion for Failure Predictions of 7075-T6 Aluminum Front Panels.

4.3 Failure Predictions for Bare 7075-T6 Aluminum Panels

Table 3 shows the different cases that have been calculated, using NONSAP, for "bare" 7075-T6 panels (i.e. panels in direct contact with the fluid). The hoop stress vs radius profiles for these cases are contained in Appendix B. Table 3 includes a summary of the calculated overstress areas, $\int (\sigma_{\theta\theta} - \sigma_{11})\,dR$, together with the failure predictions.

The values of the overstresses are plotted versus velocity in Figure 29. The shaded region constitutes an uncertainty band for the predictions of the failure velocity, V_f. Experimentally determined values of V_f are also denoted for comparison.

4.4 Failure Predictions for Bare 2024-T3 Aluminum Panels

Table 4 shows the NONSAP cases for bare 2024-T3 panels, together with the calculated overstress areas and the failure predictions. (The $\sigma_{\theta\theta}$-R profiles are contained in Appendix C).

Exact bracketing of the failure/no failure impact velocity range was not available to us from UDRI test results for one projectile-panel thickness combination in 2024-T3. It was therefore necessary to use data from different combinations, specifically 2S1.60 (no failure in UDRI test) and 2L1.46 (failure in UDRI test).

Figure 30 shows the overstress areas vs velocity for the 2024-T3 panels, and illustrates the uncertainty band for failure prediction, as calibrated from results of tests 2S1.60 and 2L1.46. Again, the current experimental values are included.

4.5 Comparison of Failure Predictions with Experimental Data Available to CRT

The calculated and experimental predictions of failure velocities for the various combinations of plate thickness and alloy as discussed above are summarized in Table 5. The four predictions for .635 cm thick panels are in quite good agreement with the test results. (7L agrees of course, as this configuration was used to normalize the calculations.) 7S and 2L predictions are within the spread of the test data. The

48

TABLE 3. SUMMARY OF 7075-T6 CASES TREATED IN NONSAP ANALYSES

Panel Thickness	Projectile Mass	Impact Velocity	Case Designation	Calculated Overstress Area $\int(\sigma_{\theta\theta}-\sigma_n)dR$	Failure Prediction
1/4-in.	11.66-gm	1.60	7L1.60	16.4	NO FAIL
1/4-in.	11.66-gm	1.63	7L1.63*	22.8	NO FAIL
1/4-in.	11.66-gm	1.69	7L1.69*	30.9	FAIL
1/4-in.	11.66-gm	1.80	7L1.80	43.9	FAIL
1/4-in.	5.83-gm	1.80	7S1.80	11.5	NO FAIL
1/4-in.	5.83-gm	1.95	7S1.95	27.0	UNCERTAIN
1/4-in.	5.83-gm	2.00	7S2.00	34.5	FAIL
1/16-in.	11.66-gm	1.15	7L1.15	10.8	NO FAIL
1/16-in.	11.66-gm	1.30	7L1.30	20.8	NO FAIL
1/16-in.	11.66-gm	1.45	7L1.45	35.7	FAIL
1/16-in.	5.83-gm	1.30	7S1.30	12.1	NO FAIL
1/16-in.	5.83-gm	1.40	7S1.40	19.1	NO FAIL
1/16-in.	5.83-gm	1.56	7S1.56	29.3	UNCERTAIN

* Cases 7L1.63 and 7L1.69 correspond to UDRI tests which
bracketed uncertainty band for critical velocity. Calculated
overstress areas, $\int(\sigma_{\theta\theta}-\sigma_n)dR$, for these conditions were
used to calibrate failure prediction criterion for 7075-T6:

If $\int(\sigma_{\theta\theta}-\sigma_n)dR >30.9$, panel fails

If $\int(\sigma_{\theta\theta}-\sigma_n)dR <22.8$, no failure

Figure 29. Overstress Area vs Impact Velocity for 7075-T6 Al Front Panels

Impact Velocity (km/sec)

Overstress Area

$V_f(7S)=.99\pm.06$ $\longleftarrow$ Experimentally $\longrightarrow$ $V_s(7L)=1.66\pm.03$ $V_s(7S)>1.95$

Determined V_s

$V_f(7L)<1.0$

Failure

UNCERTAIN

No Failure

7L

7S

7L

7S

100

50

10

1.2   1.4   1.6   1.8   2.0

TABLE 4. SUMMARY OF 2024-T3 CASES TREATED IN NONSAP ANALYSES

Panel Thickness	Projectile Mass	Impact Velocity	Case Designation	Calculated Overstress Area, $\int(\sigma_{\theta\theta}-\sigma_n)dR$	Failure Prediction
1/4-in.	11.66-gm	1.80	2L1.80	38.4	FAIL
1/4-in.	11.66-gm	1.90	2L1.90	52.6	FAIL
1/4-in.	11.66-gm	2.10	2L2.10	70.9	FAIL
1/4-in.	5.83-gm	1.94	2S1.94	21.1	UNCERTAIN
1/4-in.	5.83-gm	2.00	2S2.00	25.3	FAIL
1/4-in.	5.83-gm	2.20	2S2.20	50.3	FAIL
1/16-in.	11.66-gm	1.40	2L1.40	14.6	NO FAIL
1/16-in.	11.66-gm	1.52	2L1.52	37.9	FAIL
1/16-in.	5.83-gm	1.60	2S1.60*	20.9	NO FAIL
1/16-in.	5.83-gm	1.94	2S1.94	56.2	FAIL

* UDRI test 2S1.60 produced failure. This result was used to
calibrate lower bound of failure criterion for 2024-T3. UDRI
test 2L1.46 produced no failure. This result was used to
calibrate upper bound. Thus:

If $\int(\sigma_{\theta\theta}-\sigma_n)dR > 23$, panel fails

If $\int(\sigma_{\theta\theta}-\sigma_n)dr < 21$, no failure

51

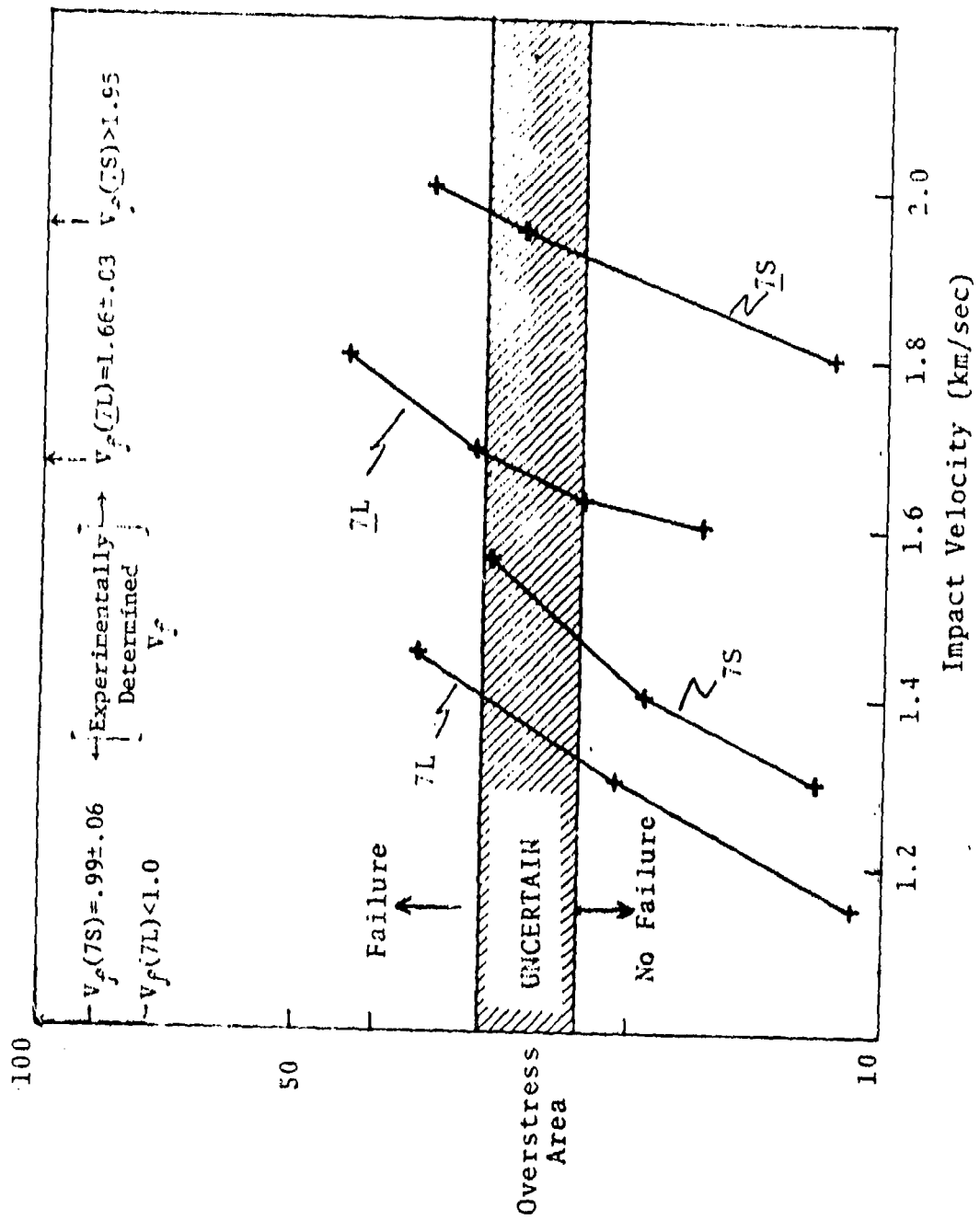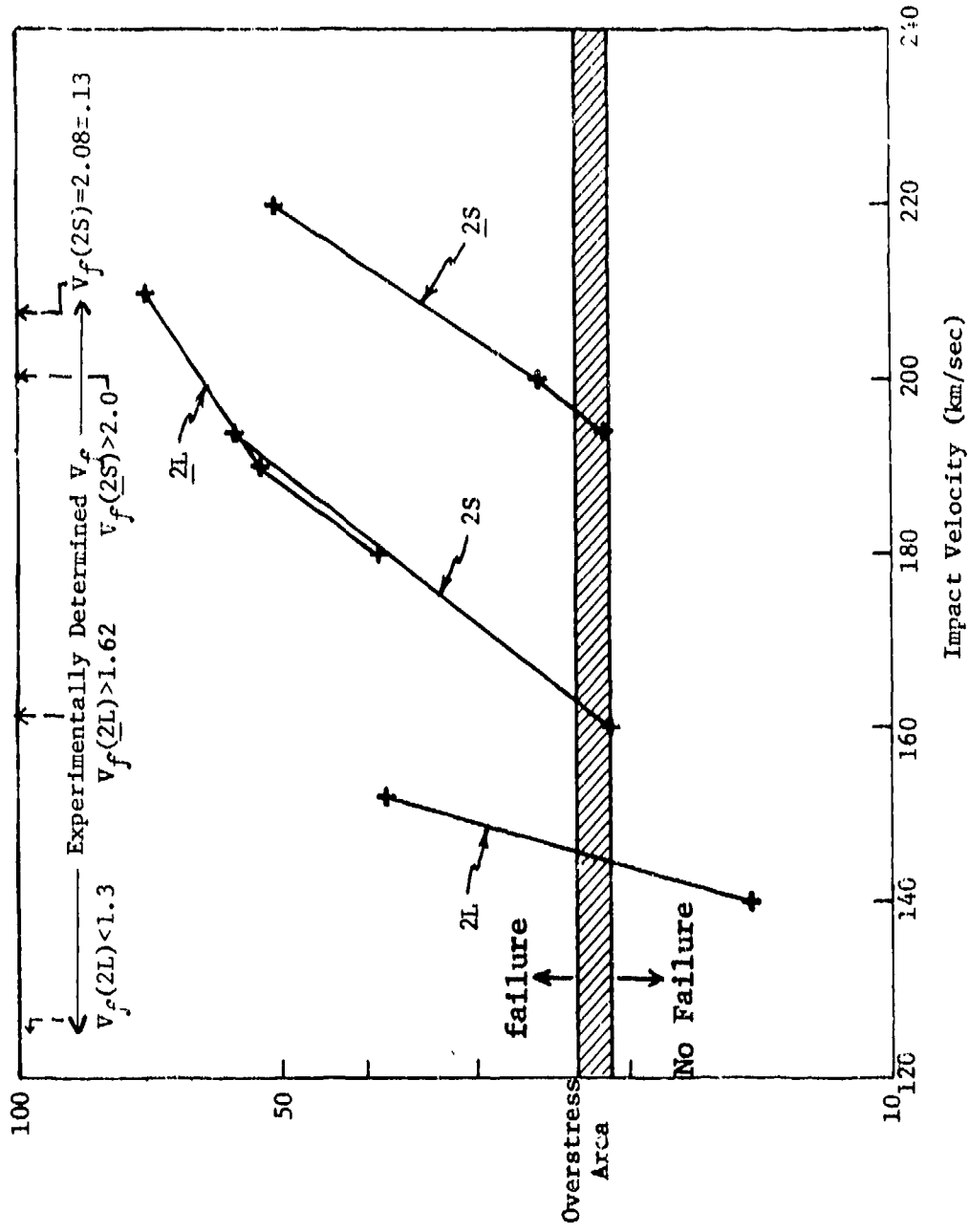Figure 30. Overstress Area vs Impact Velocity for 2024-T3 Aluminum Front Panels.

52

TABLE 5. PREDICTED FAILURE VELOCITIES

Condition Designation	Panel Alloy	Thickness (in.)	Projectile Mass (gm)	Predicted Critical Failure Velocity, V_f (km/sec)	Experimentally Determined V_f (km/sec)	Relevant UDRI
7L	7075-T6	1/4	11.66	1.63~1.69	1.66±.03	7L1.63* and 7L1.69*
7S	7075-T6	1/4	5.84	1.92~1.97	>1.95	7S1.95
7L	7075-T6	1/16	11.66	1.33~1.41	< .99	---
7S	7075-T6	1/16	5.84	1.48~1.59	.99±.06	7S1.35
2L	2024-T3	1/4	11.94	1.60~1.64	>1.62	2L1.60
2S	2024-T3	1/4	5.6	1.94~1.97	>2.0	---
2L	2024-T3	1/16	11.94	1.44~1.46	<1.30	2L1.30
2S	2024-T3	1/16	5.6	1.60~1.64	2.08±.13	2S1.60* and 2S1.94

* Calibration cases

53

$\underline{2S}$ results are slightly below (~2%) the experimental value. This V_f, however, was extrapolated from the other test data since no shots of the large cube into the .635 cm panel have been fired.

The calculated V_f's for the thinner, .158 cm panels differ significantly from the experimental results. The most plausible explanation for the discrepancy would be an error in the dependency of the loading functions on panel thickness, ω. The final loading finctions (Equations 3 and 4) derived subsequent to the structural analysis of failure have a very different dependence on ω than Equations 1 and 2. Thus, calculations using the final functions to obtain the loading forces may produce results in better agreement with the data. The large difference between the V_f obtained experimentally in the 2L and 2S test series indicates that for the thin panels, the effect of penetrator shape is significant, i.e., the cubes in the 2L tests produced a substantially lower V_f than the spheres in the 2S series.

The above comparisons suggest that the numerical techniques are not yet able to predict from panel failures without the aid of experiments. The various approximations imposed by the numerical constraints (e.g., axial symmetry, material models) and cost considerations necessitate the type of normalization to test data discussed above. Results of extrapolations away from the known data base are less certain and may be in error. Thus, currently, the calculations are best used to provide a detailed understanding of the phenomena associated with front panel failure by fragment impact, rather than as predictive tools. Further development and refinements of the techniques, coupled with a broadening experimental data base are needed before the codes can reliably predict failure for a set of conditions which vary widely from the known data.

4.6 Variations in Mechanical Properties of Aluminum Alloys and Their Effects on Failure Conditions

It is of some interest to assess the possible effects of mechanical property variations on the failure conditions (as determined experimentally or analytically) for fragment impacts into fuel tank panels. From Ref. 4, the range of properties for 2024-T3 and 7075-T6 alloys are as follows:

Alloy	Ultimate Strength (ksi)			Yield Strength (ksi)		
	*min	nominal	max**	min*	nominal	max**
2024-T3***	63	70	77	42	50	58
7075-T6***	78	83	88	69	73	77

*Minimum values are levels at which 99% of the material is expected to conform, at confidence level of 0.95. These values are generally specified for all *design* purposes.

**Assuming symmetrical distribution around the nominal value.

***The mechanical property limits of material designated as T3 recognize effects of cold working (e.g., flattening) on strength. Such effects, if present, are *not* recognized in the property limits of material designated as T6. By implication, the properties of 7075-T6 may be understated.

From these values and the distribution data, it can be presumed that 90% of the aluminum panels will have properties in the following ranges:

Alloy	Ultimate Strength (ksi)	Yield Strength (ksi)
2024-T3	65.5-74.5	44.9-55.1
7075-T6	79.8-86.2	70.5-75.5

NONSAP analyses were repeated for Case 7L1.69 to determine the sensitivity of critical failure velocities to these variations

in mechanical properties. The results show the following:

Properties Assumed for 7075-T6	Calculated Overstress Area $\int(\sigma_{\theta\theta} - \sigma_n)dR$
$\sigma_y = 70.5$ ksi $\sigma_u = 79.8$	35.4
$\sigma_y = 73$ $\sigma_u = 83$	30.9
$\sigma_y = 75.5$ $\sigma_u = 86.2$	27.7

These variations in overstress area are equivalent to a variation in critical velocity of ±30 m/sec about the nominal value; if the threshold failure velocity were determined to be V_c for a sample of material, there is a 90% probability that the value for another lot would be in the range V_c ±30 m/sec.

SECTION V.

CALCULATIONS OF ENTRANCE PANEL DISPLACEMENTS

The NONSAP calculations discussed in Section 4 were all terminated 120 μsec after impact, by which time the tensile stresses within ~5cm of the impact point have passed their peak. Thus, if failure occurs, it does so very shortly after impact. Displacements along the panel, however, do not peak for several milliseconds, time enough for several transits of the waves in the tank. To examine these late-time displacements, NONSAP calculation of 7L1.63 was extended in time and compared with the test results (Figure 31). The calculated peaks are about a factor of three lower than the experimental values. Two related explanations for this result are: 1) the breakdown of the analytic functions for points beyond 8 cm from the point of impact, and 2) the failure to model the dynamic pressure of the water behind the panel. To account for the first effect, the loading on the panel beyond 8 cm was arbitrarily modified in a second run, so that the peak pressure and total specific impulse were equal to the values at 8 cm. Arrival times and pulse shape, however, were unchanged so as to be consistent with the distance from impact. Using these conditions, the on-axis peak displacements doubled, and the overall difference between the calculation and the test data was cut in half. In a third calculation, the inertial effect of the water was approximated by not allowing the loading pressure to drop below 5 bars. This value was chosen because the water-Al interface near the point of impact in the CRALE calculations was moving about 3000 cm/sec which gives a dynamic pressure, $\frac{1}{2}\rho V^2 \approx$ 4.5 bars. The results are shown in Figure 32; displacements at .6, .8, and 1.2 μsec, were comparable with the test results at similar times. The peak displacements are also in good agreement (Figure 33).

The correlation between the final calculation and the experimental peak displacements is coincidental, since both the modeling of the pulse beyond 8 cm and the imposition of a
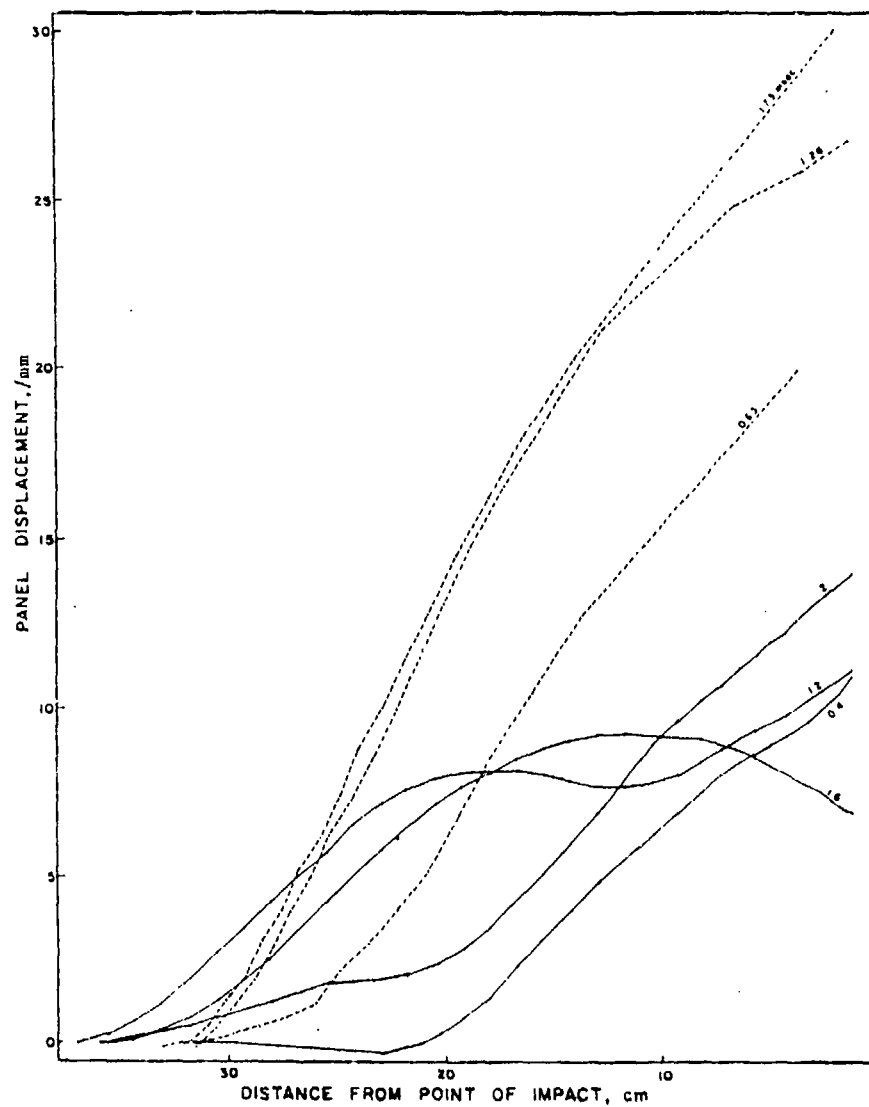
57

Figure 31. Comparison of measured (dashed lines) and predicted (solid lines) displacement for FD8 (configuration 7L). (The measured profiles are referred to the original surface, translated outward to maintain zero displacement at the bolt centerline).
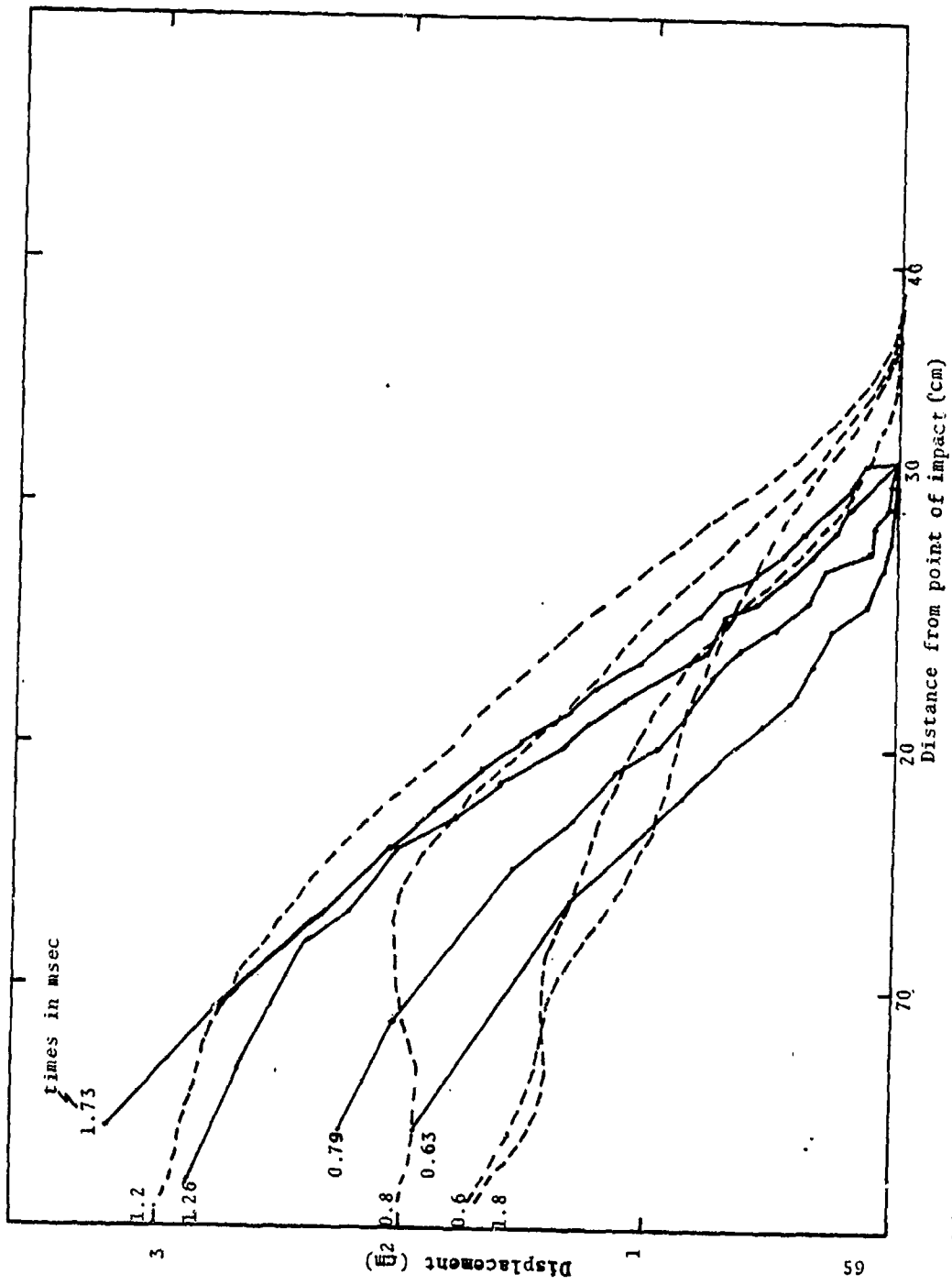
58

Figure 32. Displacements along a ¼" 7075-T6 Al front panel struck by an 11.66 gm steel fragment at 1.63 km/sec shot FD8. Experimental data (solid lines) are from shot FD8. Finite element calculation (dashed lines) include effect of dynamic pressure and forces beyond 8 cm from impact point.
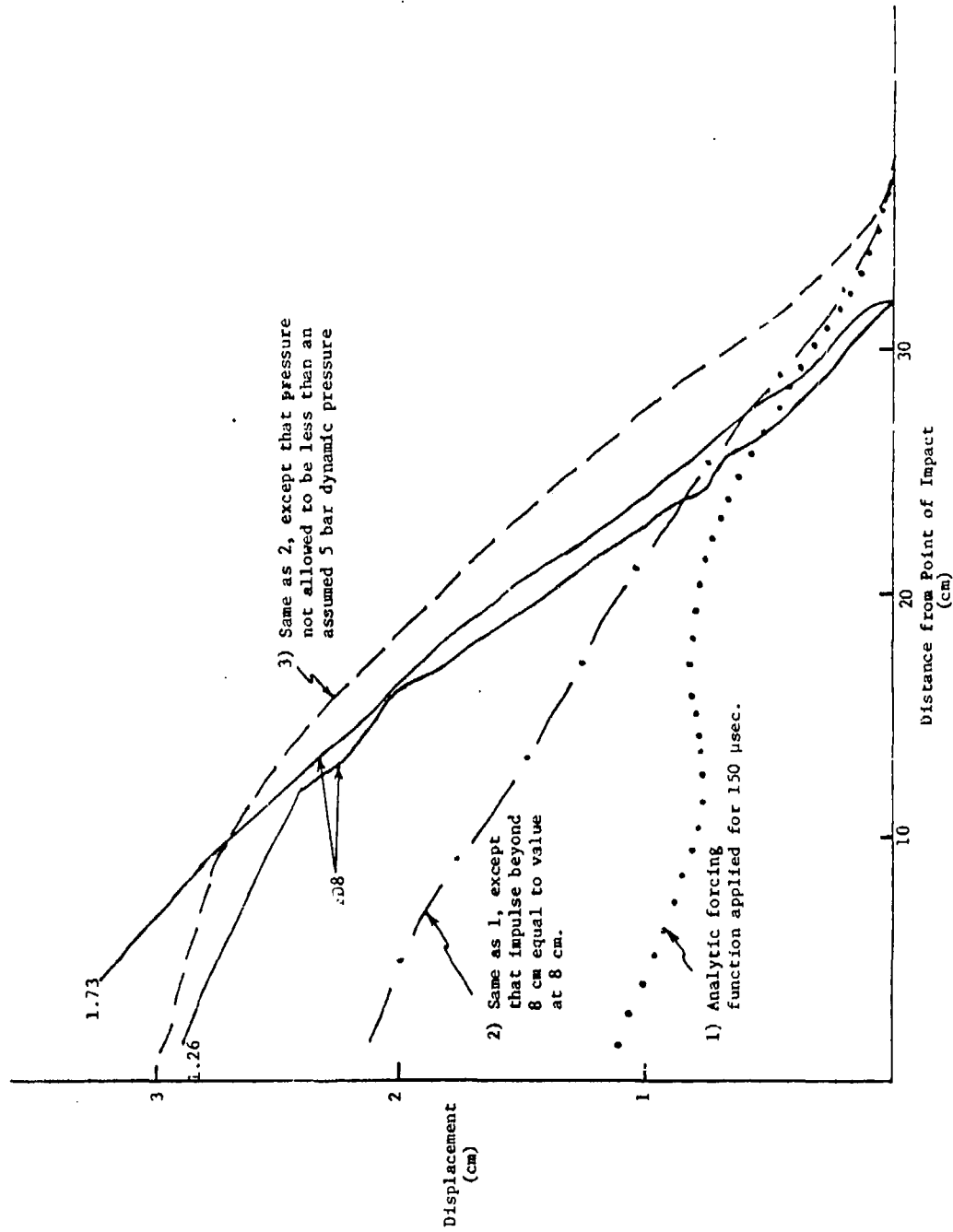
59

Figure 33. Comparisons of Peak Displacements from Three Finite Element Calculation of $\underline{7L}1.63$ with the Experiment (FD8).
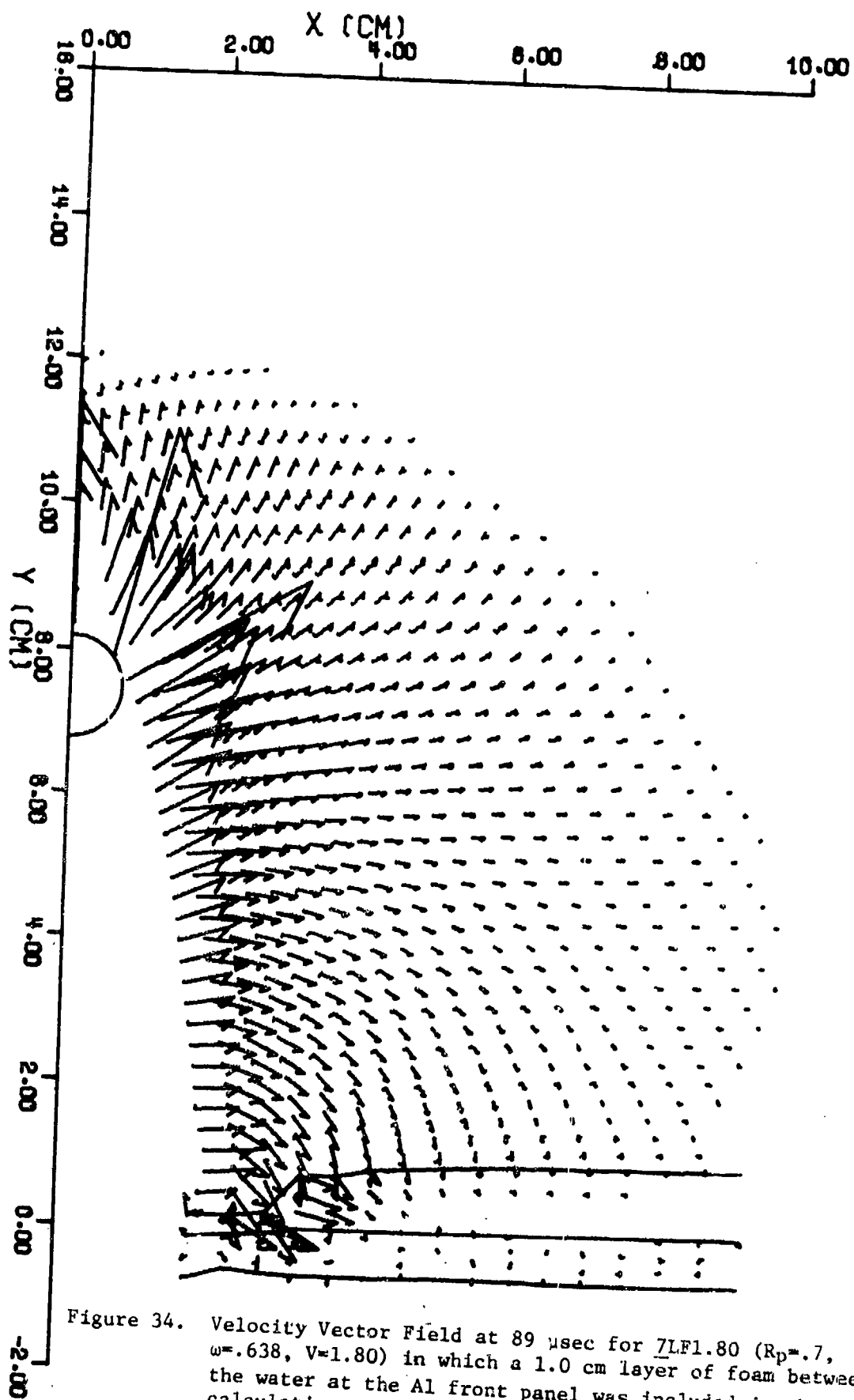
constant 5 bar dynamic load were relatively crude approxima-
tions of the actual phenomena. However, the effect of both
changes on displacement was significant. Neither can be
ignored in calculations of the motions beyond several
hundred microseconds. If peak displacements are of interest,
the finite difference portion of the calculations must be
carried out to several milliseconds to fully define the front
panel loading.

SECTION VI.

CALCULATION OF FRONT PANELS BACKED BY 1.0 CM OF FOAM

The inclusion of a thin (1.0 cm) layer of foam between the entrance panel and the fuel produces a dramatic improvement in the resistance of the tank to failure, with a resulting large increase in the fragment velocity needed to produce catastrophic failure. In the accompanying experimental program, the only failures of panels backed by only 1 cm of foam were obtained by firing the larger, 11.6 gm cube into tanks with the thin, .158 cm, 7075-T6 Aluminum front panels at velocities greater than 1.6 km/sec. (A velocity of 1.2 km/sec failed a plain panel of the same thickness.) The failures in the foam-backed panels, in contrast to the straight cracks which run from the entry hole to the edges in plain panels, resulted in long spiral-like fractures encompassing much of the panel. This fracture pattern, coupled with the experimental data showing that foam did not significantly reduce the *peak displacements* of the panels, clearly indicate that, a different fracture mode was exercised.

Several calculations were undertaken to examine the effects of the foam on the front panel behavior. The first pair of runs included both the foam and the panel explicity. The water crushed the foam, which could compact a factor of 10 before generating any significant (i.e., > 25 psi) resistance and the problems quickly ran into difficulties with zone size and time-step. As shown in Figure 34 for 7LF1.80, the water close to the entry hole has almost completely crushed the intervening foam. Based on the velocity vectors, the water appears to be stripping the foam from off the front panel. The post-shot panels in corresponding tests show that the foam is, indeed, removed from an area at least several centimeters in radius around the hole. As the code is not currently able to remove zones of material from between two

Figure 34. Velocity Vector Field at 89 μsec for 7LF1.80 (R_p=.7, ω=.638, V=1.80) in which a 1.0 cm layer of foam between the water at the Al front panel was included in the calculation.

63

dissimilar materials, the problems could not be run further and a second technique was required to generate a solution.

As it appeared that the foam offered little resistance to the water, another calculation was run in which neither foam or the Aluminum panel were included. Thus, the front of the water jumped off as if it were a free surface. As each zone of the water moved off 1 cm, however, the inertial mass of the Aluminum it would have encountered was added to its mass. This immediately slows down the water and sends a pressure pulse back into the tank.

The resultant pressure time histories to 230 μsec from points originally .1 cm behind the front surface of the water, between 2 and 9 cm from the point of impact are shown in Figure 35. A distinct separation of the first signal and the much larger pulse due to the water hitting the front panel is apparent in the traces for ranges between 2 and 6 cm. The initial impulse moves along the panel with a velocity of about 1.5 km/sec, consistent with the sound speed of water. The peak pressure in this signal is a factor of 5 lower than that calculated for the corresponding bare panel case, $7L1.80$, but decays with range to the -1.75 power, consistent with Equations 3 and 4 of the analytic model. The major pulse, dependent on the material velocity of the water, has a phase velocity along the plate of only .25 km/sec. As shown in Figure 36, the peak pressure generated by the water-panel interaction is only a factor of two lower than $7L1.80$ at $R/R_p = 1$ and decays much less rapidly ($a = -.72$). Thus, the peaks beyond $R/R_p \approx 4$ in the foam-backed case are actually higher than for the bare panel. The lower peak close to the hole coupled with the delayed arrival of the peak signal allow the front panel to dissipate the forces substantially and considerably higher impact velocities are needed to initiate crack failure.
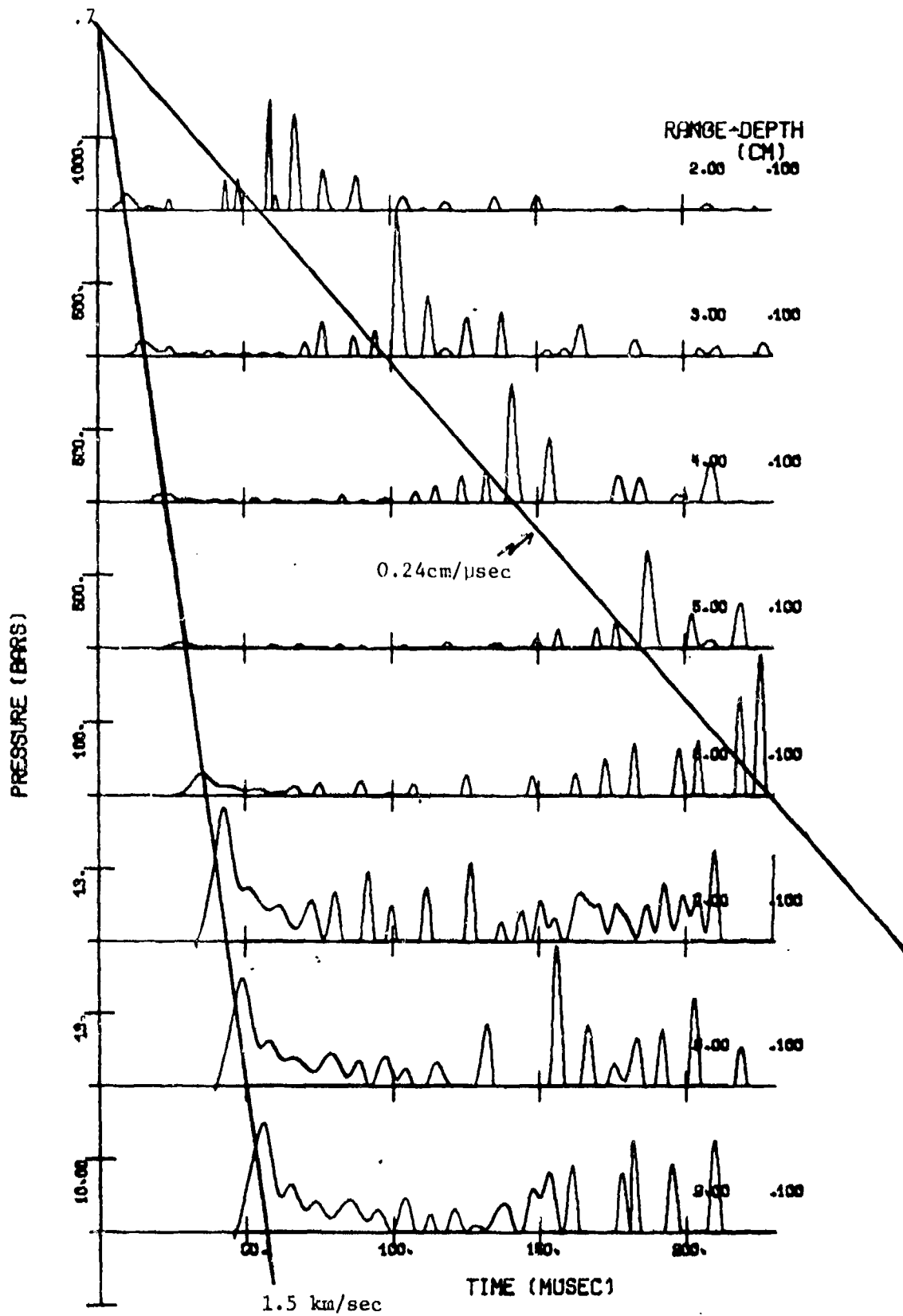
Figure 35. Pressure time histories for points 2 to 9 cm from the impact, .1 cm into the water for 7LF1.80 ($R_p=.7$, $\omega=.635$, V=1.80).
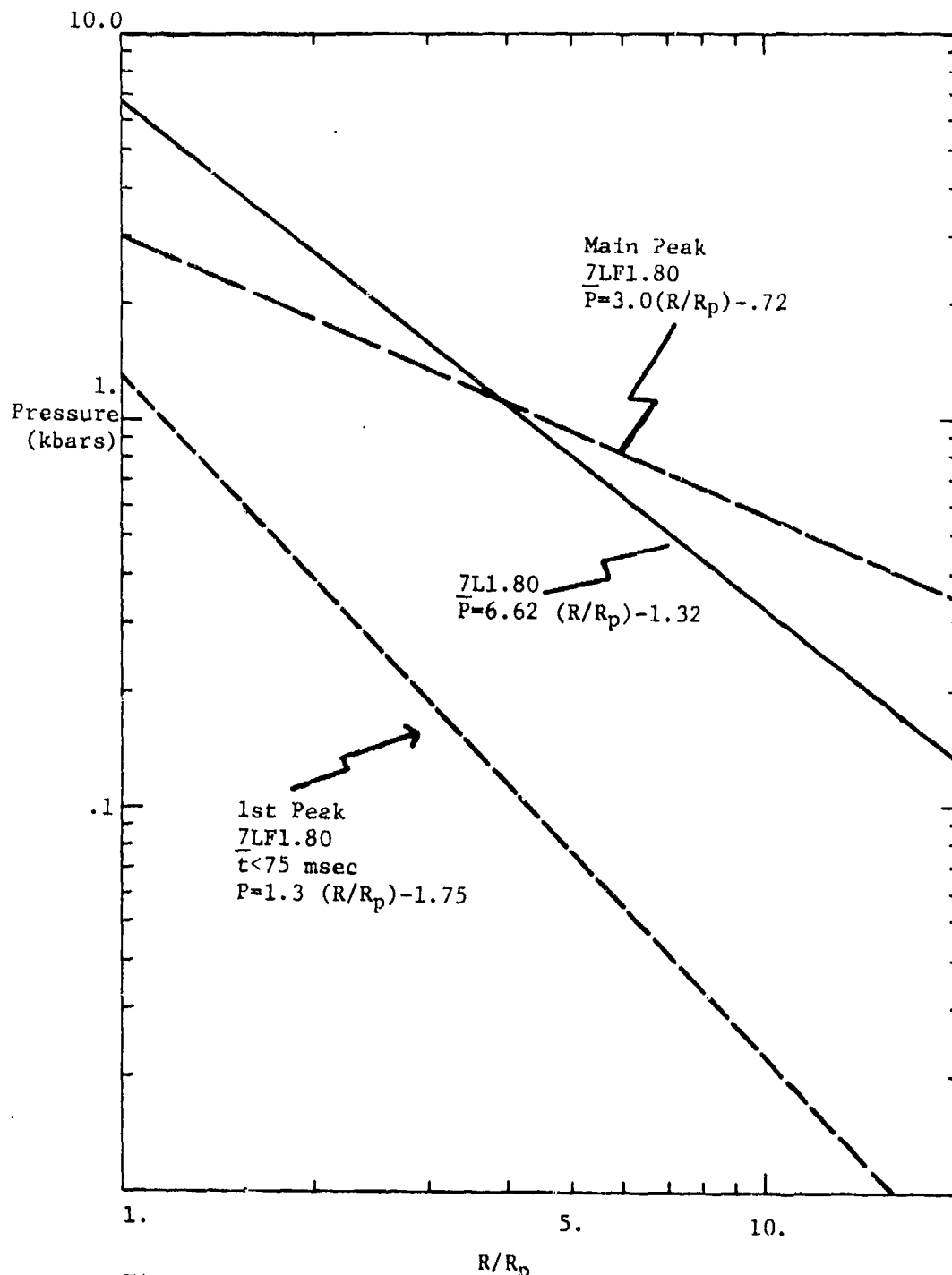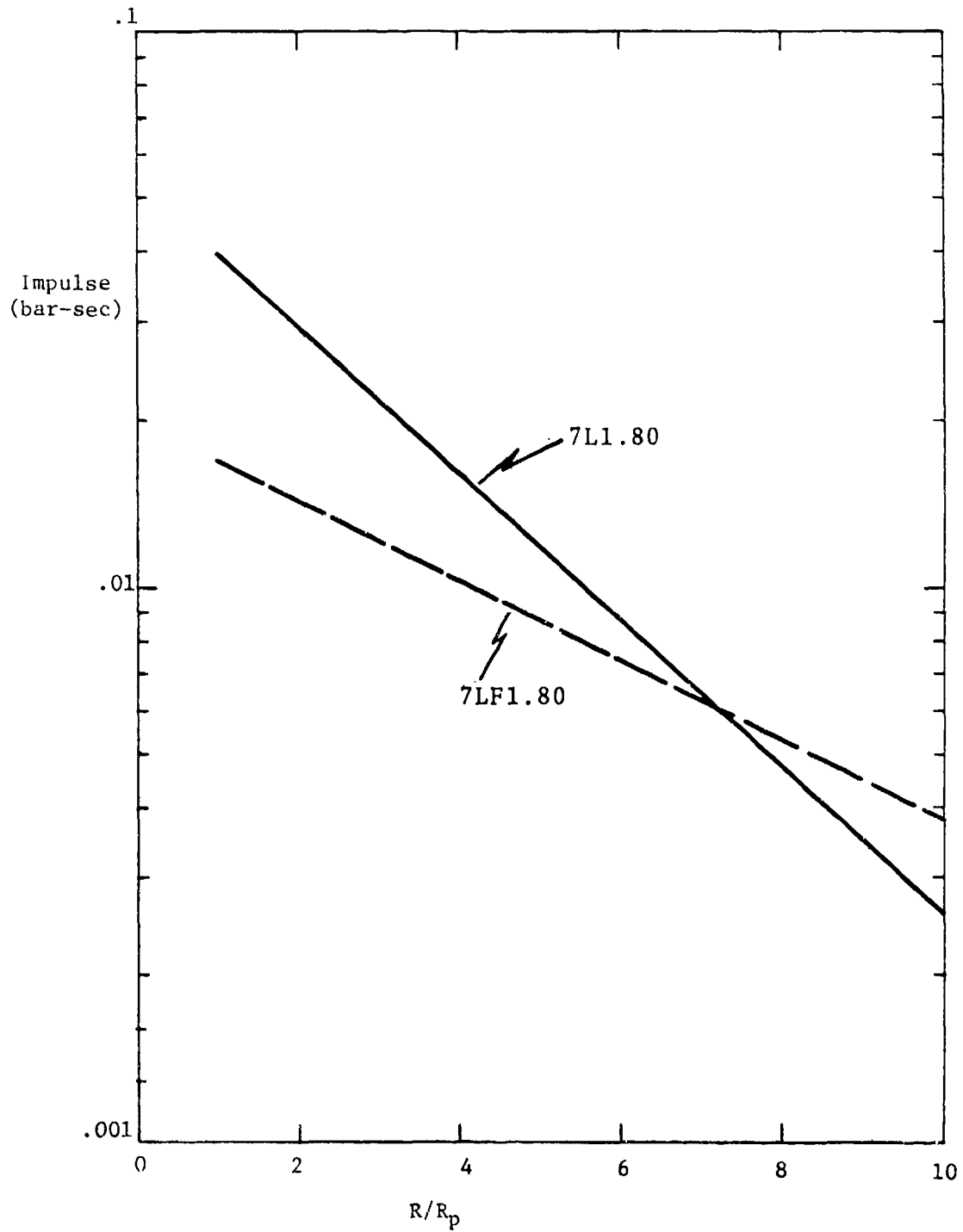
65

Figure 36. Peak Pressure Vs Range, for 7LF1.80 and 7L1.80 to illustrate the effect of including a 1.0 cm thick foam layer behind the .635 cm thick Al front panel.

66

The total impulse at $R/R_p \approx 1$ in $\underline{7}$L1.80, Figure 37, is also down considerably (~.017 bar-sec) compared to $\underline{7}$L1.80 (~.04 bar-sec). Again, however, the rate of decay with range is less, so that the total impulse beyond $R/R_p \approx 7$ is higher in the foam-backed case. Since total momentum must be conserved, the impulse delivered to the water is eventually communicated to the front plate in both cases, and results in total displacements of similar size.

The calculation of $\underline{7}$LF1.80 resolved the discrepancy between peak displacement and failure relative to the plain panels. Since the corresponding UDRI test program was unable to fail any but the .158 cm panels with the large cubes, no further calculation of foam-backed panels was undertaken.

Figure 37. Impulse vs Range for 7LF1.80 and 7L1.80 to illustrate the effect of including 1.0 cm layer of foam behind the .635 cm thick Al front panel.

68

APPENDIX A

COMPARISONS OF CALCULATED WAVE FORMS AND THE ANALYTIC MODELS
AT VARIOUS LOCATIONS BEHIND THE FRONT PANEL

Notes concerning the computer plots of Appendix A

1) Each pressure plot is scaled to the maximum value
calculated at that range. The pressure at the tic ,
mark ½" above the zero pressure line is printed for
each plot.

2) The plots are in general equally spaced in distance
from the impact point so that the velocities of the
various waves can be measured (as illustrated in
Figure A-1) by the use of a straight edge and ruler.

3) The plots at the right of each pressure trace are
labeled relative impulse. The analytic impulse
(ordinate) is plotted against the calculated value
at each time. Thus, deviation from a 45° line
indicate how well the fit approximates the calculated
waveform. Where the curve is above the 45° line
(drawn for convenience) the analytic impulse is
higher than calculated and vice versa.

4) The data for points .1 cm behind the plate at ranges
between 2 and 9 cm are plotted for each calculation,
followed by a second page which contains either a sim-
ilar plot for the .6 cm depth or one showing points
at ranges of 5, 7.5 and 10 cm and depths of .1 and .6
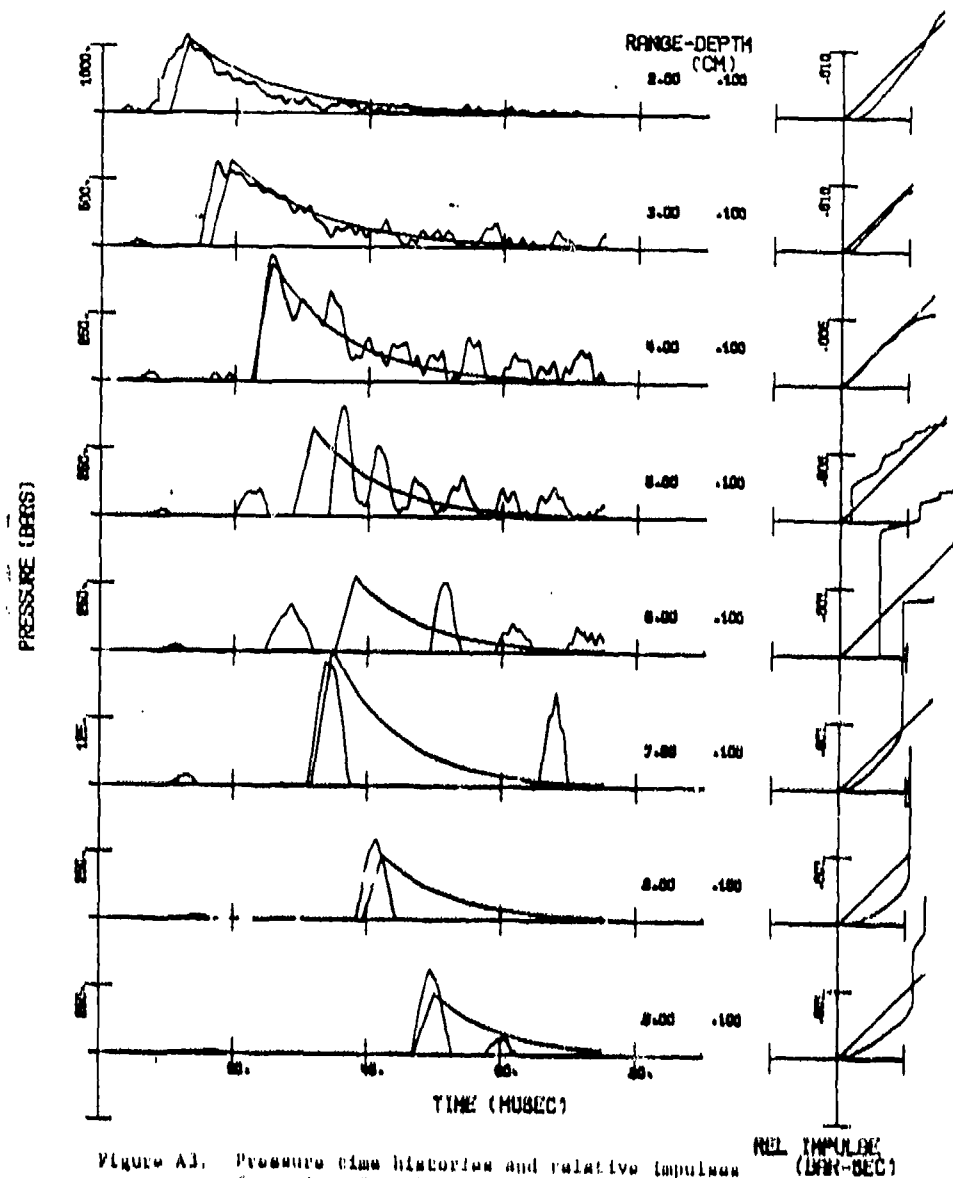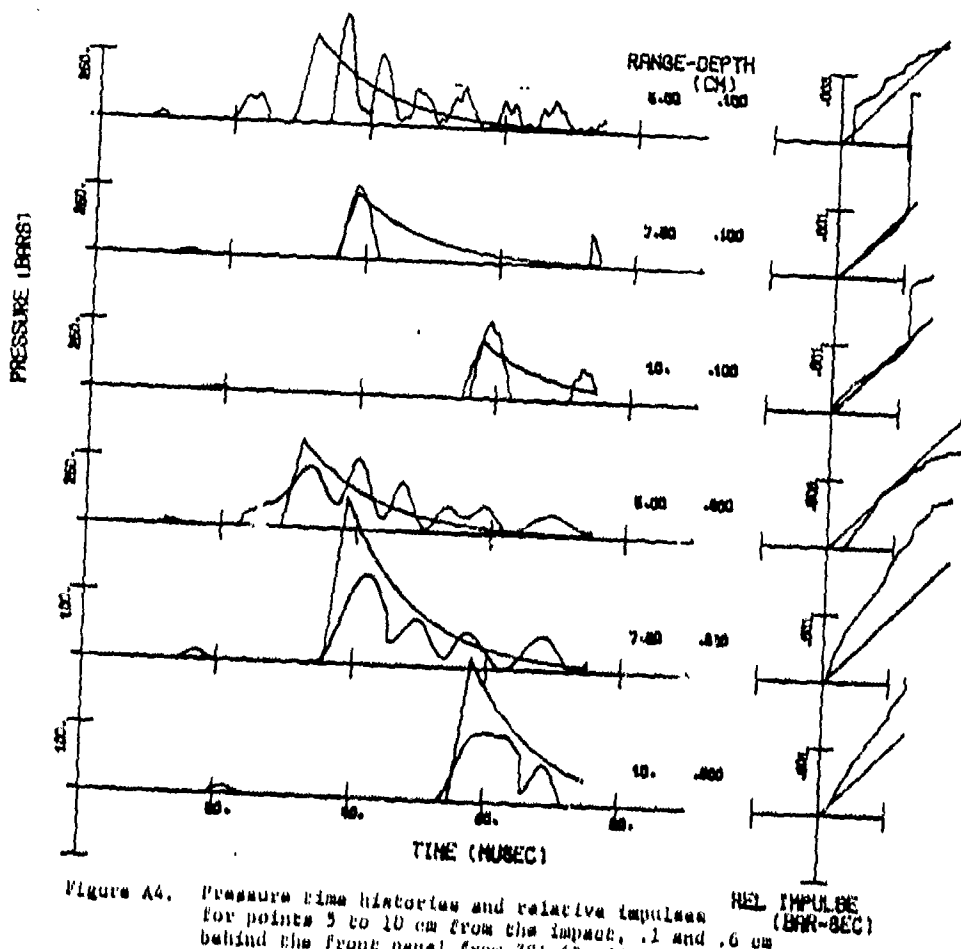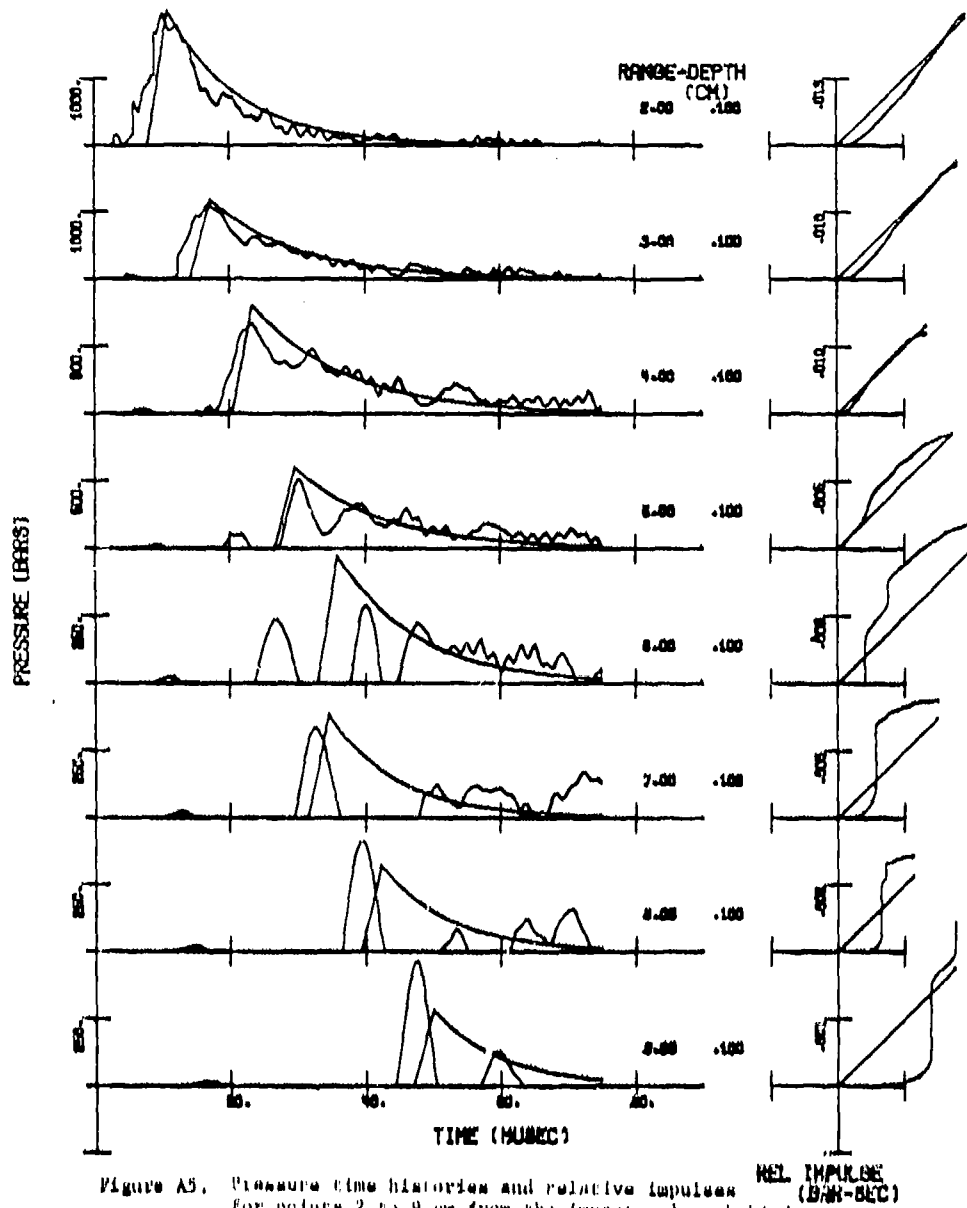depending on which data were obtained in the specific
calculations.

69
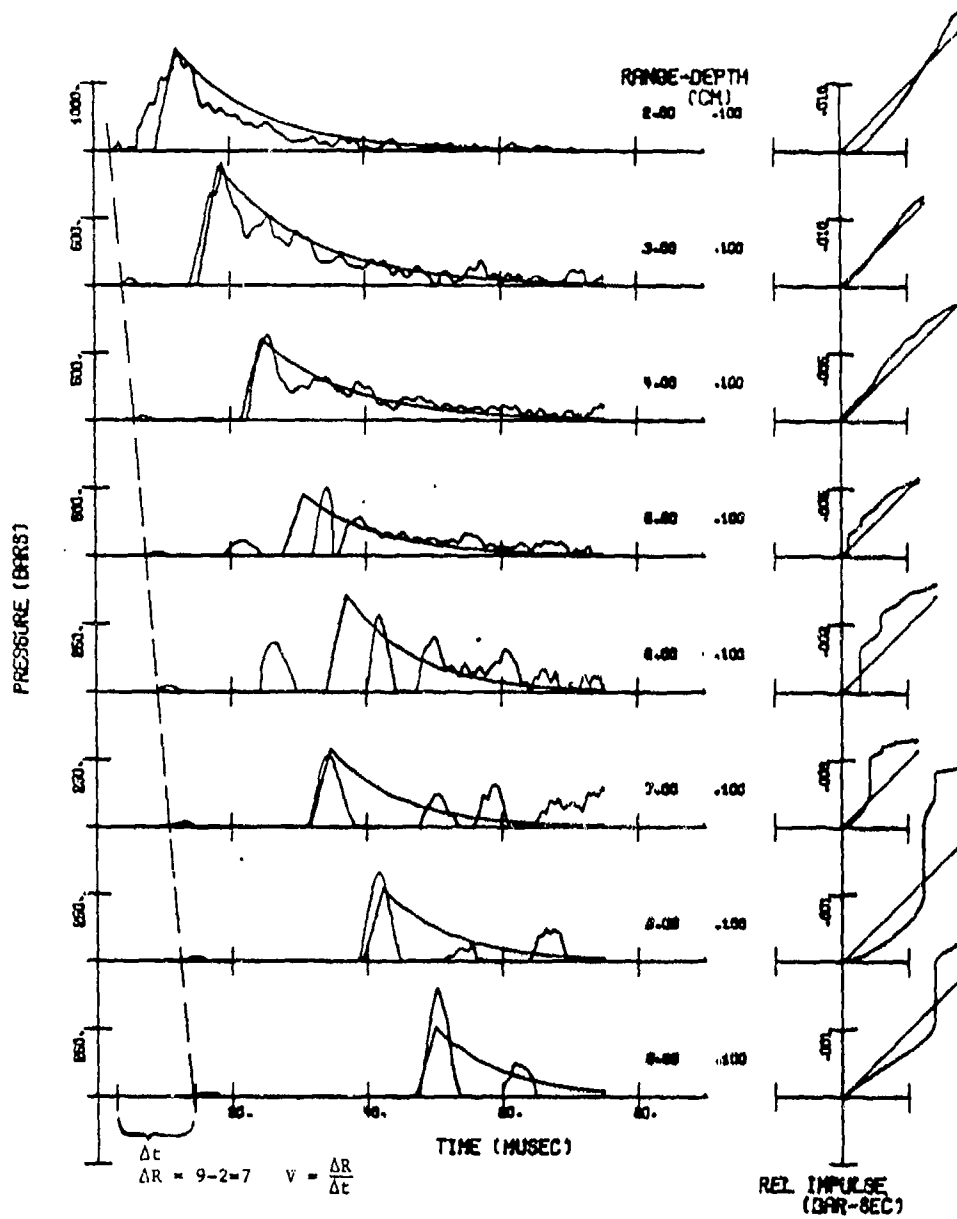
Figure A1. Pressure time histories and relative impulses for points 2 to 9 cm from the impact, .1 cm behind the front panel from 7L1.63. (R_p = .7, w = .635, V = 1.63)
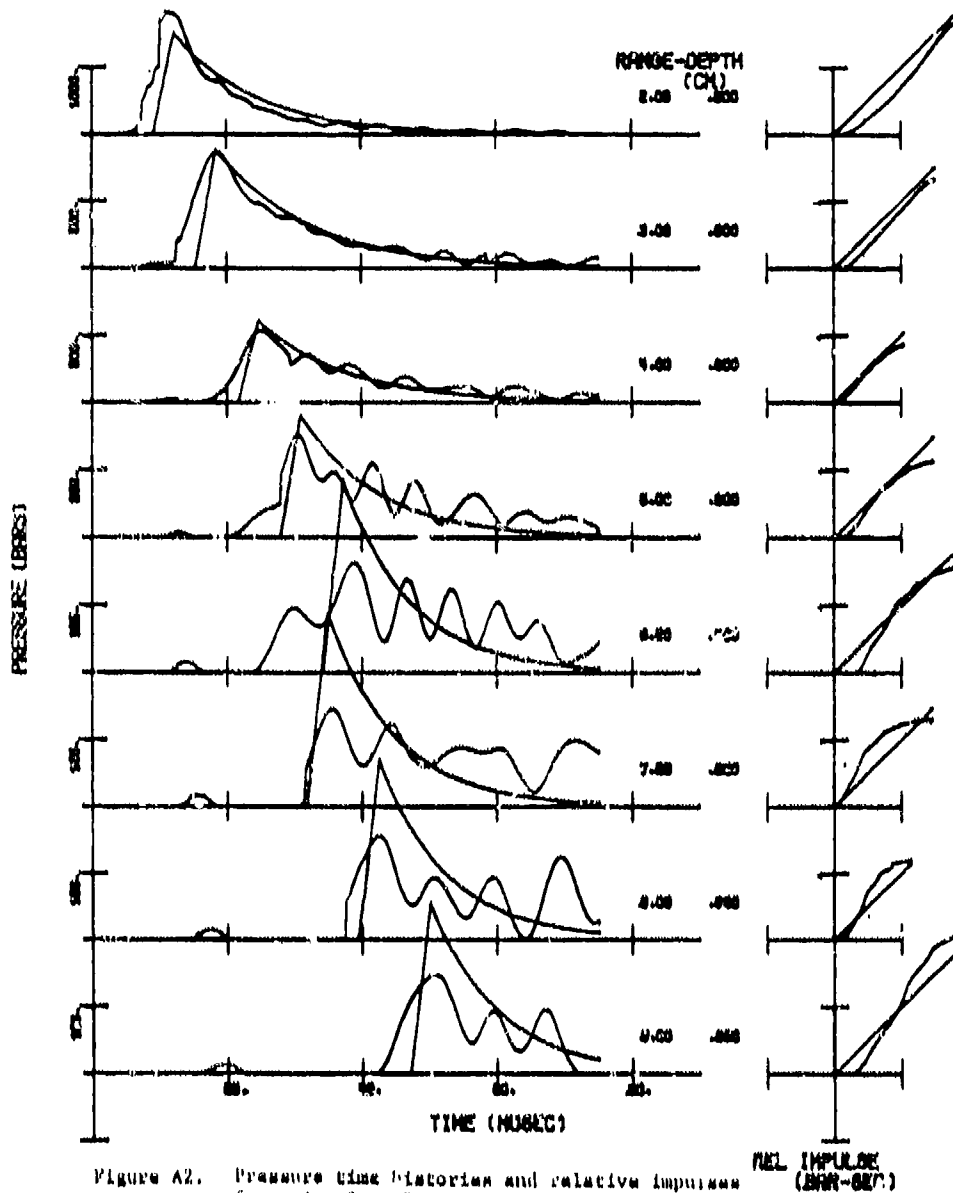
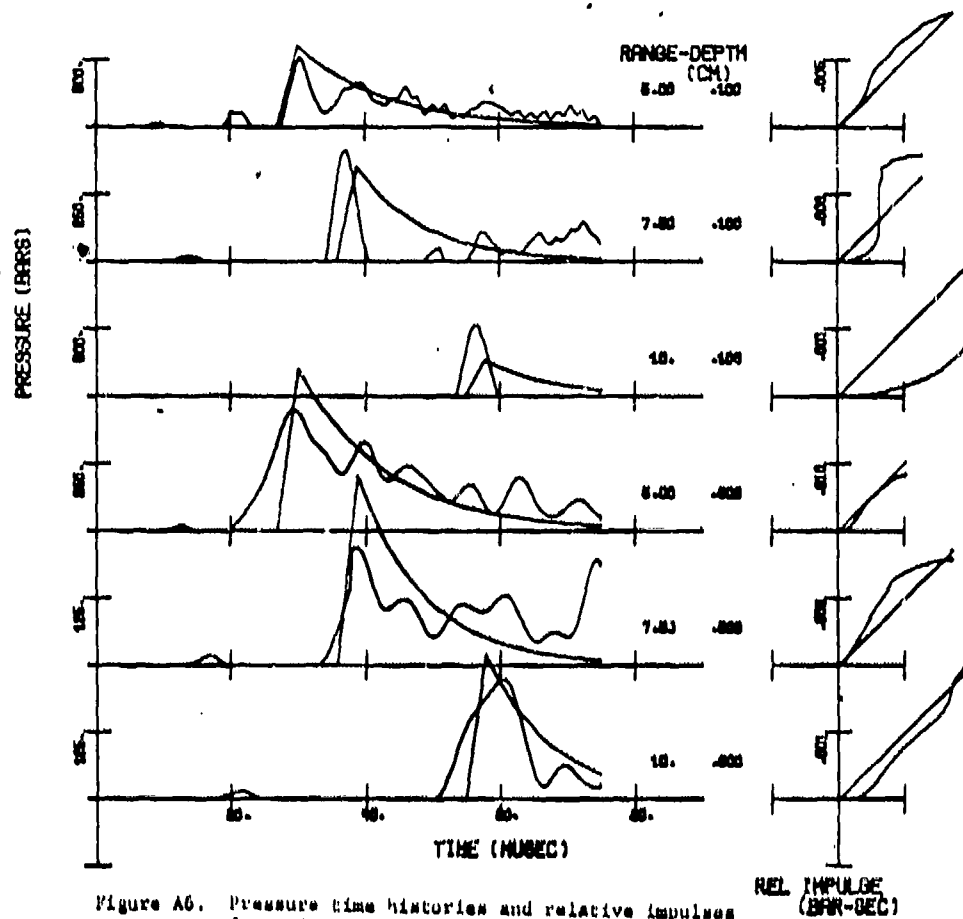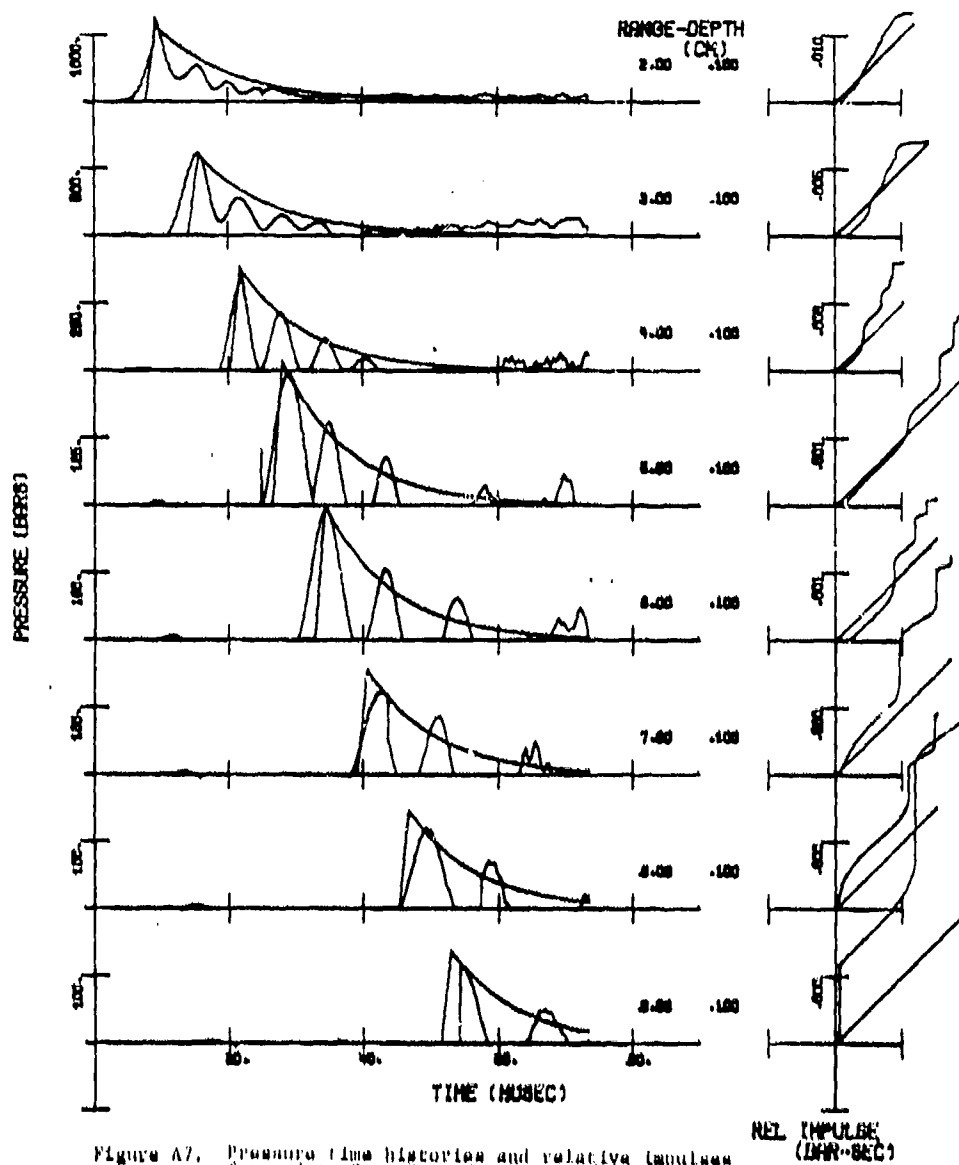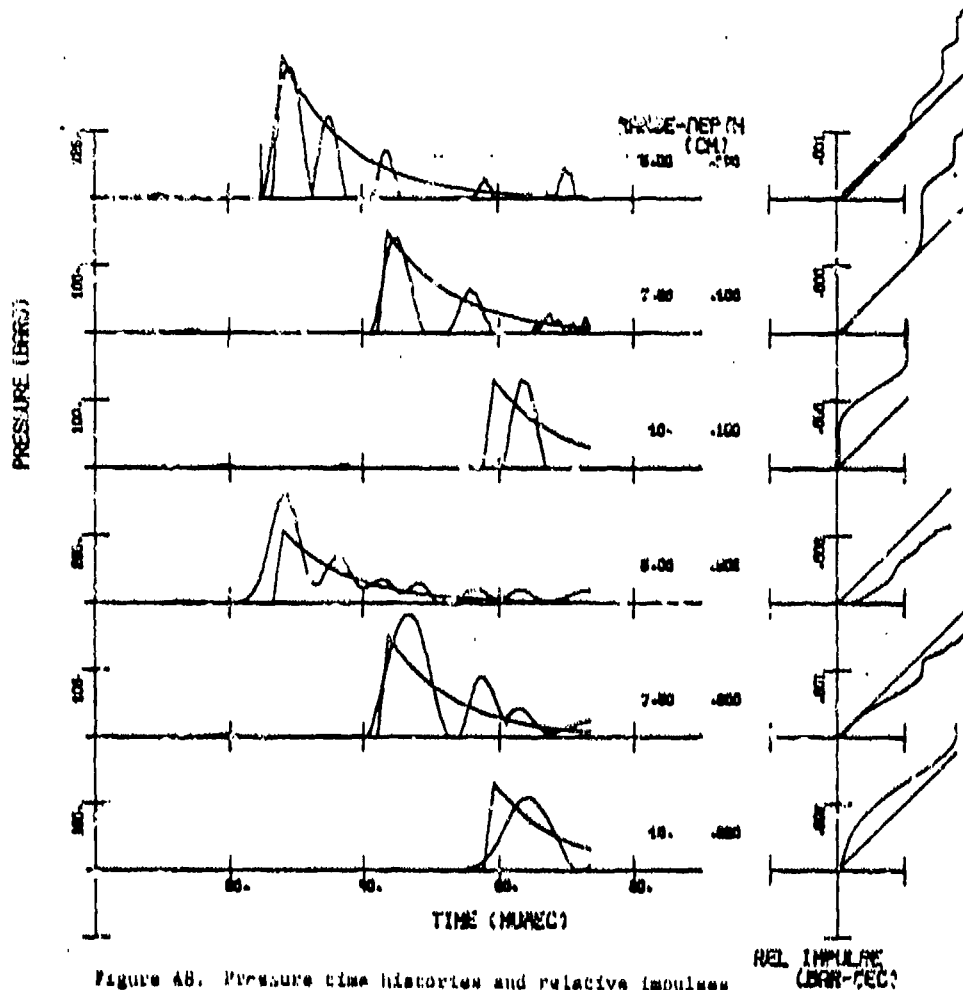Figure A2. Pressure time histories and relative impulses for point 2 to 9 cm from the impact, .6 cm behind the front panel from 7L1.63, (R_D = .7, ω = .635, V = 1.63).
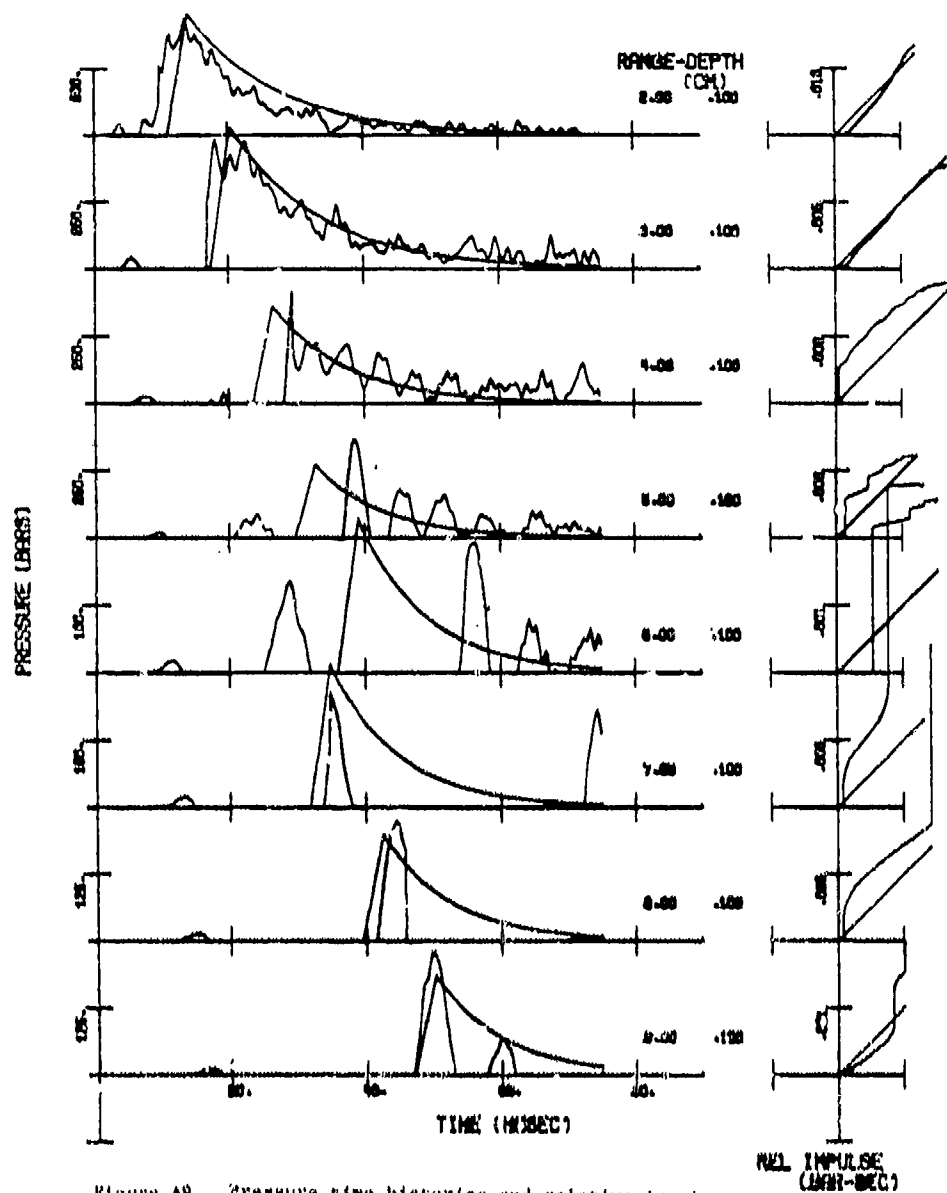
71

Figure A3. Pressure time histories and relative impulses for points 2 to 9 cm from the impact, .1 cm behind the front panel from 281.63, (R_p = .55, ω = .635, V = 1.63).
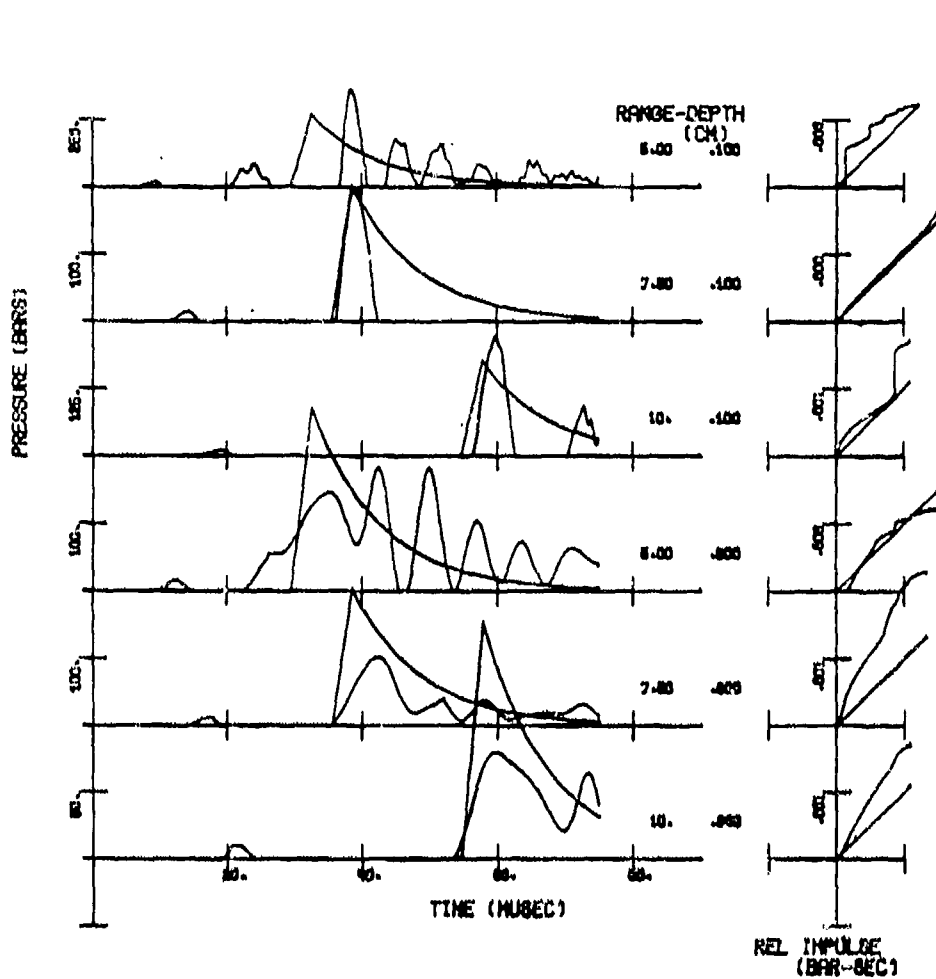
Figure A4. Pressure time histories and relative impulses for points 5 to 10 cm from the impact, .1 and .6 cm behind the front panel from 281.63, (R_p = .55, σ = .635, V = 1.63).
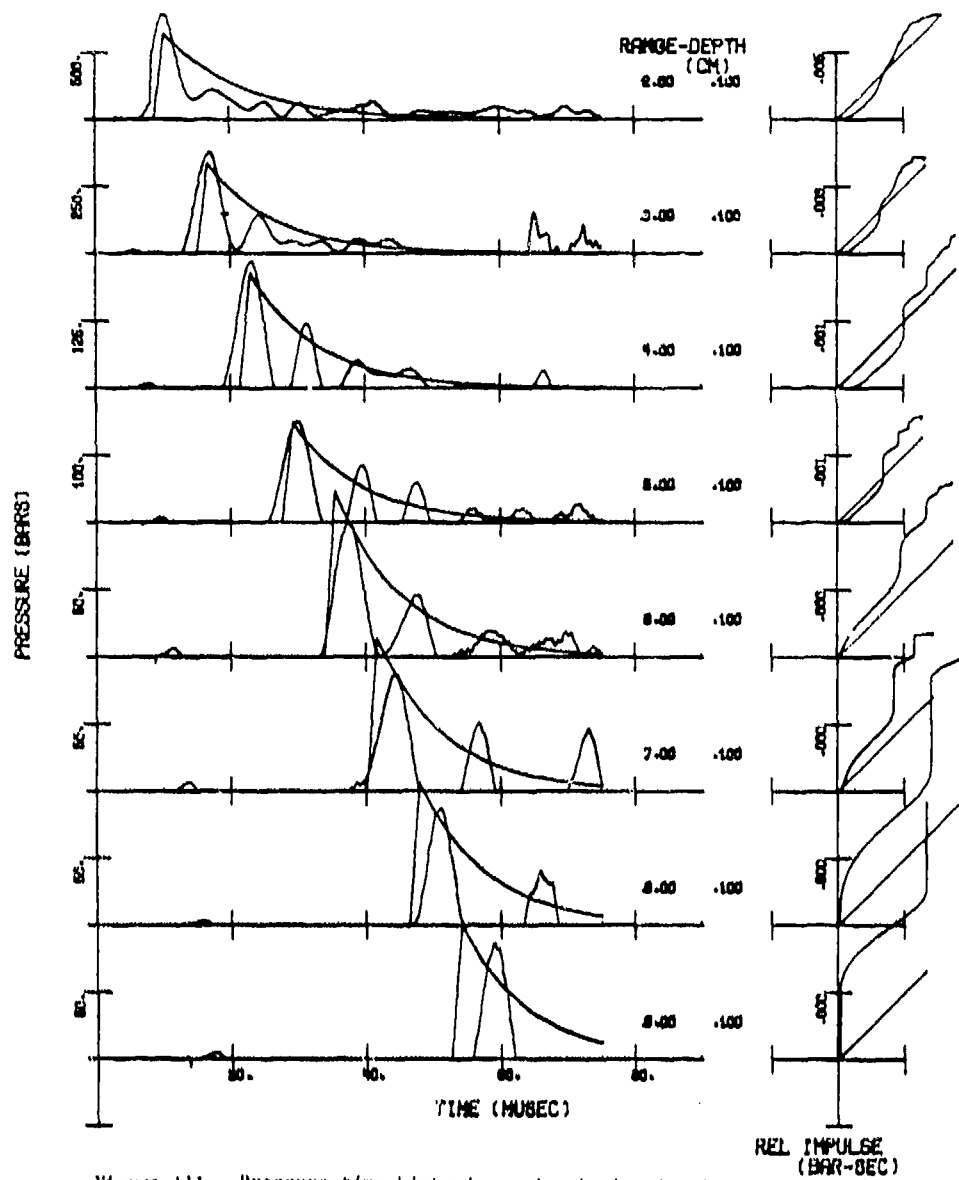
73

Figure A5. Pressure time histories and relative impulses for points 2 to 9 cm from the impact, .1 cm behind the front panel from $7X1.6J$ ($R_0 = .875$, $\omega = .635$ $V = 1.64$).

Figure A6. Pressure time histories and relative impulses for points 5 to 10 cm from the impact, .1 and .6 cm behind the front panel from 7X1.63 (R_p = .875, ω = .635, V = 1.63).

75

Figure A7. Pressure time histories and relative impulses for points 2 to 9 cm from the impact, .1 cm behind the front panel from 7L1.63, (R_0 = .7, ω = .158, V = 1.63).
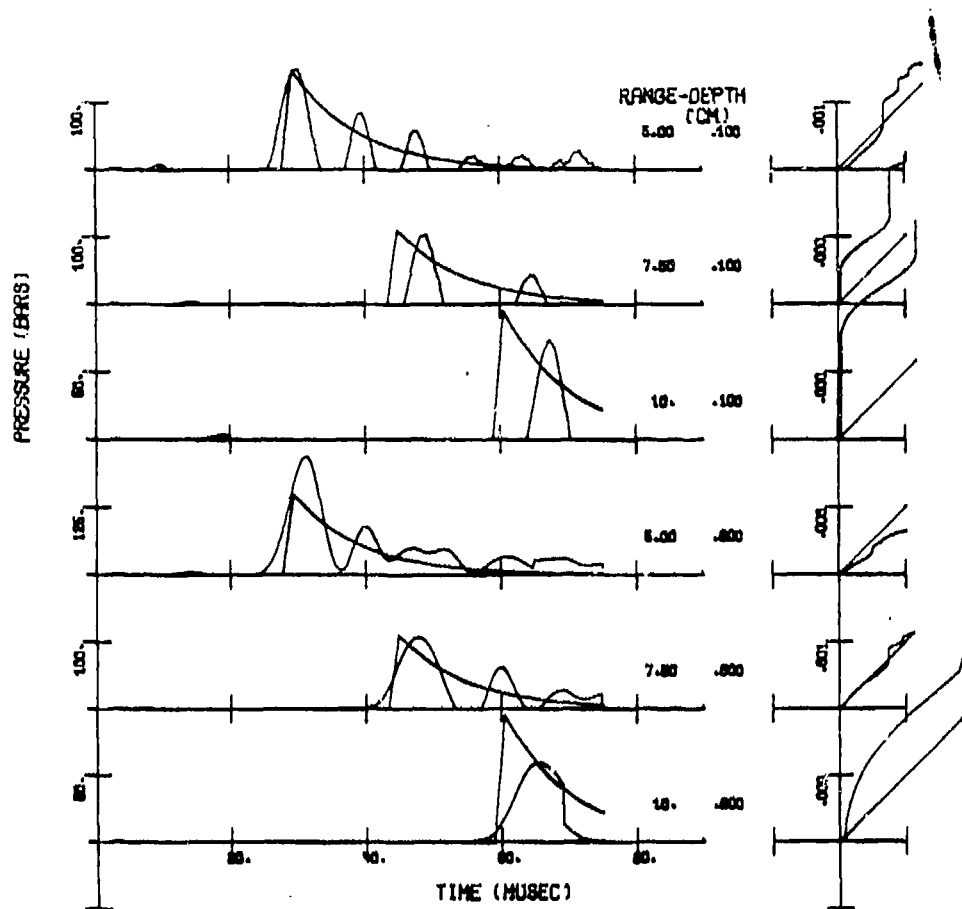
Figure 48. Pressure time histories and relative impulses for points 5 to 10 cm from the impact, .1 and .6 cm behind the front panel from 741.63, (R_p = .7, ω = .158, V = 1.63)
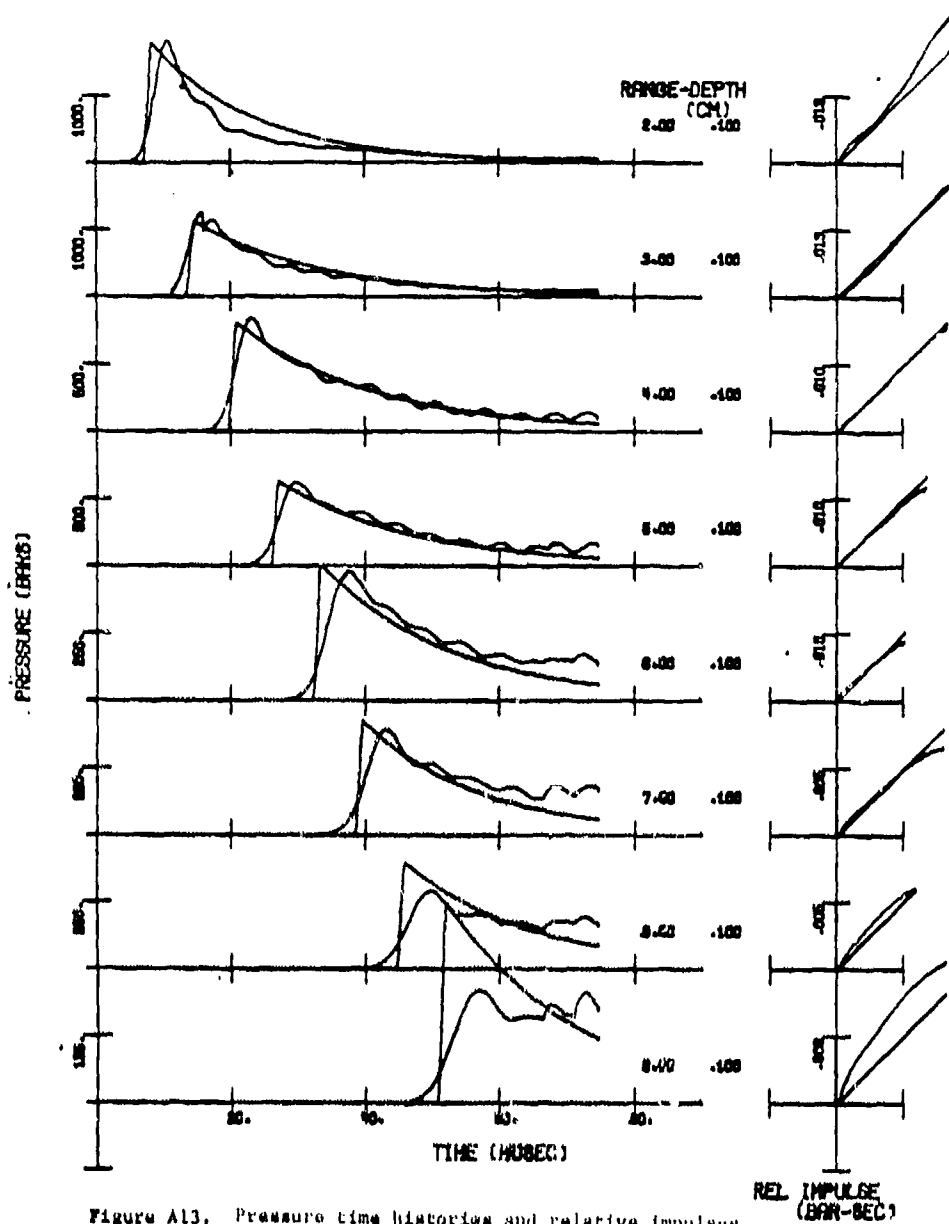
Figure A9. Pressure time histories and relative impulses for points 2 to 9 cm from the impact, .3 cm behind the front panel from 281.35 (R_p = .99, ω = .635, V = 1.35).

Figure A10. Pressure time histories and relative impulses for points 5 to 10 cm from the impact, .1 and .6 cm behind the front panel from Z81.35 (W_p = .55, ω = .635, V = 1.35).
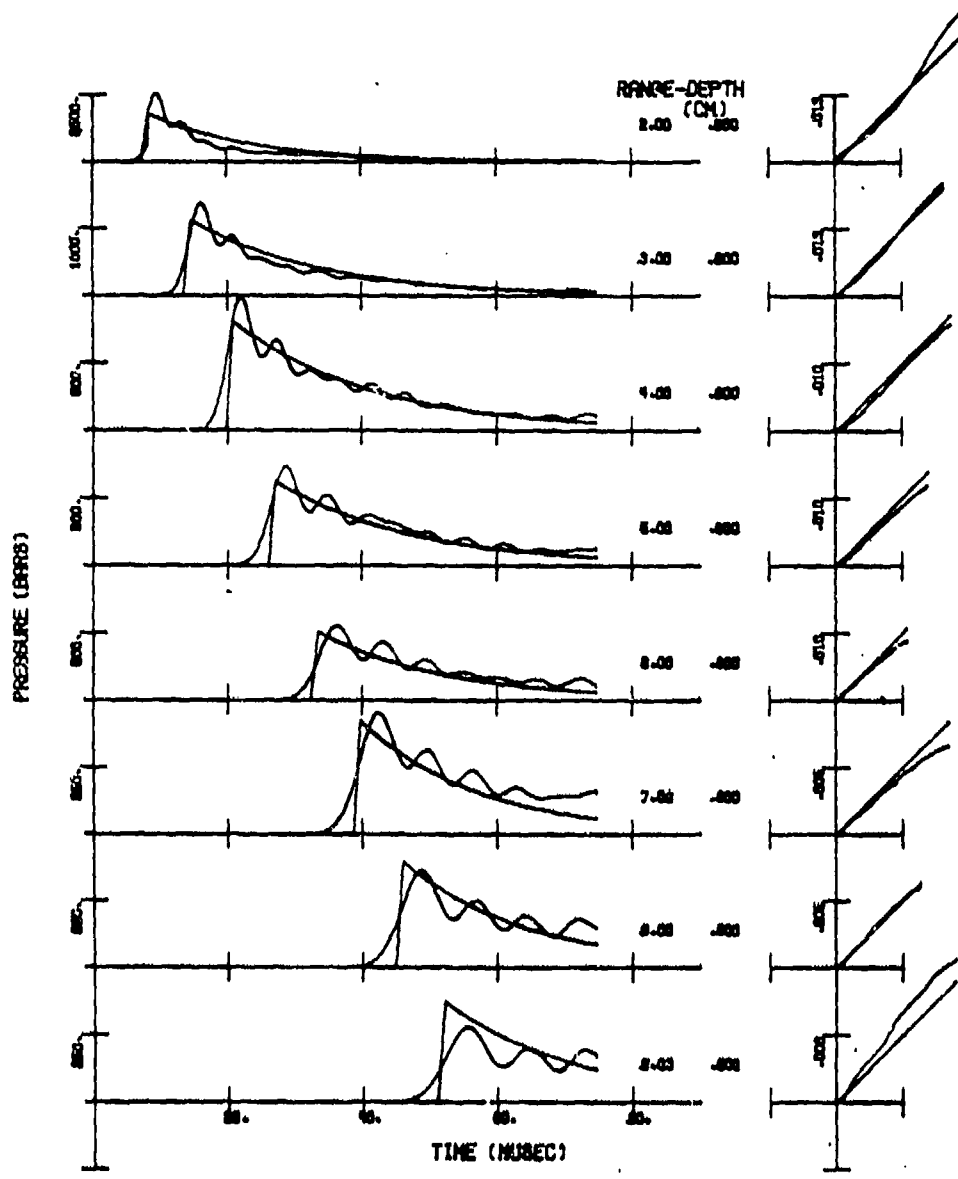
79

Figure A11. Pressure time histories and relative impulses for points 2 to 9 cm from the impact, .1 cm behind the front panel from 7S1.35 (R_p = .55, ω = .158, V = 1.35).

Figure A12. Pressure time histories and relative impulses for points 5 to 10 cm from the impact, .1 and .6 cm behind the front panel from 7S1.35, (R_p = .55, ω = .158, V = 1.35).

Figure A13. Pressure time histories and relative impulses for points 2 to 9 cm from the impact, .1 cm behind a rigid front surface, RL1.63 (R_p = .7, ω = ∞, V = 1.73).

Figure A14. Pressure time histories and relative impulses for points 2 to 9 cm from the impact, .5 cm behind a rigid front surface, RL1.63 ($R_p = .7$, $\omega = \infty$, $V = 1.63$).

APPENDIX B

PEAK HOOP STRESS VS RANGE FOR 7075-T6 Al FRONT PANELS
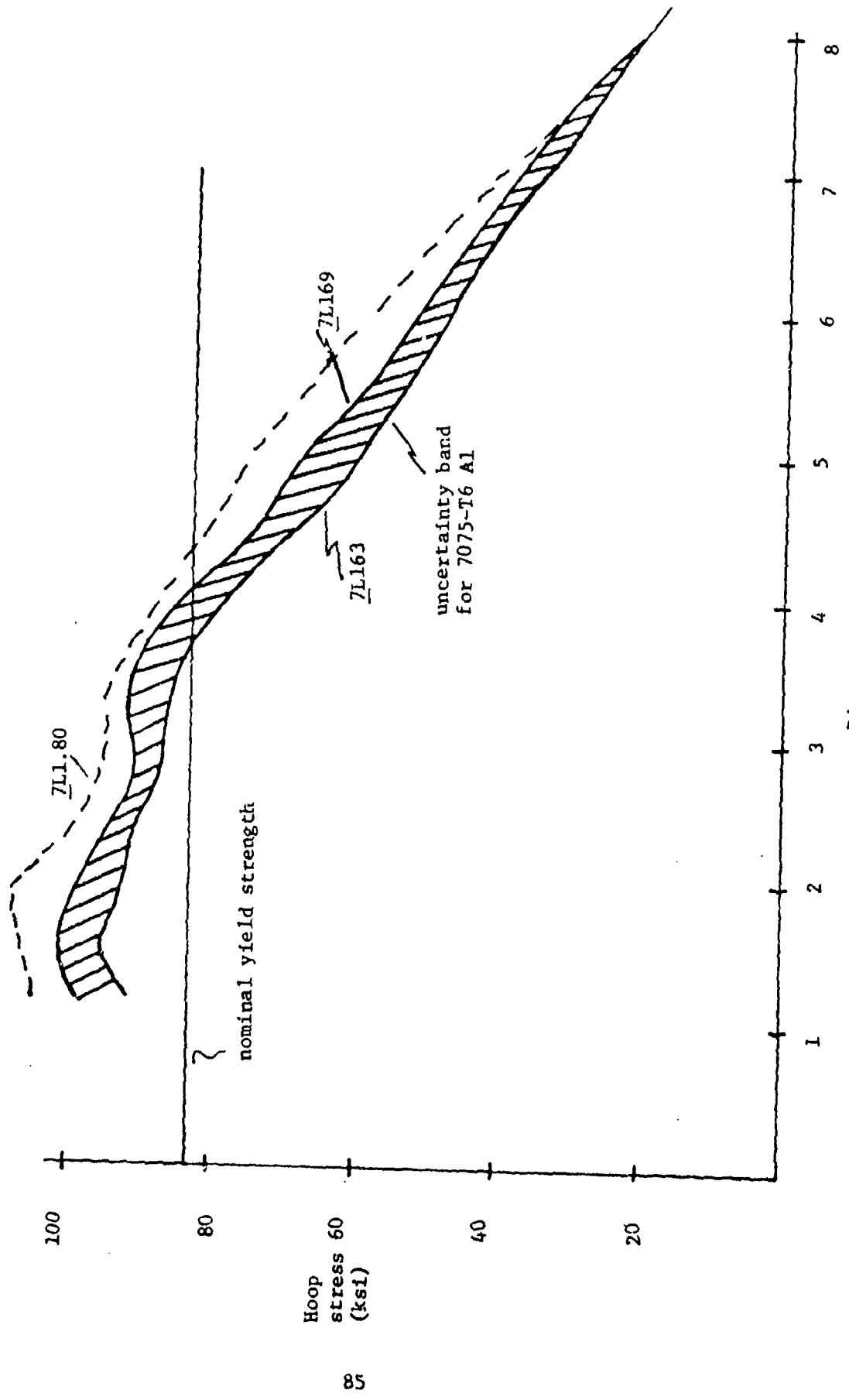
Figure B1.   Peak tensile Hoop Stress for calculations of 11.66 gm steel spheres impacting ¼-in 7075-T6 Al front panel.
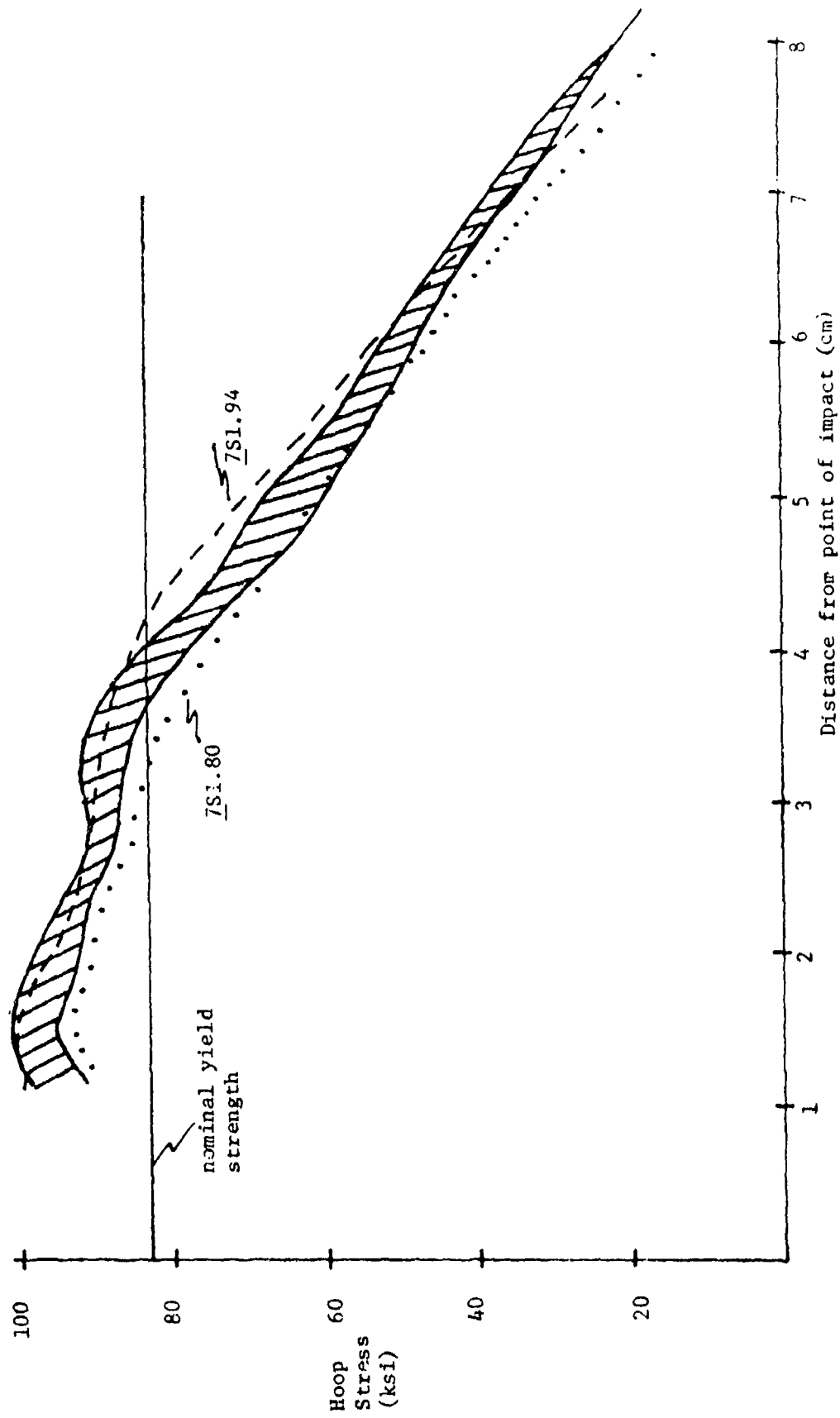
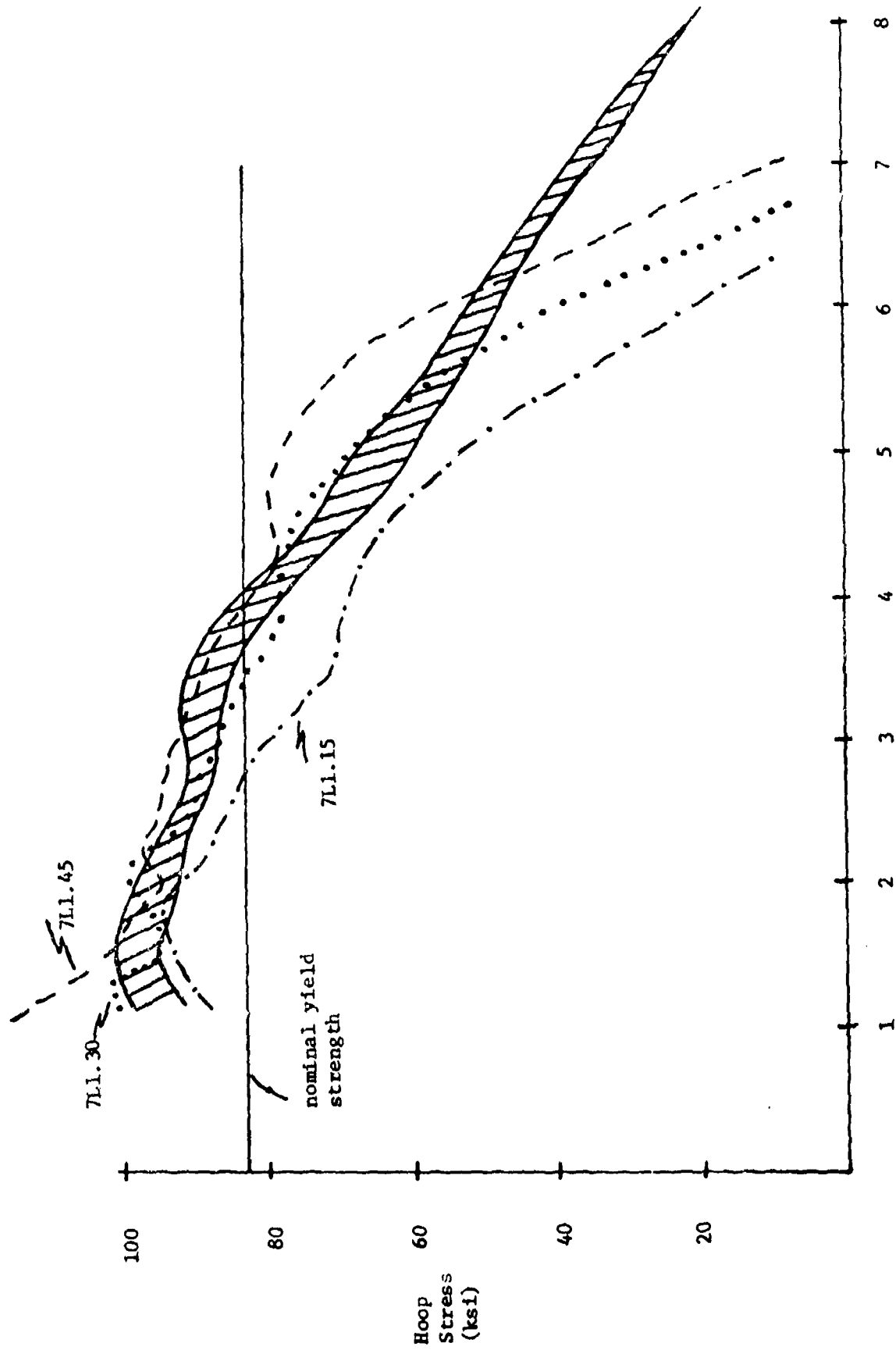Figure B2   Peak tensile Hoop Stress for calculations of 5.83gm steel spheres impacting ¼-in 7075-T6 Al front panel.

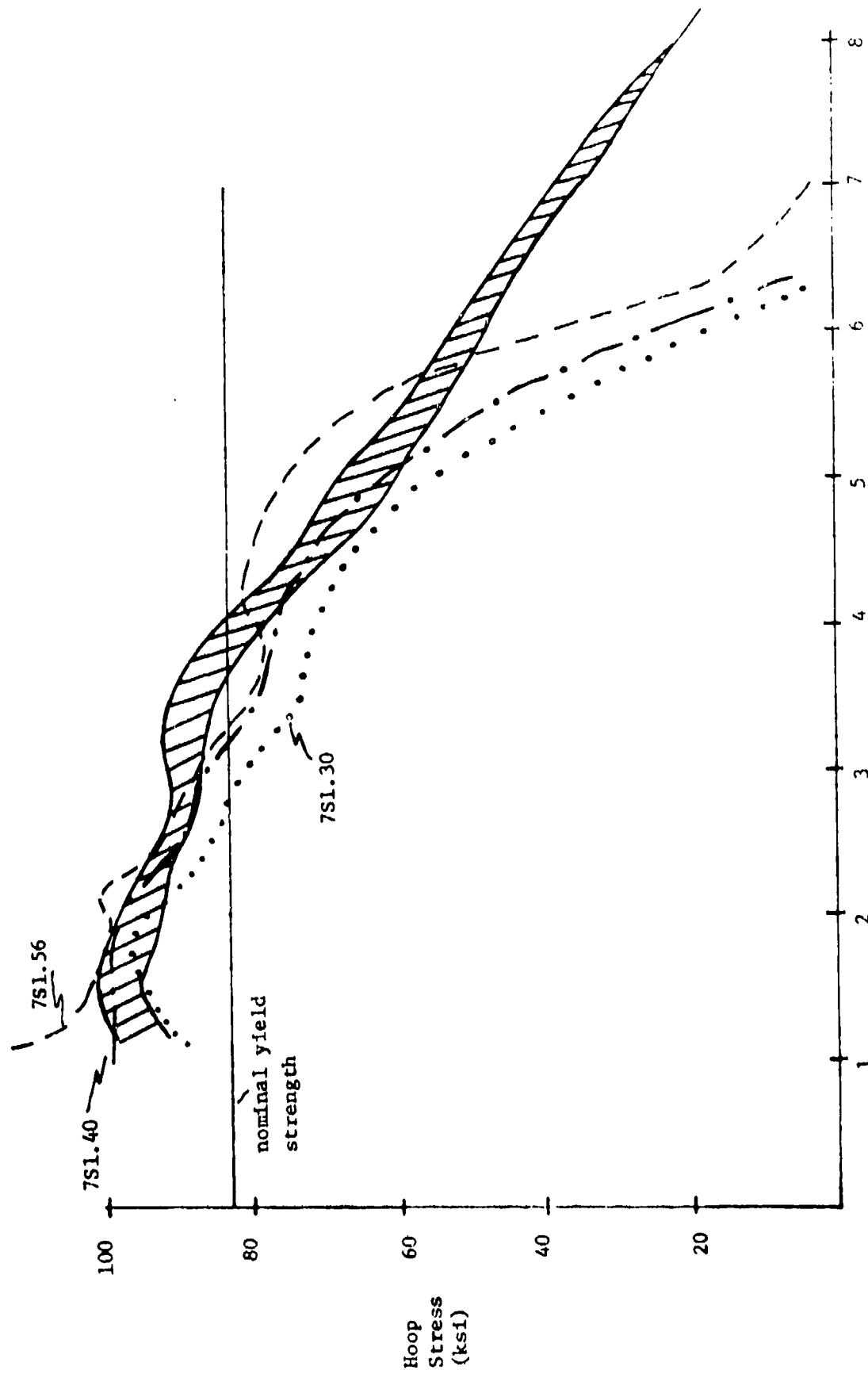Figure B3. Peak tensile Hoop Stress for calculations 11.66gm steel spheres impacting 1/16-in 7075-T6 Al front panel.

Figure B4. Peak tensile Hoop Stress for calculations 5.8 gm steel sphere impacting 1/16-in 7075-T6 Al front panel.

APPENDIX C

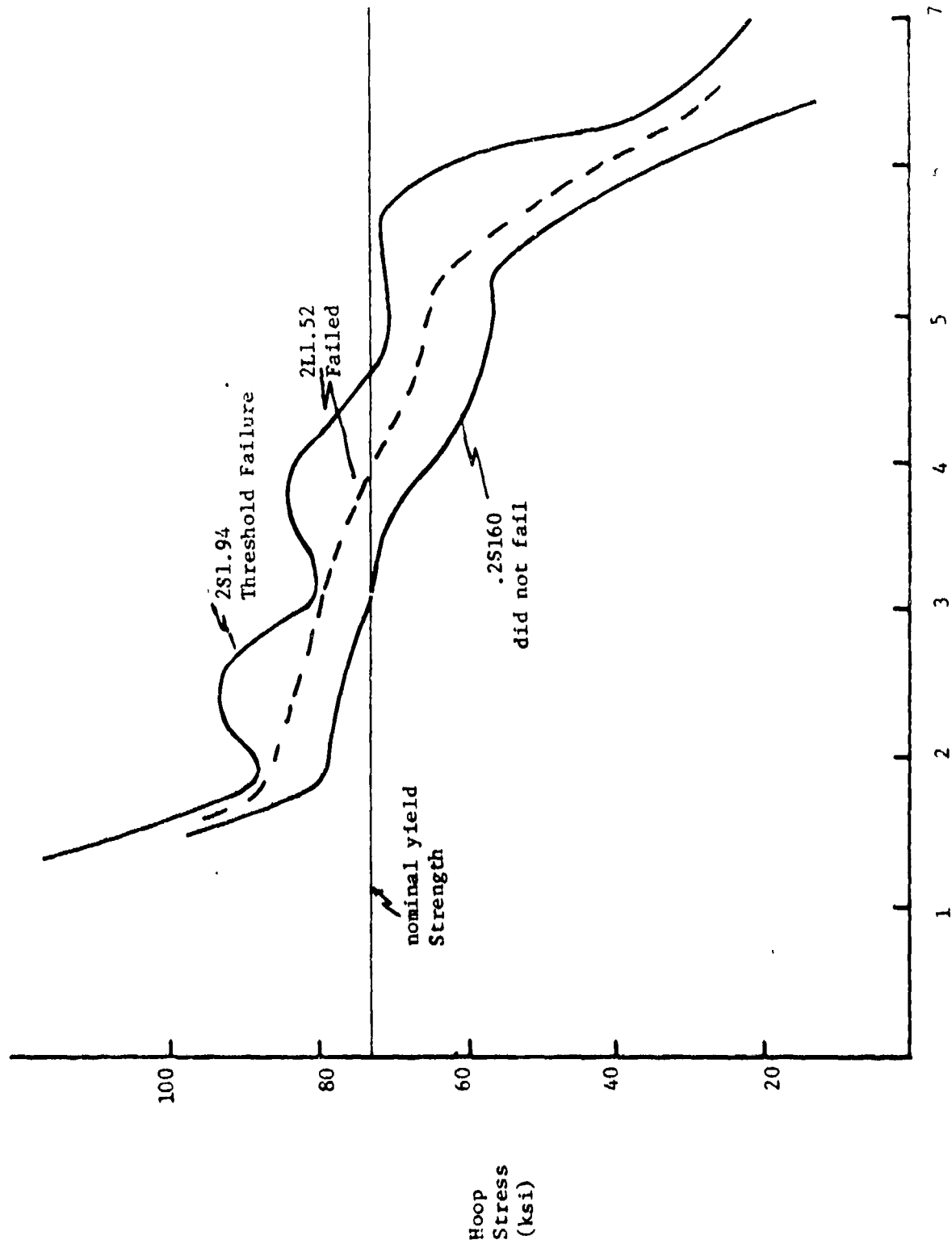PEAK HOOP STRESS VS RANGE FOR 2024-T3 A1 FRONT PANELS

Figure C1. Peak tensile Hoop Stress for calculations of 5.83-in steel sphere impacting 1/16-in 2024-T3 Al front panel
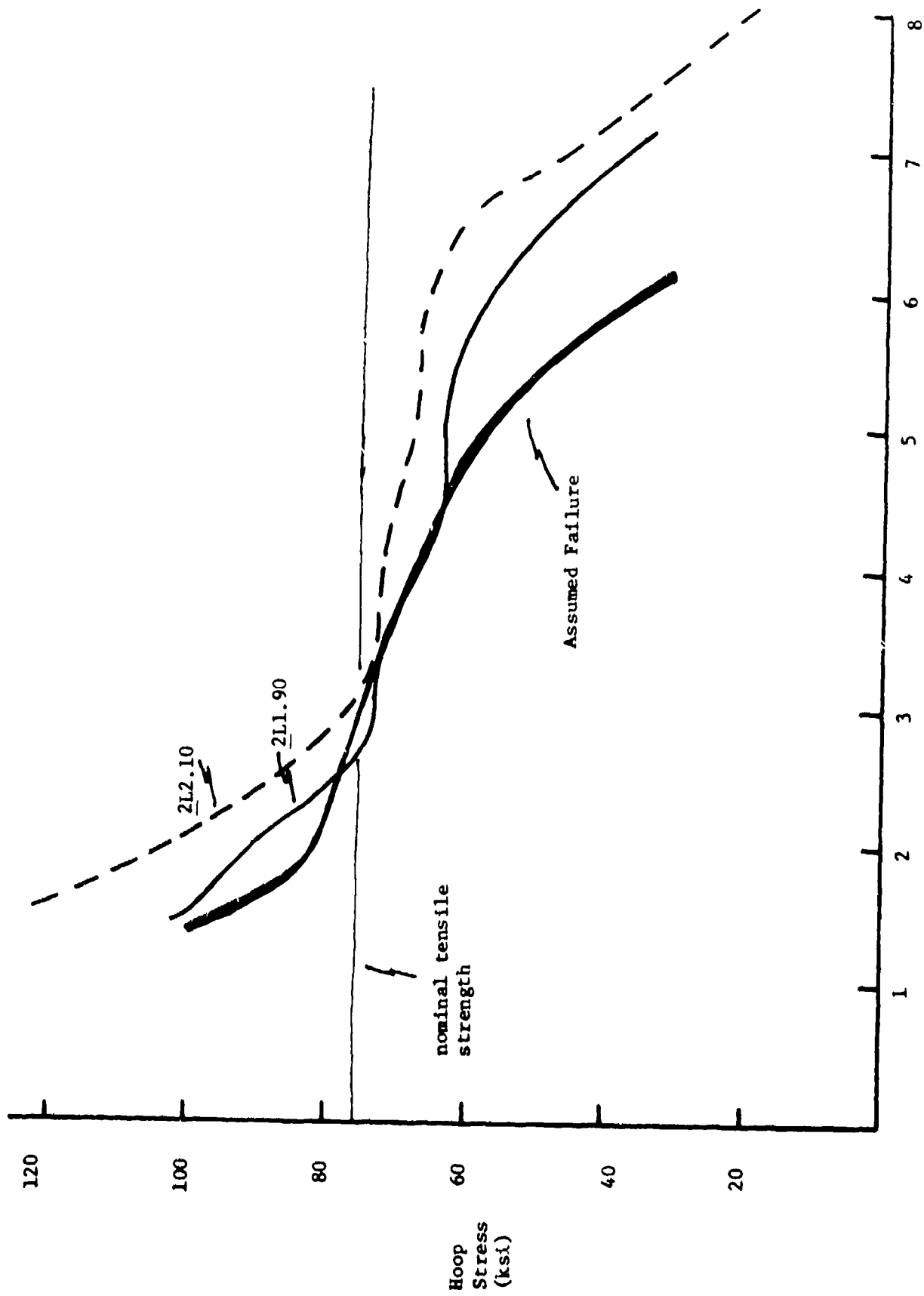
Figure C2. Peak tensile Hoop Stress for calculations of 11.66gm steel sphere impacting 1/4- in 2024-T3 Al front panel
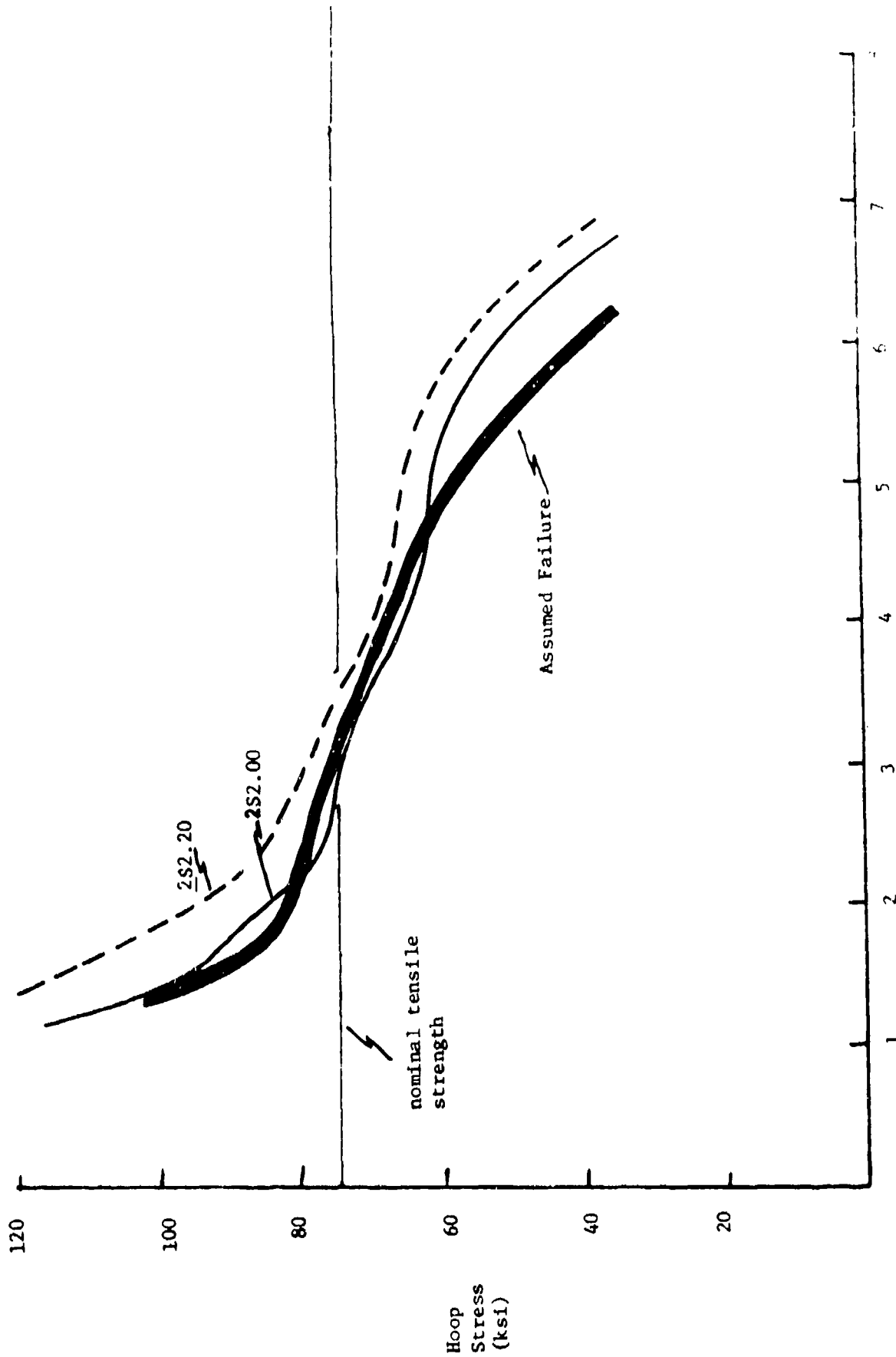
Figure C3. Peak tensile Hoop Stress for calculations of 5.8 in s... impacting 1/4-in 2024-T3 Al front panel.